Master's thesis

NTNU
Norwegian University of Science and Technology
Faculty of Information Technology and Electrical Engineering
Department of Electronic Systems

Vegard Leer Leksås

Optical Sensor System for Deflection and Vibration Detection in Internal Turning Tools

Master's thesis in Electronic Systems Design
Supervisor: Dag Roar Hjelme
June 2021

NTNU
Norwegian University of
Science and Technology

Vegard Leer Leksås

Optical Sensor System for Deflection and Vibration Detection in Internal Turning Tools

Master's thesis in Electronic Systems Design
Supervisor: Dag Roar Hjelme
June 2021

Norwegian University of Science and Technology
Faculty of Information Technology and Electrical Engineering
Department of Electronic Systems

NTNU
Norwegian University of
Science and Technology

Abstract

Reducing vibrations and tool deflection in internal turning is an important factor for improving the machining result. An optical sensor system for measuring these parameters is developed in this project. The sensor system utilises a collimated laser diode in combination with a Position Sensitive Device (PSD) to measure the tool deflection and vibrations. The PSD S5991-01 is identified to be a good choice for the sensor system with its high linearity and wide measurement area. A mechanical test setup has been developed to test the performance of the sensor system. At a cutting tool length of 500 mm the deflection measurement range is found to be 1084.7 µm in every direction.

To meet the specified deflection resolution requirement of less than 1 µm, a new sensor interface was developed. With an improved reference voltage generation and a differential ADC configuration, the noise amount on the measurement signals is reduced about 9 times. This has resulted in an improved deflection resolution of 0.7 µm, which is within the specified requirement. Vibration measurements revealed that the sensor system perfectly detected the applied vibration frequencies, in the range from 0 to 500 Hz. It was observed that the measured vibration amplitude varied with the applied vibration frequency, even though the applied vibration amplitude was constant. The main cause of this problem is identified to be mechanical resonance in the test setup. The mechanical setup must therefore be further investigated, and possibly changed in order for the sensor system to measure correct vibration amplitudes.

Sammendrag

Ved innvendig dreiing er det viktig å redusere vibrasjoner og verktøyutbøying for å forbedre resultatet av maskineringen. I dette prosjektet har det blitt utviklet et optisk sensorsystem for å måle disse parameterne. Sensorsystemet bruker en kollimert laser diode sammen med en posisjonssensor for å oppnå dette. Den optiske posisjonssensoren S5991-01 har vist seg å være et godt valg for bruksområdet, grunnet sensorens høye linearitet og store måleområde. Et mekanisk testoppsett har blitt utviklet for å teste sensorsystemets ytelse. For et dreieverktøy med lengde 500 mm, kan sensorsystemet måle utbøyinger av verktøyet i en radius av 1084.7 µm.

Sensorelektronikken ble forbedret for å oppnå det angitte kravet om en utbøyingsoppløsning mindre enn 1 µm. Ved å benytte en forbedret spenningsreferanse og bruke en differensiell ADC konfigurasjon, ble støynivået på målesignalene redusert ca. 9 ganger. Dette førte til en forbedret utbøyingsoppløsning på 0.7 µm, som er innenfor det satte kravet. Vibrasjonsmålinger viste at sensorsystemet målte påførte vibrasjonsfrekvenser perfekt i frekvensområdet 0 til 500 Hz. Den målte vibrasjonamplituden varierte med endringer i vibrasjonfrekvensen, selv om den påførte vibrasjonamplituden var konstant. Hovedgrunnen til dette problemet var mekanisk resonans i testoppsettet. For å fikse dette problemet, burde det mekaniske oppsettet undersøkes ytterligere og eventuelt endres.

Acknowledgements

I would like to thank my supervisor Dag Roar Hjelme for his technical input and guidance throughout this project. I would also like to thank Sandvik Coromant Trondheim for allowing me to work on this exciting project for the last four semesters. This especially includes my co-supervisors Dan Østling and Audun Lønmo Knudsrød for their assistance and guidance throughout this project, as well as mechanical engineers Ole Henrik Johansen and Magnus Olsen for developing the required mechanical components. Lastly, I would like to thank Lloyd Clark at Microchip for our discussions around different electrical aspects of the system, and for lending me useful development equipment.

Vegard L. Leksås
Trondheim, June 14^{th} 2021

Contents

Figures

Acronyms

ADC Analogue-to-Digital Converter. i, 25, 43, 51, 52, 57–60, 64, 66, 68–70, 73, 97

DAQ Data Acquisition. 25, 30, 39, 47, 51, 52, 57, 61

DC Direct Current. 39, 40, 48, 57, 70

FFT Fast Fourier Transform. 48–50, 97

IC Integrated Circuit. 25, 59, 65

ICE In-Circuit Emulation. 60

IDE Integrated Development Environment. 62

kbps kilobits per second. 66

MCU Microcontroller Unit. 52, 66

PCB Printed Circuit Board. vii, viii, 22, 24–27, 29–31, 43, 51, 52, 59, 60, 62–65, 73, 80, 82, 84

PGA Programmable Gain Amplifier. 58

PSD Position Sensitive Device. i, vii, 5–7, 9–11, 15, 16, 22, 23, 25, 26, 52, 54, 63

PSU Power Supply Unit. 45, 71

PTP Peak-To-Peak. 40, 43, 45–47, 55, 59, 71–73, 97

SD Standard Deviation. 39, 40

SMD Surface Mount Device. 22, 25, 62

SNR Signal-to-Noise Ratio. 54, 73

SPI Serial Peripheral Interface. 59, 60

TIA Transimpedance Amplifier. 6, 7, 11, 23–27, 30, 54, 55, 57, 58, 67, 73

UART Universal Asynchronous Receiver-Transmitter. 59–63, 66

UPDI Unified Program and Debug Interface. 60

USB Universal Serial Bus. 55, 59–63

Chapter 1

Introduction

1.1 Background

Turning is a machining process in which a single point cutting tool moves parallel to the axis of rotation of a rotating workpiece [1]. This process can be used to remove material of a workpiece in order to create cylindrical and rounded forms. Turning is the most common process for metal cutting.

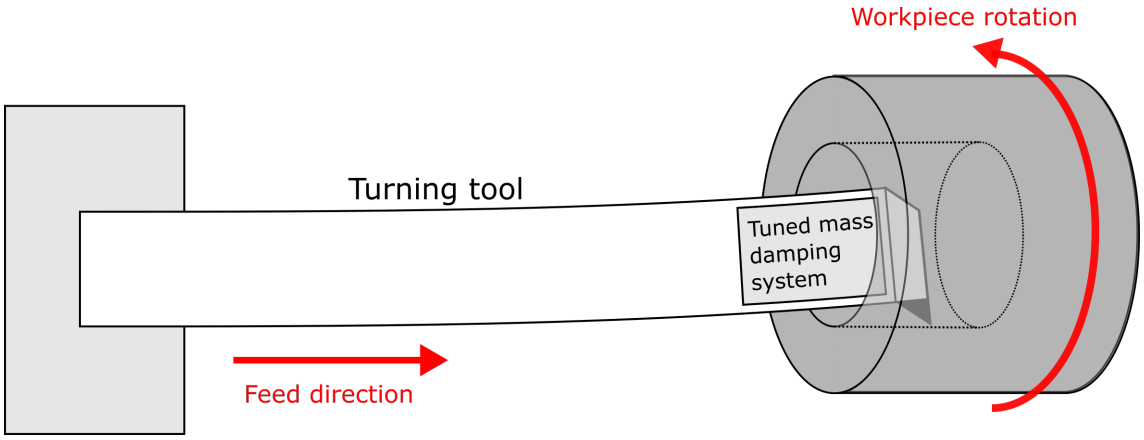

Figure 1.1: The general concept of internal turning. A single point cutting tool is used to create cylindrical holes in the rotating workpiece.

In order to create cylindrical holes in a workpiece, a machining process called internal turning is often used. Cutting tools used for internal turning requires long overhangs in order to make deep holes in a workpiece. Long overhangs can aggravate problems with both tool deflection and vibrations caused by the applied cutting forces. Both vibrations and tool deflection will have a negative impact on the cutting result and are therefore important to measure, and if possible, correct during a machining process.

Sandvik Coromant Trondheim have implemented a sensor system for measuring both the tool deflection and vibrations in their internal turning tools. An accelerometer is mounted inside the tool, close to the cutting tip in order to measure the vibrations at the cutting tip. In addition,

four strain gauges is mounted inside the cylindrical overhang of the cutting tool. By measuring the strain applied to the cutting tool caused by the cutting forces, it is possible to calculate the tool deflection. A certain positioning and configuration of the strain gauges allows the system to measure the tool deflection in two axes.

However, there are a few challenges related to the existing sensor system. These are mainly related to the assembly process and the available space inside the cutting tool. Sandvik Coromant develops cutting tools in many different sizes, depending on the application. The current sensor system requires that there is sufficient space in the front of the cutting tool to mount the breakout board for the accelerometer. There must also be space to mount the strain gauges on the inside of the tool cylinder. In addition, it is necessary for the sensor wires to be routed to the back end of the tool. This will also require additional space inside the cutting tool. These requirements can be problematic in smaller cutting tools, where the available space inside the tool is limited. The same applies for the mounting process, as it is usually much harder to insert these sensors into smaller tools.

Therefore, Sandvik Coromant Trondheim is interested in finding an alternative solution to their sensor system. A possible solution to the existing challenges is to use an optical sensor system. The main advantage of an optical system, if developed correctly, is that it can eliminate the need for any electronics and wires in the front of the tool. This reduces the required space inside the cutting tool, while also allowing for an easier assembly process.

1.2 Optical Sensor System

The basic concept of an optical sensor system for this application is depicted in Figure 1.2. A laser diode is placed in the back of the cutting tool. The collimated laser beam will travel through the cylindrical tool and hit a mirror in the opposite end. The mirror will then reflect the laser back. An optical position sensor will be used to detect the position of the laser spot within the sensor's measurement surface. In addition, a beam splitter is placed in the laser path in order to redirect the reflected laser beam in the direction of the sensor.

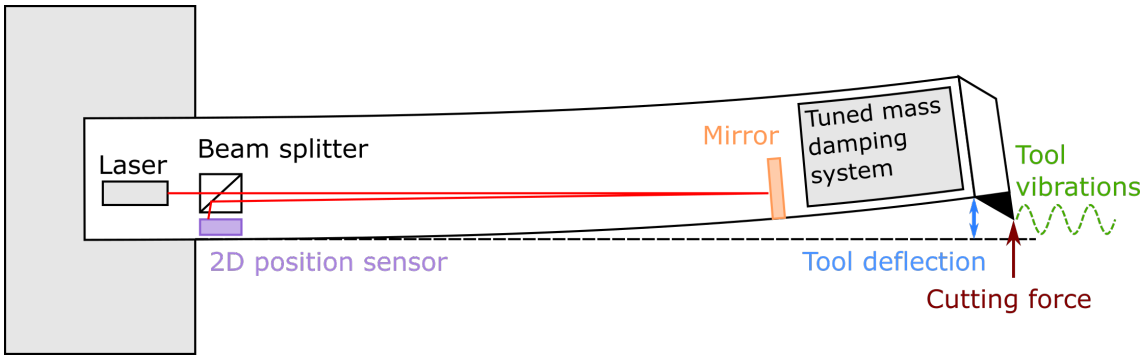

Figure 1.2: Basic concept of the optical sensor system. The system utilises a laser diode and an optical position sensor to measure the deflection and vibrations of the cutting tool. With the use of a mirror and a beam splitter, all the electrical components can be kept in the back end of the cutting tool.

The cutting tool is fixed in one end, such that the cutting force induces a curvature. The curvature will result in a change of the mirror angle and therefore a change in the angle of reflection. This will result in a change of the laser spot position. Thus, the measured laser spot position can be used to calculate the tool deflection. Similarly, the vibrations at the cutting tip can be measured, as these are rapid changing deflections.

The idea of using such an optical sensor system was first proposed many years ago by Dan Østling at Sandvik Coromant Trondheim. A project at that time was therefore started to research if such a sensor system could work. However, due to priority reasons, it was never finished. The current project to look further into this topic was therefore started in collaboration with Sandvik Coromant Trondheim, August 2019.

1.3 Problem Description

The goal of the overall project was to develop and test an implementation of the optical sensor system presented in Section 1.2. A variety of tests should be performed to test the functionality and state the performance of the developed sensor system. These results should be further discussed in order to conclude if such an optical sensor system is a viable option for the defined application.

1.3.1 System Requirements

As different sized cutting tools have different amounts of deflection, it is challenging to develop a sensor system suitable for all tool sizes. The sensor system was therefore set to be developed for cutting tools with a length of about 500 mm. The overall size of the sensor system is an important aspect. However, a size requirement was not set for this development as the main goal was to test the concept. The system should be designed so it can measure deflections of the cutting tool in a square of 2 mm × 2 mm. This means that the system should be able to measure the deflection of the tool as long as it is deflected within an area of 2 mm × 2 mm. Within the measurement range the system should be able to detect variations of the tool deflection down to 1 µm. This is defined as the deflection resolution. In addition, the system should be able to measure vibrations of frequencies between 0 and 500 Hz occurring at the cutting tip. These system requirements are summarised in Table 1.1.

Sensor System Aspect	Requirements
Cutting tool length	500 mm
Deflection resolution	1 µm
Deflection measurements range	2 mm × 2 mm
Vibration frequency detection range	0 to 500 Hz

Table 1.1: Requirements set for the optical sensor system.

1.3.2 Development Areas

The development of a sensor system like this requires the implementation of several different subtasks and raises both electrical, optical and mechanical challenges. The main tasks that need to be solved are listed below.

Calculation of tool deflection: The system requires a function for calculating the tool deflection based on the measured position of the laser spot. This is heavily dependent on the dimensions of the system and the positions of the optical components.

Test setup: Build a setup for testing and developing the sensor system. This will be essential for testing the functionality of the system and for comparing different solutions.

Optical components: Select components like the laser diode, sensor, beam splitter and mirror. Compatibility is crucial as the laser diode and the sensor needs to be compatible with each other. The mirror and beam splitter should be selected according to the laser diode and the sensor, but also based on the system dimensions.

Mechanical components: Plan and develop required mechanical components in cooperation with Sandvik Coromant Trondheim. The company has the ability to manufacture the required mechanical components. The test setup will require several different components, including adjustment components in order to align the laser beam correctly.

Sensor interface: The sensor will require additional electronics for the measurement data to be handled by a computer. If a standalone sensor is chosen, it will require an amplification circuit, sampling circuit and possibly a circuit to process and send the data to a computer.

Data processing and presentation: The measurement data from the sensor can be processed either by hardware, software, or a combination of both. The system also requires a graphical interface to present the measurement data.

1.4 Previous Work and Inspiration

The combination of using a laser diode and an optical position sensor to measure both vibrations and displacements of objects is a well-known concept. A. Saha et al. [2] used a Position Sensitive Device (PSD) in combination with a collimated laser diode and a mirror to measure the vibration applied by a speaker, in the range from 20 Hz to 800 Hz, with a displacement resolution of 7 µm. D. Shetty et al. [3] presented an optical sensor system for measuring vibrations of workpieces during machining processes. The idea of the sensor system is close to what was proposed by Sandvik Coromant Trondheim, where the vibrations of an object with a mirror attached can be detected by the use of an optical position sensor and a laser diode. However, the experimental system is designed to be an external and portable setup which can be used for multiple applications.

A fairly practical approach has been used to develop the sensor system. This means that decisions made during the development process are mainly based on test results of the system, and challenges that got apparent during the development process. The project started the autumn of 2019, by looking closer into a laser diode and a position sensor which had previously been tested by Sandvik Coromant Trondheim. No details about the previous project was provided, as they wanted the student to start with a fresh perspective on the project. The project has been worked on for three different courses and resulted in three reports before starting this master's project. An outcome of the three sub-projects was a developed test setup of the optical sensor system. Due to this being a very important aspect of the overall project, the most crucial parts of the development process is included in Chapter 3. Thus the work presented in Chapter 3 is the result of the pre-project conducted by the student before starting the master's project.

1.5 Scope

As the master's project started with having a developed test setup, the first step was to test the system. From initial tests it was known that the noise levels of the test setup would not be low enough to match the system requirements. The goal of the master's project was therefore set to test and analyse the performance of the test setup. Focusing on the measurement range, deflection resolution, and the system's ability to detect vibrations. Furthermore, the sensor interface would be improved to try to reduce the noise of the system and therefore increase the deflection resolution. Lastly, the same measurements would be performed using the improved sensor interface to verify the performance improvements.

This thesis will present and discuss the development of the initial system and its performance. This will be the foundation for the development and testing of the improved sensor interface. Lastly, the overall functionality and usability of the sensor system will be discussed to conclude if the sensor system is a viable option for the application.

1.6 Thesis Structure

The thesis is structured as following:

1. Introduction introduces the background for the project and defines a problem. The previous work of the project is presented and the scope of the thesis is explained.

2. Theory presents theory for understanding how a Position Sensitive Device works. In addition, theory about Transimpedance Amplifiers is presented.

3. Test Setup Development presents the idea, challenges and development of the test setup for the optical sensor system. This chapter presents the work conducted by the student prior to the master's project.

4. Initial Test Setup Performance presents measurements performed on the initial test setup and discusses the test results. This includes finding the system sensitivity and measurement range of the test setup. Finding the deflection resolution by defining the amount of electrical noise on the measurement signals. Lastly, the system's ability to measure vibrations is also tested.

5. Sensor Interface Improvements present the development of an improved sensor interface for reducing the noise on the measurements signals, and making the test setup into a complete system, instead of an experimental test setup.

6. Test Setup Performance with Improved Sensor Interface presents the performance of the test setup with the improved sensor interface, focusing on the same measurement that was performed on the initial setup.

7. Discussion discusses the results of an improved sensor interface and the sensor system's performance. Furthermore, the test methods used are evaluated and the sensor system's ability to be implemented in a cutting tool is discussed.

8. Conclusion summarises the achievements of the project and presents further work.

Chapter 2

Theory

This chapter will present theory for understanding how a Position Sensitive Device work. In addition, theory about Transimpedance Amplifiers will be presented.

2.1 Photodiode

A photodiode is a semiconductor device with a P-N junction that converts photons (or light) into electrical current [4]. A cross-section of a typical P-N photodiode is depicted in Figure 2.1. The diffusion of electrons from the N layer to the P layer and holes for the P layer to the N layer, creates a depletion region where no free carriers exist. This creates an electric field over the depletion region.

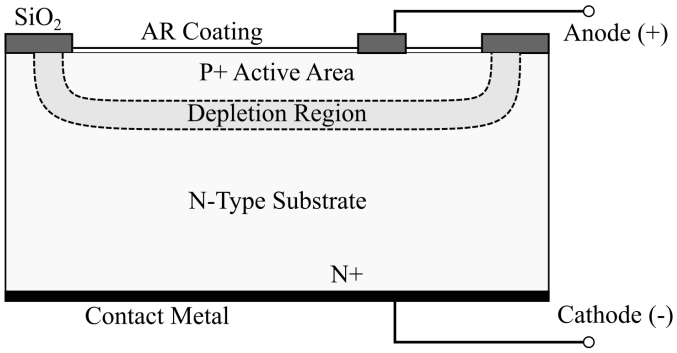

Figure 2.1: Cross-section of a typical P-N photodiode. A P-N photodiode is a semiconductor device that converts photons (or light) into electrical current.

When photons with sufficient energy strike atoms within the device, electrons are released. This creates so-called electron–hole pairs. Due to the electrical field over the depletion region, electrons will move towards the cathode and holes move towards the anode. This will result in a photocurrent in the diode. The photocurrent will be dependent on the amount of photons hitting the depletion region.

There are a few key parameters which describes the performance of a given photodiode. Some of them are response time, spectral responsivity, and dark current:

Response Time: The time required for charge carriers to cross the P-N junction. The response time is dependent on the capacitance of the P-N junction. The capacitance over the P-N junction is heavily dependent on the width of the depletion region.

Spectral Responsivity: The ratio between the generated photocurrent and the power of the incident light. Expressed as ampere per watt $[A/W]$. This ratio will change depending on the wavelength of the incident light.

Dark Current: The current travelling through the photodiode when there is no incident light. The dark current includes the photocurrent generated by background radiation and the saturation current of the semiconductor junction. This makes the dark current a huge noise source of photodiodes.

2.1.1 PIN Photodiode

A PIN photodiode is similar to the basic P-N photodiode. However, in a PIN photodiode the P and N-layer is separated by an intrinsic layer. A cross-section of a PIN photodiode is depicted in Figure 2.2. The highly resistive intrinsic layer results in a stronger electric field compared to a P-N photodiode. The higher electrical field result in a lower capacitance over the junction, which result in a lower response time of the photodiode. The wider depletion region will also allow for more electron-hole pairs to be created and will result in a higher photocurrent. Therefore, a PIN photodiode usually have a higher spectral responsivity compared to the P-N photodiode.

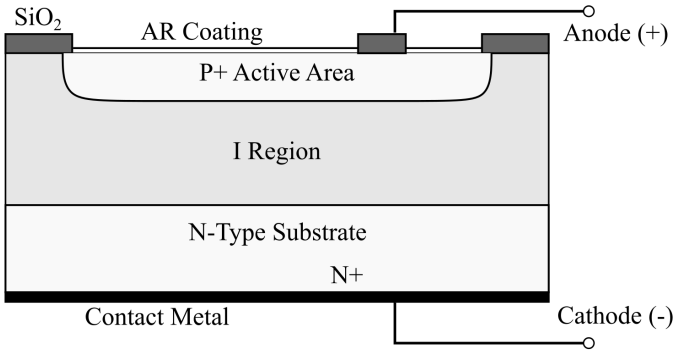

Figure 2.2: Cross-section of a typical PIN photodiode. The structure of the PIN photodiode allows for lower response time and higher spectral responsivity compared to the P-N photodiode.

2.1.2 Modes of Operations

A PIN photodiode can be configured to two different modes, depending on the voltage applied over the diode. The two different modes are called photovoltaic mode and photoconductive mode, which is illustrated in Figure 2.3. In photovoltaic mode, the anode and cathode of the photodiode is open-circuited. This means that the voltage over the photodiode is zero. With no external voltage applied over the junction, the dark current will be close to zero, which will reduce the noise of the photodiode.

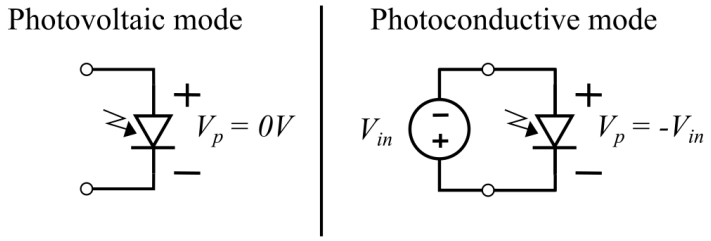

Figure 2.3: Modes of operation for a photodiode. Photovoltaic mode is used when low noise is preferred, while photoconductive mode is used when low response time is preferred.

In photoconductive mode the photodiode is reverse biased. This means that the voltage potential is higher at the cathode compared to the anode. The reverse bias causes the potential over the depletion region to increase and therefore the depletion region width to increase. As mentioned in the comparison between a PIN and P-N photodiode, a larger depletion region will result in a lower response time. A big disadvantage with the photoconductive mode, is the increase in dark current due to a larger depletion region.

The photoconductive mode is often used in high-speed applications due to the lower response time. However, in precision applications where low noise is an important aspect, the photovoltaic mode is a better solution. Photovoltaic mode works well for low frequency applications under 350 kHz [4].

2.2 Position Sensitive Device

A Position Sensitive Device (PSD) is a device that can be used to measure the position of a light spot. Most position sensitive devices use the same structure as a PIN photodiode. However, PSDs have two or four electrodes placed on the P-layer versus the one of a regular PIN photodiode. Figure 2.4 displays the cross-section of a typical one-dimensional PIN PSD. When a light spot strikes the PSD, photocurrents are generated, and will travel through the anodes of the photodiode. The distribution of the photocurrents through the anode X1 and X2 is inversely proportional to the distance between the light spot and the corresponding anode. This means that if the light spot is closer to the anode X1, the photocurrent will be greater at X1 compared to X2. The proportional generated photocurrents can therefore be used to calculate the center-of-mass of the light spot.

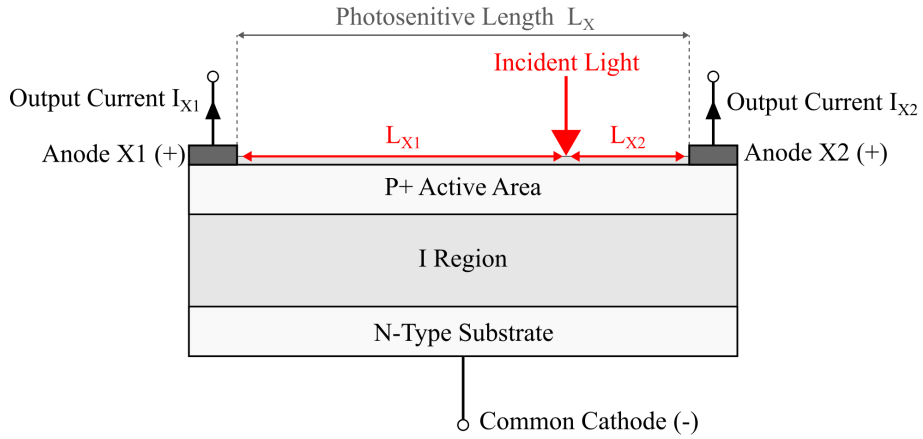

Figure 2.4: Cross-section of a Position Sensitive Device. A light spot hitting the PSD will make photocurrents flow out of the two anodes. The differences in the two photocurrents can be measured and used to calculate the position of the light spot.

2.2.1 2D Tetra-Lateral PSD

The 2D tetra-lateral PSD can measure the position of a light spot in two dimensions. The structure of this device is the same as the one-dimensional PSD. However, this device has four electrodes on the P-layer instead of two. The functionality of a 2D tetra-lateral PSD is presented in Figure 2.5.

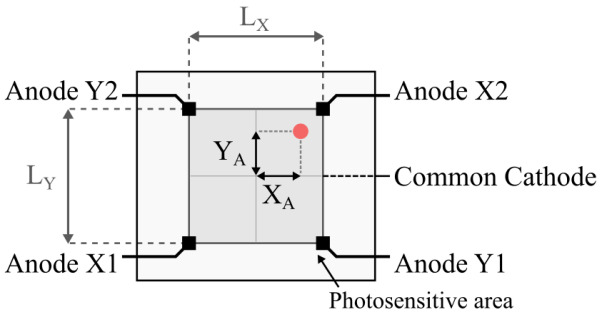

Figure 2.5: Figure displaying the functionality of a 2D tetra-lateral Position Sensitive Device. The PSD has four anodes and one common cathode. By measuring the different photocurrents flowing through the four anodes, the position of the light spot can be found using Equation (2.1) and (2.2).

The sensor has four anodes and one common cathode. By measuring the different photocurrents flowing through the four anodes, the position of the light spot can be found using Equation (2.1) and (2.2). Inputting the four photocurrents on the left side of the equations will calculate a relative X and Y-value. This value will range from -1 to 1, where -1 and 1 represent the edges of the photosensitive area and 0 represent the middle. The actual position of the center-of-mass of the light spot can be found by multiplying this value with the length of the photosensitive area, divided by 2.

$$\frac{(I_{X2}+I_{Y1})-(I_{X1}+I_{Y2})}{I_{X1}+I_{X2}+I_{Y1}+I_{Y2}}=\frac{2X_A}{L_X} \tag{2.1}$$

$$\frac{(I_{X2}+I_{Y2})-(I_{X1}+I_{Y1})}{I_{X1}+I_{X2}+I_{Y1}+I_{Y2}}=\frac{2Y_A}{L_Y} \tag{2.2}$$

For a 2D PSD to measure the correct position of a laser beam, the whole laser spot needs to be within the photosensitive area. As the position obtained from the PSD is the center-of-mass of the laser spot, the size and shape of the laser spot is irrelevant. However, the laser spot size must be smaller than the photosensitive area for the PSD to detect a position change of the laser spot.

2.3 Transimpedance Amplifier

A Transimpedance Amplifier (TIA) can be used to convert a low-level current from a sensor, which can be hard to detect, into a more easily detectable voltage. A simple configuration of a TIA is depicted in Figure 2.6. An op-amp is configured with a resistor between the inverting input and the output of the op-amp. When a current generating device, e.g. a photodiode, is connected to the inverting input of the op-amp, a voltage is generated at the output.

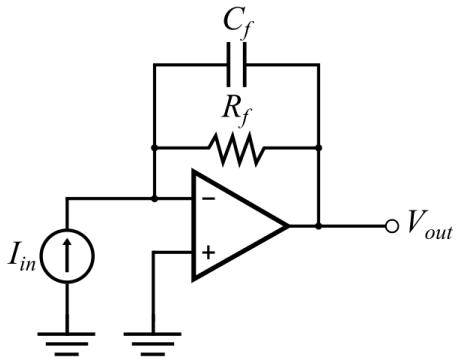

Figure 2.6: Simple Transimpedance Amplifier configuration. The TIA can be used to convert an input current, I_{in}, into a measurable output voltage, V_{out}. The gain resistor, R_f, will decide the amplification of the output voltage.

The resistor value, R_f, will decide the amplification of the output voltage. When the non-inverting input is grounded, as in Figure 2.6, the output voltage, V_{out}, can be calculated by Equation (2.3). This will generate a negative output voltage when a current is applied to the inverting input. If a positive output voltage is required, the non-inverting input can be set to a voltage reference, V_{ref}. The output voltage can then be calculated by Equation (2.4). Note that in this case, when no current is supplied to the input, the output voltage is equal to the voltage reference. Supplying an input current will still result in a decrease of the output voltage.

$$V_{out} = -I_{in}R_f \tag{2.3}$$

$$V_{out} = V_{ref} - I_{in}R_f \tag{2.4}$$

An optional capacitor, C_f, can be placed in parallel with the resistor, R_f. This will work as a low pass filter, where the amplification of signal frequencies over the cutoff frequency, f_c, will be reduced. The cutoff frequency of the system can be calculated by Equation (2.5). Note that this equation can be rearranged to find a fitting capacitor value based on the resistor value and the preferred bandwidth of the system.

$$f_c = \frac{1}{2\pi R_f C_f} \tag{2.5}$$

Chapter 3

Test Setup Development

This chapter will present the idea, challenges, and the development of the test setup for the optical sensor system.

3.1 General Idea of the Test Setup

The motivation for making a test setup was to allow for an easier development process. By using a test setup, the system can easily be tested in a controlled environment. Furthermore, the system can be iterated based on the test results and other requirements.

The objective of the test setup is to measure the movement of a steel pipe. This being the deflection of the pipe when one end is mounted and a force is applied to the other end. In addition, the system must be able to measure vibrations at the end of the pipe.

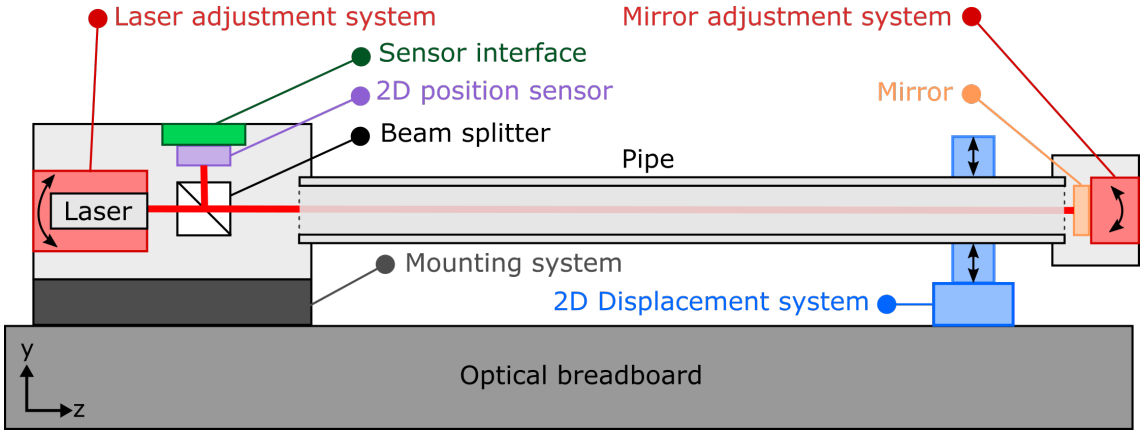

Figure 3.1: General idea of the test setup. The idea is based on the basic concept of the sensor system presented in Section 1.2. A pipe is used to simulate a cutting tool. One end of the pipe is mounted to an optical breadboard, while the other end is hanging free. Applying a force at the free end will make the pipe deflect similar to a cutting tool.

The general idea for the test setup is depicted in Figure 3.1. The idea is based on the basic concept of the sensor system presented in Section 1.2. In order for a pipe to deflect when a force is being applied to one end, the other end needs to be fixed. In this setup one end of the pipe is mounted to an optical breadboard, while the other end is hanging free. An applied force at the free end of the pipe will simulate the cutting forces being applied to a cutting tool, as illustrated in Figure 1.2.

The sensor system will use the same configuration as presented in Section 1.2 to measure the deflection of the pipe. The mirror is mounted at the free end of the pipe, while the rest of the system is mounted at the fixed end of the pipe. The deflection of the pipe will cause the laser beam to be reflected from the mirror at a slightly different angle. This angle change will result in a change in the position of the laser beam. The position change of the laser beam will be measured by a 2D position sensitive device. The measured position change can then be used to calculate the deflection of the pipe.

By mounting the whole system to an optical breadboard, it is possible to perform measurements in a controlled environment. A displacement system can be placed at the free end of the pipe to deflect the pipe in controlled and precise steps. This can be used to test the system, but also calibrate it. By applying known deflections of the pipe and measuring the different positions of the laser beam, the relationship between the deflection of the pipe and the position of the laser beam can be found. This relationship can then be used when calculating the deflection of the pipe.

3.1.1 Cutting Tool Implementation

There are several ways one could implement the sensor system to a cutting tool. The main requirement for the sensor system to work, is that the angle of the mirror must correspond to the deflection of the cutting tool. The mirror must therefore follow the curvature of the cutting tool. Figure 3.2 illustrates how a modified version of the test setup could be placed inside a cutting tool. For this setup to work, the pipe containing the sensor system must follow the exact same curvature of the cutting tool. This means that the sensor system must be properly mounted inside the cutting tool. A major issue with this configuration, is the limited space inside a cutting tool. The space inside a cutting tool will depend on the size of the cutting tool, but is generally very limited. Miniaturisation must therefore be prioritised for the setup to be implemented inside the cutting tool.

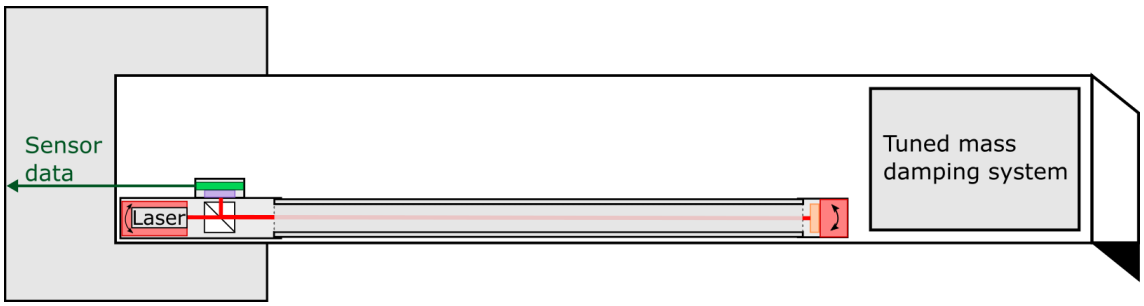

Figure 3.2: Idea of how the test setup can be used in a cutting tool. The test setup must be mounted so the pipe follows the curvature of the cutting tool.

The implemented sensor system in Figure 3.2 uses a steel pipe in the same way as the test setup depicted in Figure 3.1. The sensor system can also be used without the pipe, by mounting the optical components directly inside the cutting tool. This might reduce the required space inside the cutting tool. However, using the pipe configuration might also have some advantages. Some of the optical components will require adjustment systems to properly align the laser beam. This will be further explained in Section 3.2.2. By using the setup containing a steel pipe, the sensor system is independent of the cutting tool. This means that the laser beam can be properly aligned before inserting the sensor system into the cutting tool. This can be very advantageous as adjusting anything inside the cutting tool might be a difficult task.

Another possible configuration is to mount the sensor system on the outside of the cutting tool. The use of a steel pipe will then be advantageous, as the laser beam might be blocked or disturbed by flying metal scrap from the cutting process. The size of the sensor system will also be important in this configuration, as the size will add to the overall diameter of the cylindrical cutting tool and might therefore limit the smallest hole diameter a turning tool can operate at.

3.2 Optomechanical Challenges

3.2.1 Pipe Deflection vs. Laser Beam Displacement

As presented in Section 3.1, the position of the laser beam will change depending on the current deflection of the pipe. Figure 3.3 illustrates an undeflected pipe. The laser beam coming from the left side will be split into two parts when it reaches the beam splitter. One part will go forward through the beam splitter, while the other part will be reflected upwards. The laser beam going forward will hit the mirror at the opposite end of the pipe and be reflected directly back, due to the angle between the laser beam and the mirror being 90°. The reflected laser beam will once again be split into two new laser beams. The laser beam being reflected downwards will hit the 2D PSD. For the type of beam splitter used in this project, the optical power of the original laser beam will be split equally for the two new laser beams created. This means that the laser beam hitting the 2D PSD will only possess 25% of the original laser beam's optical power, as it passes two times through the beam splitter.

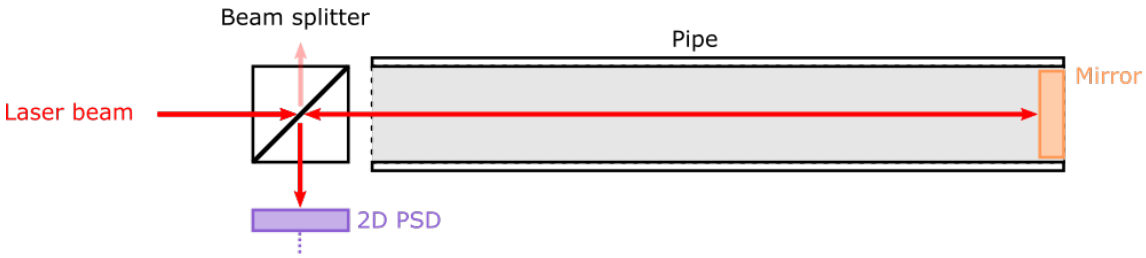

Figure 3.3: Figure displaying the laser beam path with an undeflected pipe. The laser beam will travel through the pipe and be reflected back by a mirror. A beam splitter is used to direct the laser beam onto the PSD.

As the pipe gets deflected, as illustrated in Figure 3.4, the position of the laser spot hitting the sensor will change. This is the foundational principle of the sensor system. The ratio between the pipe deflection and the laser beam displacement is essential to know, as the system will calculate the pipe deflection from the measured laser beam displacement.

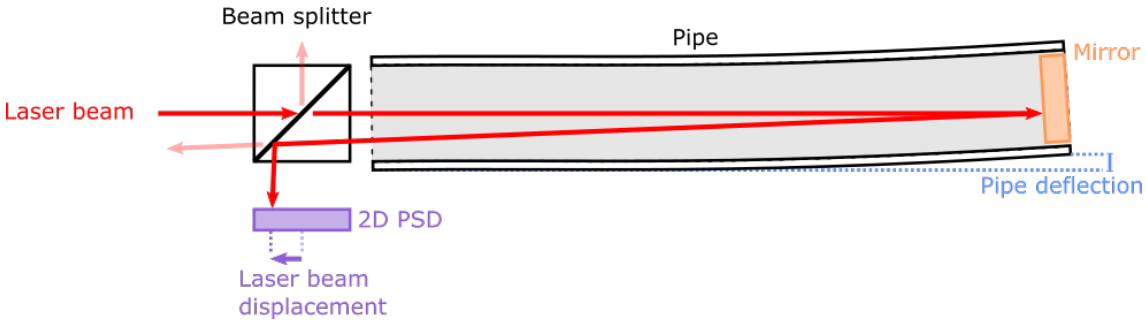

Figure 3.4: Figure displaying the laser beam path with a deflected pipe. A deflection of the pipe will cause the laser beam to be reflected back at a slightly different angle. This can be detected as a change of the laser spot position on the PSD.

During this project, two different methods have been utilised for finding the displacement-deflection ratio. One of the methods was to apply known deflections to the pipe and measure the position of the laser beam. By repeating this process for many different deflection values, a function for converting the measured laser spot displacement to the estimated pipe deflection can be found using regression. The second method was to do a theoretical analysis in order to find the ratio.

Theoretical Analysis

The goal of the theoretical analysis was to find the ratio between the laser beam displacement and the pipe deflection. The analysis was performed in two steps. First, finding the relationship between the displacement of the laser spot and the angle of the mirror. Then, using this mirror angle to estimate the deflection of the pipe.

Figure 3.5 shows the result of a trigonometrical analysis for finding the relationship between the mirror angle and the laser beam displacement. D_6 in this figure represents the displacement of the laser beam, while θ_{mirror} represents the angle of the mirror. The equations stating the relationship between D_6 and θ_{mirror} can be found in Appendix D.

After finding the mirror angle, the next step was to use this to find the deflection of the pipe. This required a mechanical analysis. As previously mentioned, the pipe is fixed in one end, while the other is hanging free. In addition, the forces that make the pipe deflect is applied at the very end of the pipe. The setup was therefore considered to be a cantilever with a single end load, when doing the mechanical analysis.

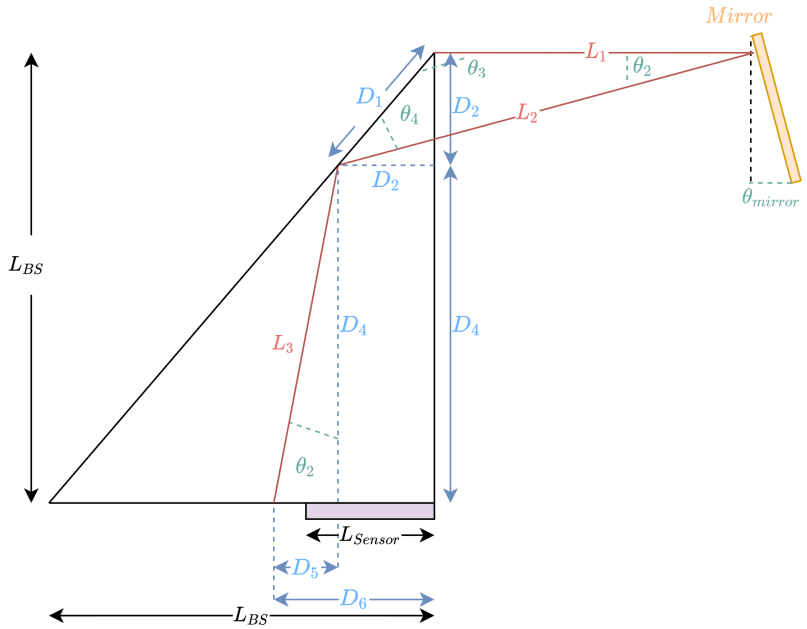

Figure 3.5: Trigonometrical figure of the test setup. A change in the mirror angle, θ_{mirror}, will result in a change of the laser spot displacement, D_6.

Figure 3.6 illustrates the deflection of a cantilever with a single end load. The load is represented by a force F pushing down on the cantilever. The applied force will make the cantilever deflect. δ_{max} in this figure represents the deflection of the cantilever at the very end. While θ_{max} represents the slope of the cantilever at the same point. By knowing the length of the cantilever, it is possible to calculate the end slope based on the end deflection, or vice versa. The equations used to explain these relations are presented in Appendix E, along with equations for finding the deflection or the slope at any given point along the cantilever. For example, these equations are useful when placing the sensor system inside a cutting tool, as depicted in Figure 3.2. When placing the sensor system inside the cutting tool the length of the pipe will not be the same as the length of the cutting tool. It will therefore be essential to convert the deflection of the pipe to the deflection of the actual cutting tool.

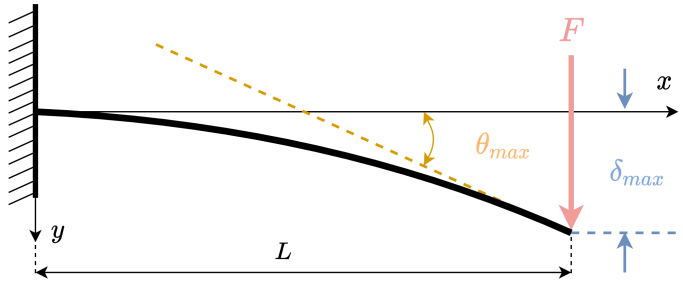

Figure 3.6: Beam deflection of a cantilever with a single end load. Where θ_{max} is the end-slope of the pipe when it is deflected δ_{max} due to a force F.

Trigonometrical Simulations

Using the trigonometrical equations previously presented, a script in MATLAB was developed to simulate the system. This script can be used to display the laser beam path at different deflection values of the pipe. Settings like the pipe length and inner radius can also be changed to simulate different pipes. This simulation was very beneficial for giving a good graphical representation of the system, especially of how the deflection value would change the position of the laser beam. The simulation was also very useful when dimensioning the test setup, which will be presented in Section 3.2.3.

Trying several different settings in the simulation revealed some important aspects of the system. One being the length of the pipe. As Figure 3.7 depicts, the length of the pipe will be irrelevant for measuring a given deflection value. This means that a 50 cm long pipe and a 500 cm long pipe with the same end-deflection will result in almost the same laser beam displacement. This is due to the end-deflection δ_{max} and the end-slope θ_{max} being proportional for a cantilever with a single end load.

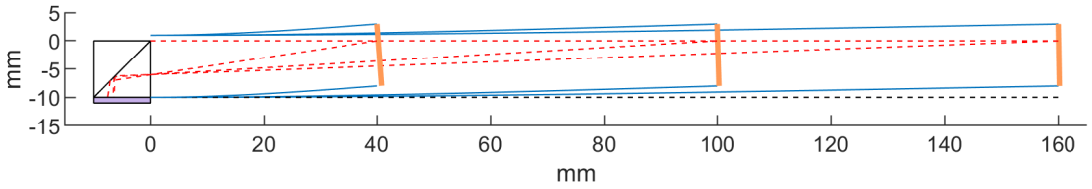

Figure 3.7: Simulation of different pipe lengths. The length of the pipe, while the end-deflection is constant, have close to zero impact on the laser position. This is due to the end-deflection δ_{max} and the end-slope θ_{max} being proportional for a cantilever with a single end load. The laser beams will intersect in X=0, where the pipe starts.

The simulations also revealed that the position of the mirror has a huge impact on the deflection-displacement ratio. Figure 3.8 depicts the effect of changing the position of the mirror within the pipe. Placing the mirror further inside the pipe, will change the angle of the mirror, which again will change the displacement of the laser beam. It is important to note that the sensor now effectively measures the displacement of the pipe at the position of the mirror. However, by knowing the distance from the mirror to the free end of the pipe, it is possible to calculate the end deflection of the pipe. This principle can be used to increase the measurement range of a system. Moving the mirror closer to the fixed end will allow the system to measure greater deflection values, using the same sensor area. An important aspect to be noted is that this will distribute the sensor's resolution over a greater measurement range, which will lower the deflection measurement resolution.

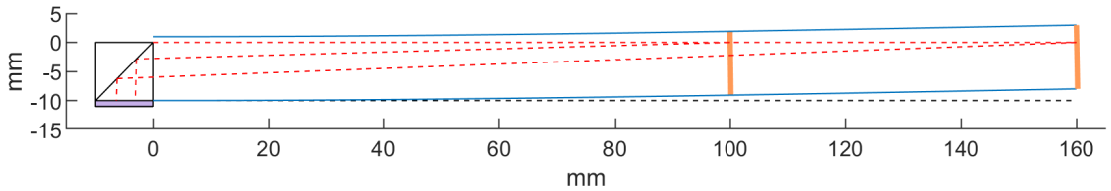

Figure 3.8: Simulation where the position of the mirror is changed while the pipe length is constant. Moving the mirror will change the angle of the mirror, which again will change the displacement of the laser spot.

3.2.2 Aligning the Laser Beam

A critical challenge of this sensor system is the alignment of the laser beam. After assembling the setup, there is a fairly high probability that the laser is not hitting the sensor area. There can be different reasons for this, one being an error with the laser diode. Collimated laser diodes often have an axis deviation associated with them. The axis deviation is the angle difference between the actual laser beam path and an ideal perpendicular path. The axis deviation of a collimated laser diode will result in the laser beam not going straight forward. The second reason for the laser beam not hitting the sensor, is errors associated with the mechanical components. Due to limited precision of cutting tools, manufactured mechanical components will always have a margin of error. This can result in the optical components in the setup not being fully aligned with each other.

To mitigate the possible errors, mechanical adjustment systems for both the laser and the mirror were implemented. The adjustment of the laser allows the laser beam to hit the mirror at a desired position, while the adjustment of the mirror will allow the laser beam to be reflected and hit the sensor area at a desired position. This is very advantageous, as it allows for adjustments to the measurement range of the system, as depicted in Figure 3.9.

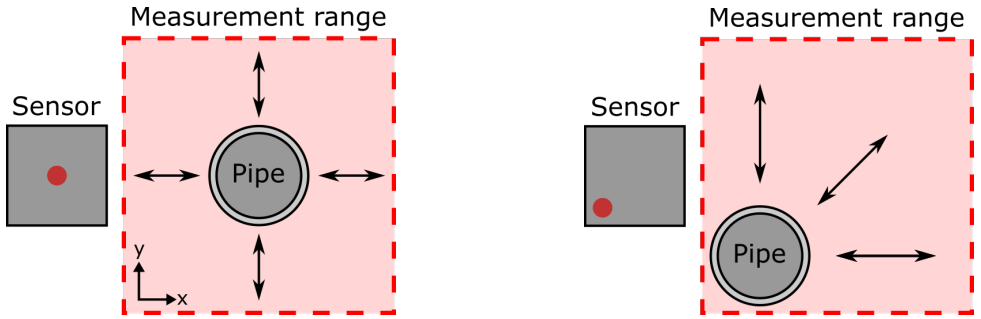

(a) A laser beam aligned in the middle of the sensor area will distribute the deflection measurement range equally around the pipe.

(b) A laser beam aligned in the corner of the sensor area will shift the measurement area to the corresponding quadrant in relation to the cross-section of the pipe.

Figure 3.9: The deflection measurement range of the pipe can be shifted by aligning the laser beam differently on the sensor area.

The initial alignment of the laser beam will decide the measurement range of the system. In Figure 3.9a, the laser beam is aligned to the middle of the sensor, when the pipe is undeflected. The pipe can then be deflected equally in every direction. The shape of the measurement area will be the same as the shape of the sensor area.

Another possibility is to align the laser beam to a corner of the sensor area, as depicted in Figure 3.9b. This will limit the measurement range of the system to one quadrant relative to the cross-section of the pipe. This can be very beneficial when the sensor system is being used in a cutting tool, as the cutting forces applied to a turning tool will make the tool deflect mostly within one quadrant. The sensor system's measurement range can therefore be shifted to measure bigger deflections in this quadrant.

3.2.3 Dimensioning the Test Setup

Designing a sensor system for Sandvik Coromant's turning tools can be challenging as their tool lineup includes a huge range of different sized cutting tools. As presented in Section 3.2.1, the length of the pipe will be insignificant as long as the end deflection of the pipe is the same. For the implementation into a cutting tool, this effectively means that a sensor system dimensioned for a specified tool can also be used for different sized tools. This is true as long as the distance proportion between the beam splitter, mirror and cutting tip stays the same. This means that a sensor system that is dimensioned to detect up to 1 mm deflection of a 30 cm long tool, can be used to detect the same 1 mm deflection of a 300 cm long tool.

However, the diameter of the cutting tool is also important to consider, as the cutting tool diameter will limit the overall size of the sensor system. When setting requirements for the test setup, an overall size limitation was not set. This was due to the fact that the main purpose of the test setup was to test the general functionality of the system. The setup could therefore be developed quicker and easier, as miniaturising the system was not a key focus. The miniaturisation of the system should be considered in a later stage of the development process.

Based on the requirements presented in Section 1.3.1, the test setup was set to measure deflections of a pipe with the length of 500 mm, within the deflection measurement range of 2 mm x 2 mm. Note that this specifies the total deflection range. So, if the laser spot is placed in the corner of the sensor, as depicted in Figure 3.9b, the measurement range in the X-axis will be 0 mm to 2 mm. However, if the laser spot is to be placed in the middle of the sensor, as depicted in Figure 3.9a, the measurement range for the X-axis will be −1 mm to 1 mm.

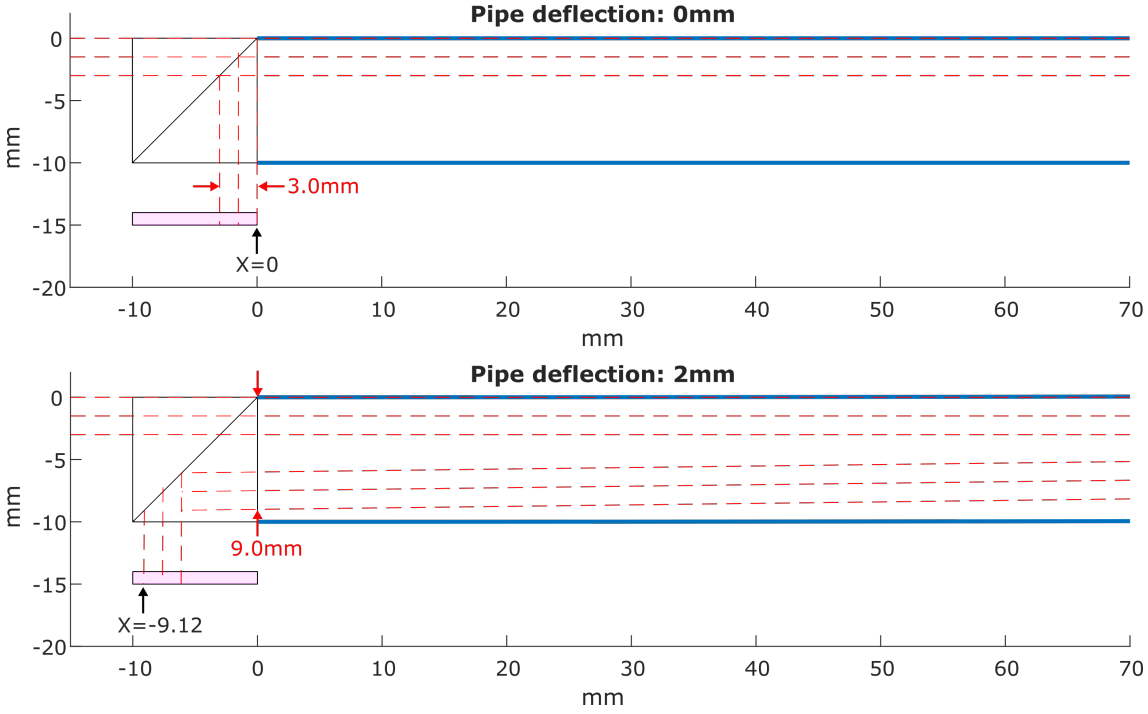

Figure 3.10: Simulation results for a pipe with the length of 500 mm. In the upper graph, the pipe has no deflection. In the lower graph, the pipe is deflected 2 mm at the opposite end. 2 mm deflection of the pipe results in a 6.12 mm position change of the laser spot on the sensor side.

The length of the pipe and the deflection measurement range was used to simulate the system, using the MATLAB script mentioned in Section 3.2.1. In addition to these parameters, a beam splitter with the area of 10 mm × 10 mm and a laser beam with a beam diameter of 3 mm was also defined. These values are based on the components tested earlier in the project. The simulation results for a pipe with the length of 500 mm and an end-deflection of 2 mm is illustrated in Figure 3.10.

It is important to note that this simulation is only considering one measurement axis. However, because all of the components in this setup are either round or square, the two measurement axes should theoretically be identical. In the simulation graphs, the pink rectangle is representing the sensor measurement range. In the upper graph the pipe is undeflected and the laser beam is aligned so it hits the edge of the sensor's measurement range. In the lower graph, the pipe is deflected 2 mm upwards. This is resulting in a 6.12 mm displacement of the laser spot. For a position sensor to measure the correct position, the whole laser spot needs to be within the sensor area. The required sensor measurement range in this scenario is therefore 6.12 mm plus the laser beam diameter of 3 mm, which equals 9.12 mm.

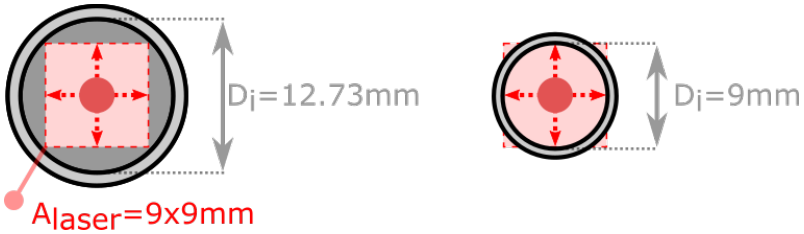

Figure 3.11: Required laser beam movement range illustrated within the cross-section of the pipe. A movement range of 9 mm × 9 mm will require a pipe with a minimum inner diameter of 12.73 mm. An inner pipe diameter lower than this will limit the movement range of the laser.

Another important result that this simulation reveals, is the minimum inner pipe diameter that is required. A too small pipe diameter will result in the laser beam being blocked due to the pipe's deflection. From the simulation results we can see that the pipe needs to have at least an inner diameter of 9.0 mm. However, this is only in one measurement axis. If this is to be applied to both measurement axes, the area within the cross-section of the pipe would have to be at least 9 mm × 9 mm, as illustrated in Figure 3.11. In order for the pipe to not block the laser when the pipe is deflected somewhere in the range of 2 mm × 2 mm, the pipe needs to have an inner diameter of 12.73 mm. Using a pipe with an inner diameter of 9 mm, will limit the system to only measure deflections within a circular measurement area with a diameter of 2 mm.

3.3 Optical Components

The mechanical components had to be specifically designed to fit with the optical components. The optical components were therefore chosen first. Firstly, the position sensor and the laser diode were chosen, as these are considered to be the two most important components of the system. Secondly, the mirror and the beam splitter were selected based on the position sensor, laser diode, and the system requirements.

3.3.1 Optical Position Sensor and Laser Diode

The optical position sensor chosen was the 2D tetra-lateral Position Sensitive Device (PSD), S5991-01 from Hamamatsu [5]. The laser diode chosen was the collimated laser diode module, CPS635R [6] from Thorlabs. This combination was preferred as it would match the required laser spot displacement range well. It was found from the simulations that the sensor must be able to detect laser spot displacements in a range of 6120 µm × 6120 µm, in order for the system to detect pipe deflections in the range of 2 mm × 2 mm. With a laser beam diameter of 2900 µm and a sensor area of 9000 µm × 9000 µm, the system can measure displacements of the laser in a range of 6100 µm × 6100 µm. The reason why the displacement range is lower than the sensor area, is because the whole laser spot needs to be within the sensor area for accurate measurements.

The spectral response of the PSD ranges from 320 to 1100 nm. The peak sensitivity of the sensor is at 960 nm with a photosensitivity of 0.6 A/W. For the wavelength of the CPS635R at 635 nm, the sensitivity is about 0.4 A/W, which will be more than sufficient. With an optical power of 1.2 mW in the laser beam, the total photocurrent generated from the PSD will be 480 µA. However, due to the 25% reduction in laser beam effect caused by the beam splitter, the total generated photocurrent will be 120 µA. The dark current of the sensor is rated at about 200 pA with no bias and increases with a reverse voltage. The terminal capacitance of the sensor is rated at 1 nF at zero bias and decreases with a reverse voltage.

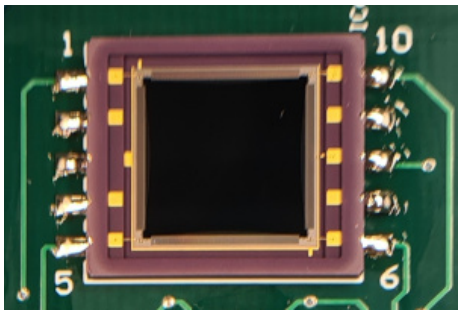

Figure 3.12: Picture of the PSD S5991-01 soldered to a PCB. The sensor has a photosensitive area of 9 mm × 9 mm and a package size of 16.5 mm × 14.5 mm × 1.26 mm

Another reason for choosing the S5991-01 PSD was the component package. The sensor has a low profile build and is fairly small sized relative to its photosensitive area. In addition, it is a Surface Mount Device (SMD) which allows it to be mounted on a PCB, while keeping the overall size of the PCB small.

3.3.2 Beam Splitter and Mirror

The size of the beam splitter must at least be as big as the photosensitive area of the PSD. As the photosensitive area of the chosen PSD was 9 mm × 9 mm, the size of the beam splitter was set to be 10 mm × 10 mm × 10 mm. The optical mirror was selected to be circular with a diameter of 9 mm.

3.4 Sensor Interface

For the position sensor to be used in the sensor system, additional electronics were required to support it. The measurement signals from the S5991-01 PSD are four relatively weak photocurrents. These can be hard to measure precisely and will therefore require a transimpedance amplifier circuit, as presented in Section 2.3. The TIA circuit will convert the weak current signals into easily measurable voltages. After converting the photocurrents to voltages, a sampling circuit is required to digitalise the signals. Furthermore, the digital measurement signals need to be processed and displayed to the user of the system. This section will present the initial sensor interface developed for the PSD.

3.4.1 Transimpedance Amplifier Circuit

Figure 3.13 depicts a simplified model of a 2D tetra-lateral PSD. The PSD can be considered as four separate photodiodes with a common cathode. The sensor will generate four photocurrents which will flow out through the four anodes of the PSD. The amplifier circuit will therefore require four identical transimpedance amplifiers, as the one depicted in Figure 2.6.

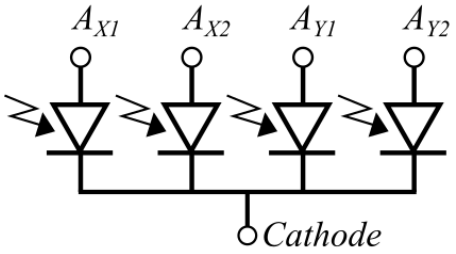

Figure 3.13: Simplified model of a 2D tetra-lateral PSD. The PSD can be considered as four separate photodiodes with a common cathode. In order to extract the four separate photocurrents, need the four anodes of the PSD to be connected to four separate TIAs.

A photodiode can either be connected with the anode or cathode to the inverting input of the op-amp. The difference will be the direction of the photocurrent and therefore the polarity of the voltage potential generated from the photocurrents. However, due to the PSD having a common cathode, it is only possible to connect the anodes of the photodiodes to the inputs of the transimpedance amplifiers. This will make the photocurrents flow from the photodiodes and through the gain resistors. The contribution from the photocurrents to the output voltage of the TIA, will therefore have a negative polarity, as seen in Equation (2.3) and (2.4). This means that the output voltage of the TIA will decrease with an increase in the corresponding photocurrent.

Mode of Operation

In Section 2.1.2 it was presented that a photodiode can be configured in two different modes; Photovoltaic and photoconductive mode. It is stated that photoconductive mode is preferred for high speed applications. Whereas the photovoltaic mode is better suited for precision applications, where low noise is important. As the resolution of the position measurements is

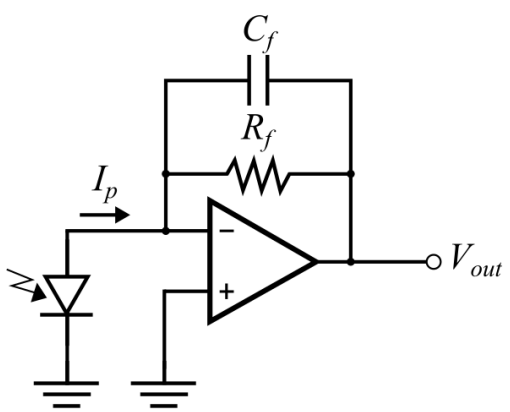

(a) Cathode and non-inverting input of the op-amp connected to ground.

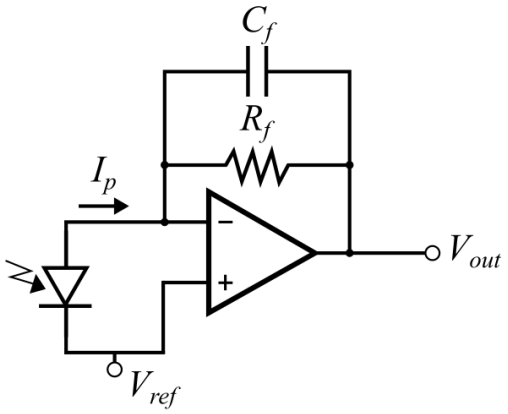

(b) Cathode and non-inverting input of the op-amp connected to a voltage reference.

Figure 3.14: Two different transimpedance amplifier configurations for using the photodiode in photovoltaic mode. The inverting terminal of the op-amp will be forced to the same voltage potential as the non-inverting terminal. This results in zero voltage potential over the photodiode.

one of the most important factors, and the vibrations that are required to be measured is only up to 500 Hz, the photovoltaic mode seemed like the best choice for this application.

The photovoltaic mode is achieved when there is no voltage potential over the photodiode. In the transimpedance circuit this can be achieved by connecting the anode of the photodiode to the inverting input of the op-amp, as discussed earlier. In addition, the cathode of the photodiode and the non-inverting input of the op-amp must be connected to ground, as depicted in Figure 3.14a. An op-amp will always try to keep its two inputs at the same voltage potential. This means that the inverting input of the op-amp will also be grounded, resulting in the voltage potential over the photodiode being zero due to a ground potential on both the anode and the cathode.

When using this configuration, the output voltage can be found from Equation (2.3). This means that when no photocurrent is present, the output voltage V_{out} will be zero. However, when the photocurrent increases, the output voltage will decrease to a negative voltage potential. In order for this to work, the op-amp must have the functionality to output a negative voltage. The output range of an op-amp is often limited to its supply voltage and would therefore require a supply voltage from $-V_{cc}$ to $+V_{cc}$. This can be achieved by a bipolar power supply. The use of a bipolar power supply was not considered to be the most preferable option, as it often will require more components to be realised and therefore more space on the PCB.

Another option is to connect the cathode and the non-inverting input of the op-amp to a voltage reference, as depicted in Figure 3.14b. The same will happen here, where the inverting terminal of the op-amp will be forced to the same voltage reference. This will result in zero voltage drop over the photodiode. The output voltage of the TIA for this configuration can be expressed using Equation (2.4). From this we can see that the voltage reference, V_{ref}, will be added to the output voltage, meaning that the output voltage will still decrease with the increase of the photocurrent, but be equal to V_{ref} when the photocurrent is zero. Using this configuration with an unipolar power supply delivering a higher supply voltage than V_{ref}, allows for an output voltage from 0V to V_{ref}.

AS89000 - Four-channel Transimpedance Amplifier

After researching different transimpedance amplifier solutions, the AS89000 [7] from AMS was identified as the preferred one. This is a four-channel programmable gain transimpedance amplifier. This means that four amplifier circuits are fit within one Integrated Circuit (IC). In addition, the gain of the amplifier can be chosen by setting different pins on the IC high or low. The gain is chosen by selecting different resistor values of R_f. The IC has 8 different stages ranging from 25 kΩ to 20 MΩ. An advantage with using an IC like this, is the small SMD package. Another solution could have been to use a four-channel op-amp in combination with four external resistors and capacitors.

The max photocurrent that could be generated on one channel of the PSD was calculated to be 120 µA. This includes the four times reduction of the laser effect due to the laser passing through the beam splitter two times. A resistor value, R_f, of 41.6 kΩ is preferred when using a supply voltage of 5 V for the transimpedance amplifiers. This resistor value ensures the output voltage being scaled perfectly with the input current. An input current of 0 µA would produce an output voltage of 5 V. The max input current of 120 µA would then produce an output voltage of 0 V.

A disadvantage of this solution is that the preferred 41.6 kΩ resistor value can not be chosen. The closest stage of the AS89000 would be the lowest resistor value of 25 kΩ. This will give an output voltage range from 5 V to 2 V based on the input photocurrent from 0 µA to 120 µA.

3.4.2 Sampling Circuit and Data Processing

One of the goals of this project was to develop a complete sensor interface. This means developing a PCB containing the sensor and other required circuitry for digitalising and transferring the measurement data to a computer. Due to time constraints, only the position sensor and the transimpedance amplifier circuit were included on the PCB of the first sensor interface iteration. This was considered preferable from a the development process view. Consequently, the performance of the sensor could be tested and analysed before deciding on the required sampling circuitry.

To digitalise the analogue measurement signals from the TIA, a Data Acquisition (DAQ) device from National Instruments was chosen. This module contains a 4-channel 16-bit Analogue-to-Digital Converter (ADC) and can be connected to a computer through USB. This made it easy to process and display the measurement data from the sensor system in real-time using LabVIEW.

A LabVIEW program was developed to import the four voltages digitalised by the ADC. The four signals were used to calculate the X and Y-position of the laser spot. In addition, the program can capture the X and Y-values, and save them to a measurement file. This file can later be used to analyse the noise and find the position resolution of the sensor system.

The formulas implemented into LabVIEW, which was used to calculate the X and Y-position of the laser, are displayed in Equation (3.1) and (3.2). Note that the X and Y-values calculated from these equations are the relative position, meaning that X and Y will range from -1 to 1. From the datasheet of the sensor, it is suggested that these relative positions can be multiplied with half of the sensor area length to find the absolute position. For the S5991-01 with a

sensor area length of 9000 µm, a relative position of 1 would translate to an absolute position of 4500 µm. A relative position of -1 would translate to an absolute position of −4500 µm.

$$\frac{(V_{X2}+V_{Y1})-(V_{X1}+V_{Y2})}{V_{X1}+V_{X2}+V_{Y1}+V_{Y2}} = X\,(relative\,position) \tag{3.1}$$

$$\frac{(V_{X2}+V_{Y2})-(V_{X1}+V_{Y1})}{V_{X1}+V_{X2}+V_{Y1}+V_{Y2}} = Y\,(relative\,position) \tag{3.2}$$

Upon testing, it did become apparent that the calculation of the absolute position would not work, as the relative position never came close to 1 or -1. A laser beam position on the very end of the sensor area would only produce a relative position of about 0.6 or -0.6. A possible explanation to this is the laser spot diameter. When the center-of-mass of the laser spot is placed at an edge of the sensor, only half of the laser spot will touch the sensor area. The center-of-mass of the laser spot is therefore different from the view of the sensor. Choosing a laser beam with a smaller spot diameter will possibly reduce this error.

Due to the position error, the relative position was not multiplied with the sensor length. Instead, the sensitivity curve for the given configuration was found through measurements. The sensitivity curve can be used to convert the measured relative position to an estimate of the absolute position. These measurements are presented in Section 4.1.

3.4.3 PCB with the Initial Sensor Interface

A PCB was preferable as it would make the integration of the sensor in the mechanical setup much easier, versus using a breadboard setup. As the sampling circuit was chosen to be an external data acquisition device, the components required for the PCB were the position sensor and the amplifier circuit. The circuit diagram for the sensor interface is depicted in Figure 3.15.

The two main components of this circuit are the PSD, S5991-01, and the TIA, AS89000. The sensor has five important pins, the four anodes (X1, X2, Y1 and Y2) and a common cathode. The rest is not connected, (NC). As presented in Section 3.4.1, the sensor is to be configured in photovoltaic mode and the cathode should therefore be connected to a voltage reference, V_{ref}. The circuit is designed for an input voltage, V_{dd}, equal to 5 V. A voltage divider is implemented to create a slightly lower V_{ref}. With $V_{dd} = 5\,\text{V}$, $R1 = 1.5\,\text{k}\Omega$ and $R2 = 13.7\,\text{k}\Omega$, the reference voltage, V_{ref}, will be approximately 4.5 V. The voltage reference is also connected to the VREF terminal of the AS89000. This is because the VREF terminal of the AS89000 is connected to the non-inverting inputs of the four TIAs. The reason for the voltage reference being slightly lower than the supply voltage, is because the op-amp of the transimpedance amplifiers can not exactly output a voltage that is identical to the supply voltage. The max voltage that the op-amps can output will always be slightly lower than the supply voltage. In order to avoid problems related to this phenomenon, the reference voltage was lowered to 4.5 V, which the op-amps has no problem outputting.

Two decoupling capacitors are connected close to the terminal where the voltage supply is to be connected. The purpose of these capacitors is to filter out noise on the supply lines. Different capacitor values will target noise at different frequencies. SW1 to SW3 of the AS89000 are the

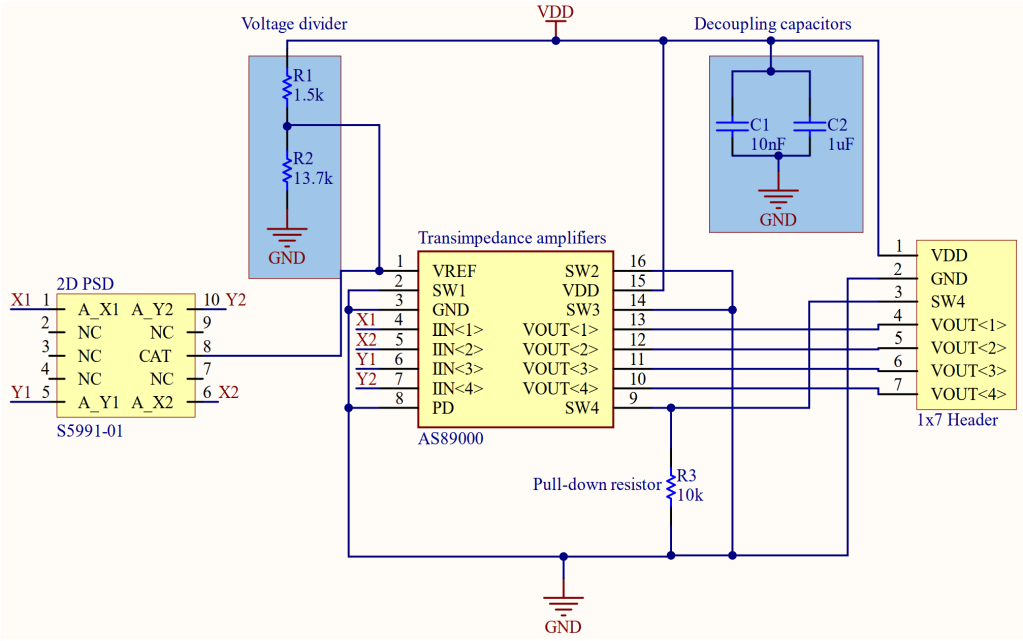

Figure 3.15: Circuit diagram of the initial sensor interface. The main components of the circuit are the position sensor and the four channel transimpedance amplifier. A voltage divider is implemented for supplying the circuit with a voltage reference of approximately 4.5 V.

pins that is used to program the resistor values of the amplifiers. By connecting them all to ground, the resistor value of 25 kΩ is chosen. SW4 chooses the value of the capacitor over the amplifiers. This pin is connected to the pin-header of the PCB, which makes it possible to change this value depending on the header-pin being connected to 5 V or ground. The four output voltages from the amplifiers can be accessed from the pin-header row.

In Figure 3.16 the layout of the PCB is depicted. A ground plane was incorporated into the back side of the PCB. There are several benefits of using a ground plane. Some of the major ones are possible improvements to the signal integrity and more resistance to interference. The size of the PCB is 3 cm × 3 cm.

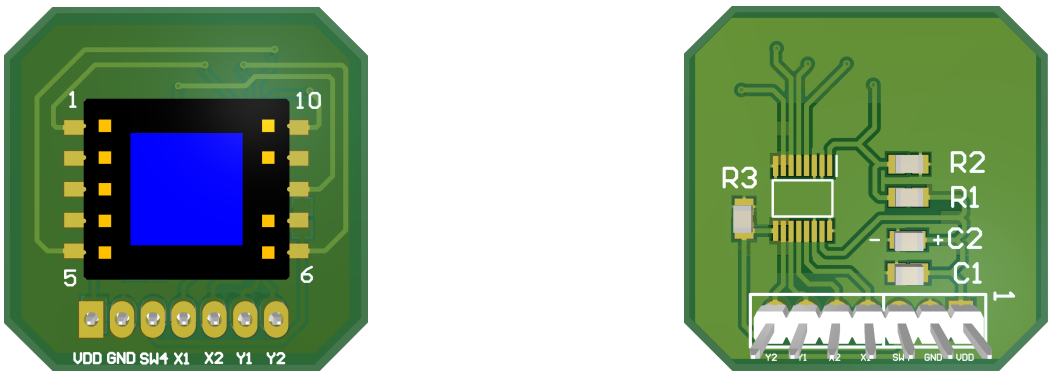

(a) Front side. **(b)** Back side.

Figure 3.16: 3D model of the PCB for the initial sensor interface. The size of the PCB is 3 cm × 3 cm. The four output voltages of the Transimpedance Amplifier can be measured from the pin-header row on the PCB.

3.5 Mechanical Solutions

As presented in Section 3.1, the test setup requires some mechanical components. Through collaboration with the engineers at Sandvik Coromant Trondheim, a mechanical system has been developed. The general flow of the development has been that the student have presented a general idea and some requirements for an aspect of the mechanical system. A mechanical engineer at Sandvik Coromant has then used this information to develop the specific solutions and design the required components. All components have been produced at Sandvik Coromant Trondheim.

Figure 3.17 depicts parts of the mechanical test setup. The setup is very similar to the general idea depicted in Figure 3.1. On the right side is the component housing the beam splitter and the laser diode module. Both the pipe and the housing have screw threads which make them easy to mount to each other. The housing is kept in place by a mounting component that is attached to the optical breadboard. At the opposite side of the pipe, the displacement system is attached. The displacement system makes it possible to bend the pipe in two axes with controlled increments down to 10 µm. The housing also includes an adjustment system for the laser, which is better depicted in Figure 3.18.

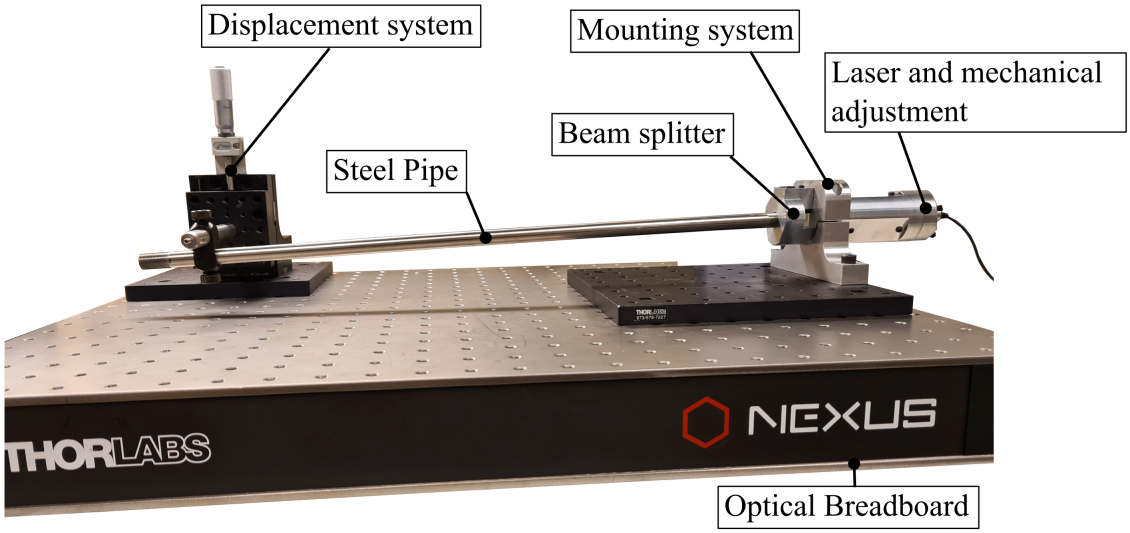

Figure 3.17: The mechanical parts of the test setup. The test setup is mounted on top of an optical breadboard to reduce unwanted vibration and to perform precise measurements. The displacement system can bend the steel pipe in two axes with controlled increments.

Inside the housing is a cylindrical component which is locked in place by one screw in the front. This is the golden component in the CAD model. This component is designed to house the laser diode module. There is a weakness in the front of the golden component which allows the back part of it to bend if exposed to mechanical pressure. So, by using the six adjustment screws, it is possible to bend the golden cylinder in a desired position. Since the laser will follow the movement of the golden cylinder, the laser beam will be angled due to this adjustment. This makes it possible to adjust the angle of the laser beam so it travels in parallel with the pipe.

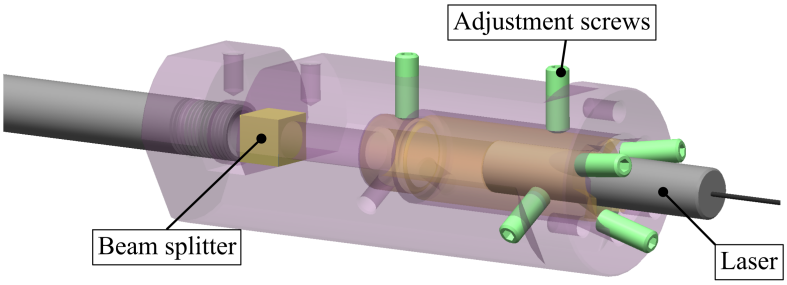

Figure 3.18: CAD model of the component housing the beam splitter and the laser diode module. Adjustment screws allow the laser beam to be aligned, securing that the laser beam goes in parallel with the steel pipe.

Figure 3.19 depicts the CAD model for the mirror mounting and adjustment system. The mirror is glued to the purple component. The purple component is attached to the transparent component using three screws. The use of o-rings between the two components allows for an angle difference between the two components, due to the flexibility of the o-rings. The mirror can therefore be adjusted to the preferred angle by tightening or loosening the three adjustment screws. The whole system is attached to the free end of the pipe by using screw threads.

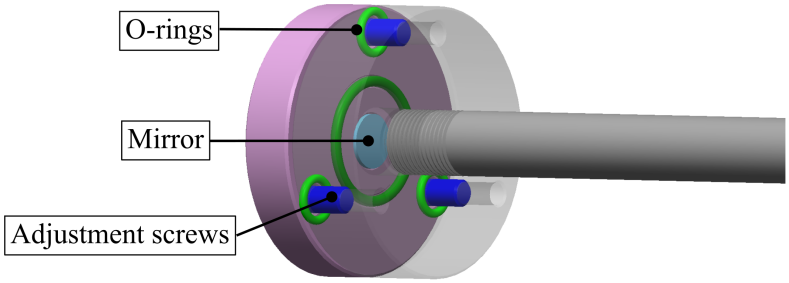

Figure 3.19: CAD model of the component housing the mirror. O-rings between the purple and the transparent component allows for small angle adjustment of the mirror.

Figure 3.20 depicts the mounting system for the PCB containing the position sensor. This system is clamped around the component housing the laser and the beam splitter. The clamping solution allow the sensor to be adjusted so the laser beam coming from the beam splitter will hit the sensor area.

Due to this being a first prototype, some of the mechanical components are not dimensioned fully after the requirements, and will therefore limit some aspects of the system. The pipe has an inner diameter of 10 mm. However, as stated in Section 3.2.3, the inner diameter of the pipe needs to be at least 12.73 mm in order for the laser beam to not be blocked when the pipe is within the deflection range of 2 mm × 2 mm. In addition, there is a cylindrical hole between the pipe and the beam splitter which has a diameter of 8 mm. This will most likely be the limiting factor of the mechanical setup, in terms of the measurement range.

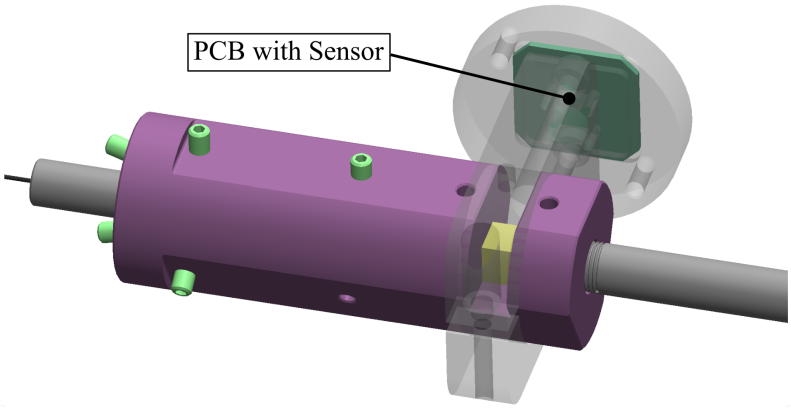

Figure 3.20: CAD model of the component for mounting the PCB containing the position sensor. The mounting mechanism allows the sensor to be adjusted relative to the beam splitter. Ensuring that the laser beam will hit the sensor area.

3.6 Developed Test Setup

The developed test setup can be explained using the block diagram in Figure 3.21. By applying strain and vibrations to the optomechanical system, the laser spot will change position on the sensor area. This will result in a change in the four photocurrents generated by the sensor. These four currents are converted to proportional voltages by the amplifier circuit on the PCB. The voltage signals are digitalised and sent to a computer using a data acquisition device. The four digital signals are imported into LabVIEW where they are used to calculate the position of the laser spot. The deflection of the pipe can also be calculated by knowing the ratio between the position of the laser spot and the deflection of the pipe.

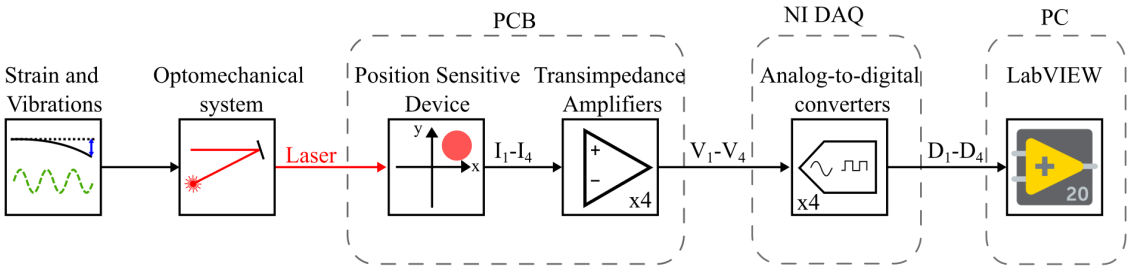

Figure 3.21: Block Diagram showing the functionality of the initial test setup. The sensor and the amplifier circuit are implemented on a PCB. The measurement signals from the TIA are sampled by a DAQ-unit and imported into LabVIEW.

Parts of the finalised test setup is depicted in Figure 3.22. The wires showing in this picture are the ones connected to the PCB. Four of the wires are for the sensor signals and two are for the supply voltage for the PCB.

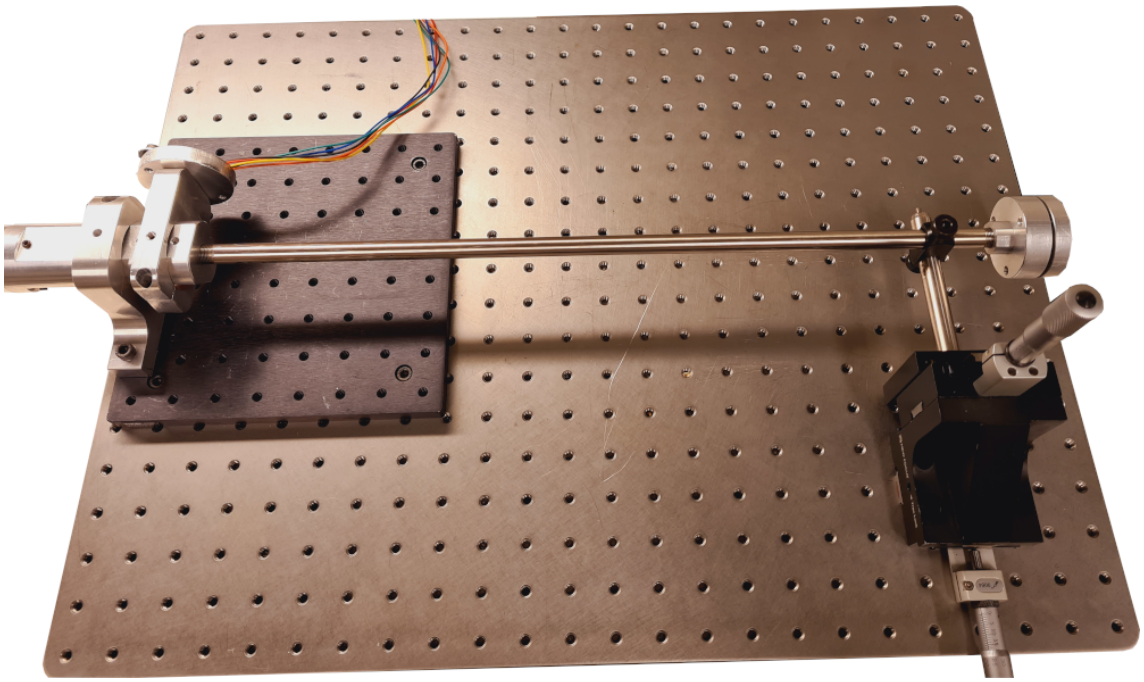

Figure 3.22: Developed test setup mounted on an optical breadboard. A displacement system is mounted at the free end of the pipe to deflect it in controlled increments.

Chapter 4

Initial Test Setup Performance

This chapter will present the different tests performed on the initial test setup. The different tests have been performed to analyse and state the system characteristics of the test setup. Section 4.1 will discuss the measurement range and the sensitivity of the system. Section 4.2 will discuss the resolution of the system which often is limited by the noise of the measurement signals. Section 4.3 discusses the test setup's ability to measure applied vibrations. Note that the measurements presented in Section 4.1 have been performed prior to starting the master's project. The master's project started by performing the noise measurements seen in Section 4.2.

4.1 System Sensitivity and Measurement Range

The system sensitivity of the test setup states the relationship between the applied pipe deflection and the measured laser beam position. The measurement range of the system states how large deflections of the pipe the sensor system can detect.

4.1.1 Test Method

Both system characteristics were found by applying known deflection values to the pipe. The exact same setup as the one depicted in Figure 3.22 was used to perform these measurements. Measurement data was captured by deflecting the pipe in increments of 100 µm or 200 µm and manually writing down the X and Y-position values calculated in LabVIEW. The deflection was measured one axis at a time. This means that while incrementing the deflection of the pipe in the X direction, the Y direction was unchanged. The measurement data could afterwards be used to plot a graph which displays the relationship between the applied deflection and measured laser beam position.

The sensitivity curve has also been captured in another system configuration, where the sensor is mounted on the free end of the pipe. This means that the laser is travelling through the pipe and hitting the sensor at the opposite end. This should make the measured displacement of the laser beam equal to the deflection of the pipe, meaning that the deflection-displacement ratio should be 1:1.

4.1.2 Results and Discussion

Figure 4.1 displays the measured sensitivity curve of the two configurations. These curves only represent the sensitivity of the system in one dimension. However, due to every component being square or circular and centered upon the sensor, the sensitivity curves for the two dimensions should be identical. The X-axis of this graph indicates how much the pipe is deflected, while the Y-axis indicates the measured position of the laser spot. As presented with Equation (3.1) and (3.2), the measured position of the laser beam is only a relative position ranging from -1 to 1. However, all relative positions in this thesis are multiplied with 1000, for better readability. This means that the relative position will be within -1000 to 1000.

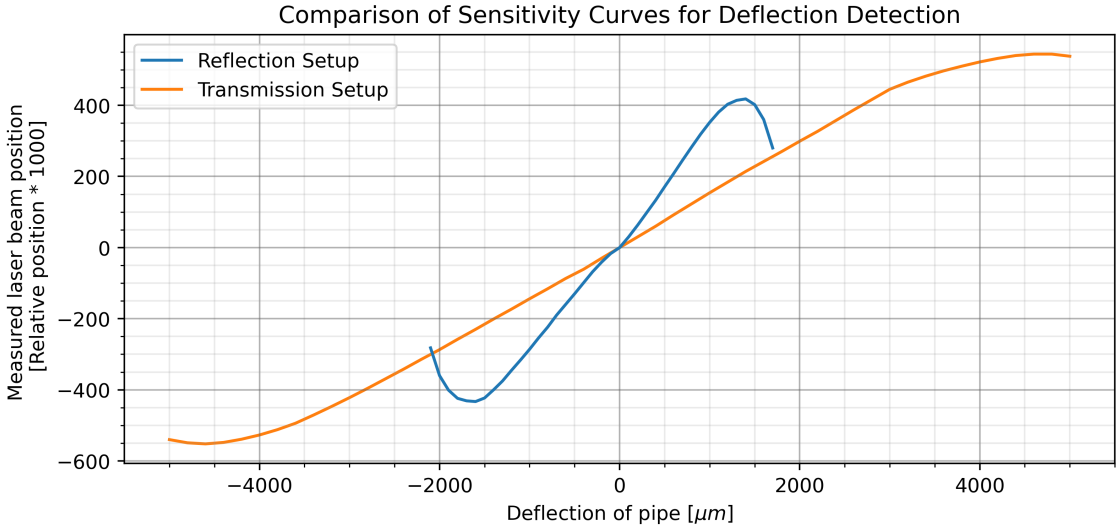

Figure 4.1: Comparison of sensitivity curves for the initial test setup. The graph displays the relationship between the pipe deflection and the measured position in two different configurations. In reflection setup, the sensor is mounted on the same side as the laser diode. In transmission setup the sensor is mounted on the opposite end of the laser diode.

The most important thing to notice from this comparison is the slope difference of the two curves. The slope of the reflection configuration is far greater than the transmission configuration. However, this is to be expected, as from the simulations it was observed that a 2 mm deflection of the pipe would result in a 6.12 mm laser spot displacement. This means that the displacement-deflection ratio is 3.06 (6.12 mm/2 mm). Meaning that theoretically, the slope of the reflection curve should be 3.06 times greater than the slope of the transmission curve. To further understand the graphs and to find the actual slope difference, each curve has been analysed individually.

Transmission Setup

Figure 4.2 shows the same sensitivity curve for the transmission setup as the one in Figure 4.1, but with added information. When performing these measurements, two additional aspects were also measured: When the laser spot intersected with the sensor edges, and when the laser spot started being blocked by some mechanical part. These aspects were measured by physically looking at the laser spot and should therefore be considered as very rough estimates.

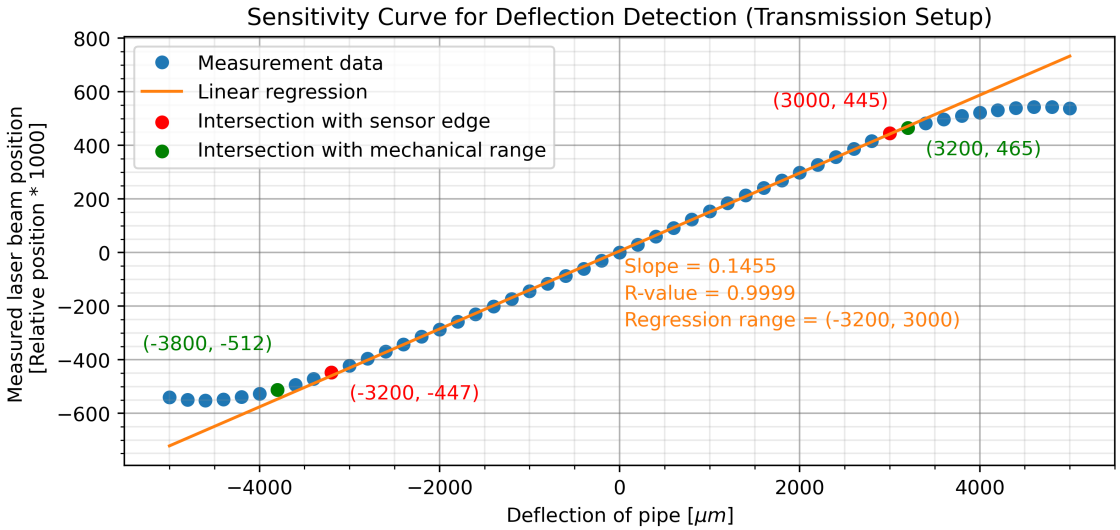

Figure 4.2: Sensitivity curve for deflection detection using the transmission setup. The graph displays the measured relative position of the laser beam for known deflection values of the pipe. A linear regression is applied to the measurement data where the laser spot is within the sensor area. This is to find the slope of the curve, which will correspond to the conversion ratio between relative position and the pipe deflection. For this configuration, the absolute laser beam position is approximately the same as the deflection applied to the pipe.

From the graph we can see that the laser spot intersected with the sensor edges at −3200 µm and 3000 µm. This is very close to what is expected. At the distance between the laser diode and the sensor, which is about 500 mm for this configuration, the laser spot diameter is estimated to be 2650 µm. When the laser spot is intersecting with the sensor edge, the center-of-mass for the laser spot will be 1325 µm (2650 µm/2) away from the sensor edge. The edges of the sensor will be at ±4500 µm due to the length of the sensor area being 9000 µm. This means that the measured position of the laser spot should theoretically be 3175 µm (4500 µm − 1325 µm).

At the outer sides of the deflection range, we can see that the measured position starts decreasing again. This is because the laser starts to move outside the sensor area, which changes the laser spots center-of-mass from the sensor's point of view. The measurement data outside the sensor edges can be used, but for simplicity and reliability, the measurement range for the test setup is defined to be within the sensor edges. From the measurement data within the sensor edges, we can see that the sensor outputs a very linear response. This is highly preferable as it makes the conversion from relative position to pipe deflection much easier. A linear regression can therefore be used to find the slope of the graph. This slope can then be used as the conversion ratio between the relative position and the pipe deflection. The linear regression in Figure 4.2 uses only the measurement data within two red points. The slope of the regression

line is 0.1455. This means that the measured relative position can be divided by 0.1445 to find an estimate of the pipe deflection. This conversion ratio should only be used between the relative positions of -447 and 445, for accurate position estimates.

Another thing to notice, is the point where the laser spot start being blocked by some mechanical aspect of the test setup. For the transmission configuration, this is the pipe. From the green points of the graph, we can see that this occurs at $-3800\,\mu m$ and $3200\,\mu m$. The fact that the green points are outside the red points is positive, as it means that the mechanical measurement range is not limiting the measurement range of the sensor in this axis. The mechanical limitation is also close to what is expected. The range where the laser spot is not blocked is $7000\,\mu m$ ($3800\,\mu m + 3200\,\mu m$). Adding the radius of the laser spot to each side, results in a range of $9650\,\mu m$ ($7000\,\mu m + 2 \cdot 1325\,\mu m$). This is close to the expected mechanical limitation of $10\,000\,\mu m$ (10 mm), which is the inner diameter of the pipe.

It is also worth noting the difference in the positions where the laser starts being blocked, $-3800\,\mu m$ versus $3200\,\mu m$. This is most likely due to the laser beam not being perfectly aligned, meaning that the laser beam does not go fully in parallel with the pipe when the pipe is undeflected. This results in the laser beam being blocked faster on one side versus the other.

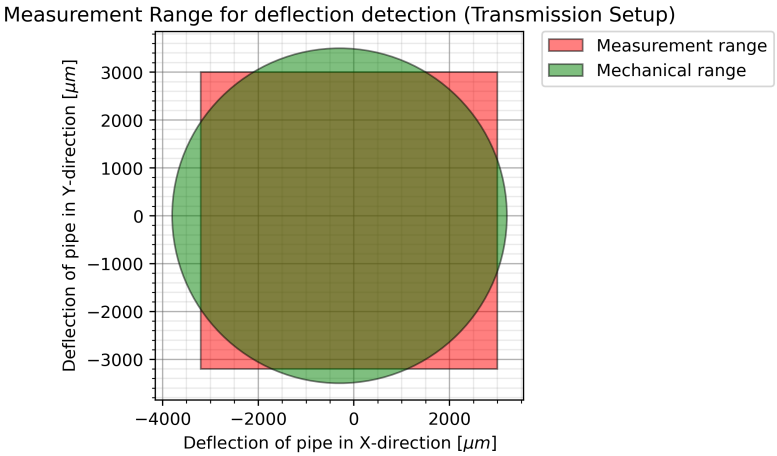

Figure 4.3: Comparison between the measurement range and the mechanical range for the transmission setup. The measurement range is defined as a square of $6200\,\mu m \cdot 6200\,\mu m$ and the mechanical range is defined as a circle with a diameter of $7000\,\mu m$. The measurement range displays how large pipe deflections the sensor can measure in X and Y-direction. The mechanical range will limit the usable measurement range. The usable measurement range for this configuration is the intersection between the two geometrical shapes.

Figure 4.3 displays the measurement range and mechanical range previously identified, as a two-dimensional plot. As previously mentioned, the X and Y-direction are assumed to be identical. The values previously identified were therefore used in both X and Y-direction. It was earlier stated that the mechanical range was not limiting the measurement range. However, when plotting the values in the two-dimensional plot, we can see that this is not the case. Due to the mechanical limitation being the pipe, the mechanical range is plotted as a circle with a diameter of $7000\,\mu m$. This means that the corners of the measurement range can not be utilised as the laser will be blocked by the pipe. The measurement range that can be used for this specific configuration, is therefore the intersection between the two figures in the plot.

Reflection Setup

Figure 4.4 is presenting a closer look at the sensitivity curve for the reflection configuration. For this measurement, the deflection of the pipe has been incremented with steps of 100 µm, versus the 200 µm increment steps used for the transmission measurement. From the curve can we see a very noticeable shift around the origin of the graph. This is to be expected due to the way these measurements have been performed. The laser spot is positioned on the origin of the sensor area before the pipe deflection is incremented in the positive direction. Afterwards the laser spot is once again positioned in the origin and the pipe is deflected in the negative direction. This has been seen to produce a DC-shift around the origin of the curve. However, this curve does not only have a DC-shift, it also has a change in the slope. The cause of this error is not quite clear, but it is most likely a problem with the displacement system and not the sensor system. The displacement system operates by pushing the pipe in one direction, while pulling the pipe in the opposite direction. Due to the stiffness of the pipe, the displacement system does have problems pulling the pipe to the desired displacement value. This is considered the most likely cause of this phenomenon. The regression was therefore only applied to the positive side of the graph, where the pipe was pushed and not pulled. The regression was applied on the measurement data from 0 to 1000 µm and resulted in a slope of 0.3588. It is worth noting that this ratio can only be used to find the deflection of the pipe, based on the relative position of the laser spot. The absolute position of the laser spot can not be identified directly from this ratio.

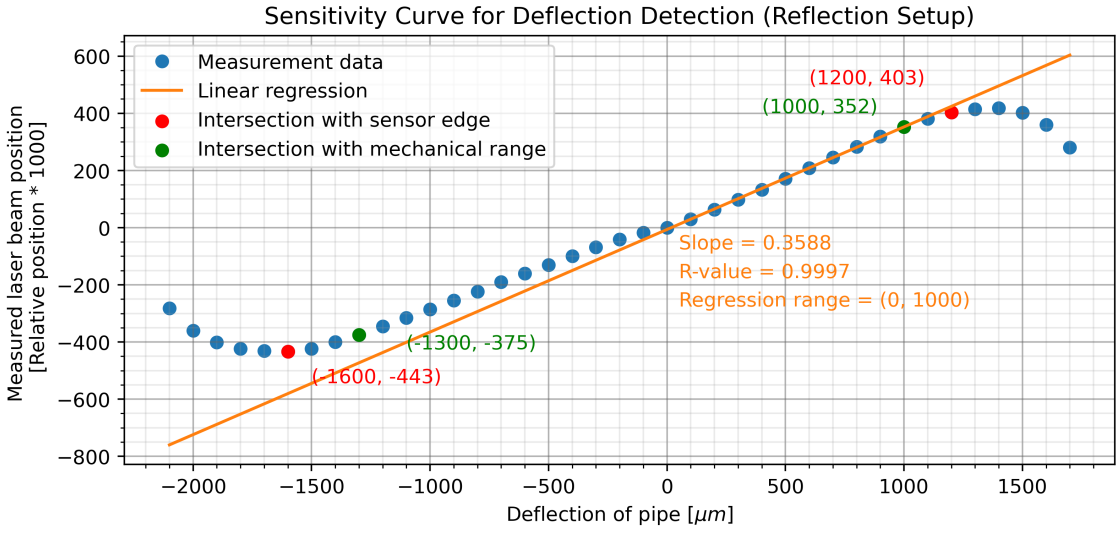

Figure 4.4: Sensitivity curve for deflection detection using the reflection setup. The graph displays the measured position of the laser beam for known deflection values of the pipe. As only the positive side of the graph is considered viable, the linear regression is applied from 0 to 1000 µm. Resulting in a slope of 0.3588.

A difference of this curve, versus the transmission sensitivity, is that the laser spot starts getting blocked by the mechanical system before the laser spot intersects with sensor edges. The result is the laser spot never intersecting with the sensor edges. This is a result of a poorly dimensioned mechanical system, as discussed in Section 3.5.

The red points in this graph, is an estimation of when the laser spot would intersect with the sensor edges. As this was not possible to see, because the laser never reached the sensor edges, this is a very rough estimate. As previously mentioned, the positive part of the graph is considered to be the most accurate representation of the system. In order to check if the intersection point is somewhat correct, some calculations were performed. These calculations are based on the measurement results from the transmission setup, which was considered to be fairly accurate. With the transmission setup it was stated that the laser spot would intersect with the sensor edge at 3175 µm pipe deflection, which would relate to a relative laser spot position of 462. Inserting this relative position into the regression function found for the reflection setup, shows that the reflection setup would measure the same relative position at 1287.5 µm pipe deflection. This is not far away from the measured pipe deflection of 1200 µm.

The expected position where the laser would start getting blocked has also been calculated. Based on the limiting mechanical diameter of 8000 µm (8 mm), the laser can be displaced 2675 µm (4000 µm - the laser radius of 1325 µm), in one direction before being blocked. In order to convert this displacement to a deflection of the pipe, it can be multiplied with the ratio between the slope of the transmission curve and the slope of the reflection curve. This ratio is identified to be 0.4055 (0.1455/0.3588), which results in a deflection value of 1084.7 µm (2675 µm · 0.4055). This is close to the measured point of 1000 µm in Figure 4.4.

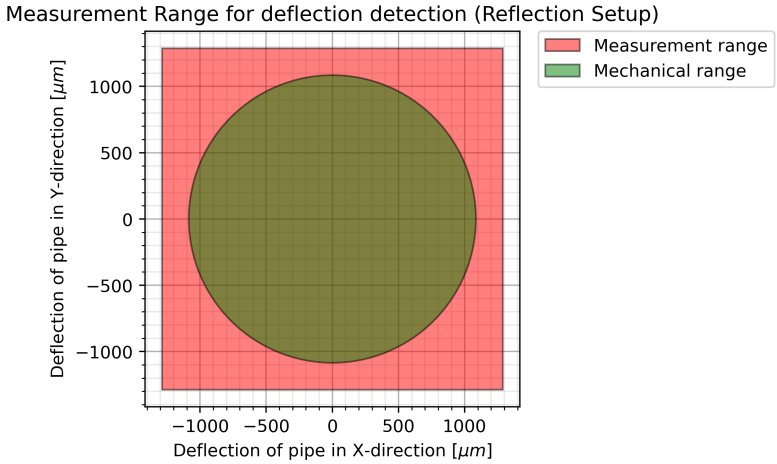

Figure 4.5: Comparison between the measurement range and the mechanical range for the reflection setup. The values used for this figure are the calculated ones, which are fairly close to the measured values. The measurement range has been found to be 2575 µm·2575 µm, while the mechanical range has been found to be circular with a diameter of 2169.4 µm. The usable measurement range for this configuration will be limited to the mechanical range.

The calculated measurement range and mechanical range have been used to visualise the measurement range for the reflection setup in Figure 4.5. The measurement range is displayed as a square of 2575 µm · 2575 µm and the mechanical range is displayed as a circle with a diameter of 2169.4 µm. For this test setup configuration, the usable measurement is limited to the mechanical range. However, if the mechanical components are better dimensioned, the potential measurement range will equal the square of 2575 µm · 2575 µm.

Simulation Results vs. Measurement Results

As mentioned in the start of Section 4.1.2, the simulation results did present a deflection-displacement ratio for the reflection setup of 3.06. This means that laser would be displaced 3.06 µm for every micro meter the pipe would be deflected. However, the deflection-displacement ratio from the measurements, were found to be 2.47 (0.3588/0.1455). This means that there is a difference between the simulation and the actual results. As the results from the transmission configuration were very close to what was expected, this indicates that the applied deflection to the pipe is correct. However, this does not mean that the angle of the mirror is correct, as the pipe might not bend with the same curvature as expected. This results in a different end-slope and mirror angle from what is simulated. There are multiple reasons why the pipe might not bend as expected. One being how the fixed end of the pipe is mounted. Due to the pipe being mounted with screw threads, this does allow for a little wobble of the pipe. Meaning that the pipe is not mounted firmly enough. This will therefore alter how the pipe will be bent.

Another reason might be because of how the deflections are applied to the pipe. From Figure 3.22 can we see that the displacement system is not mounted at the very end of the pipe. In addition, the displacement system is holding the pipe in place and not just pushing the pipe with a single point force, as depicted in Figure 3.6. Both of these differences might alter the angle of the mirror and therefore be the cause of the difference between the simulated and measured deflection-displacement ratio.

4.2 Deflection Resolution and System Noise

This section will present and discuss the resolution of the test system. The resolution of a sensor can be defined as the smallest detectable incremental change of an input parameter that can be detected in the output signal [8]. For this sensor system, the resolution will be defined as the smallest incremental change of pipe deflection the system can measure. This is usually limited by one of two factors. One being the resolution of the ADC, which will decide the number of different steps the analogue signal can be converted into. An insufficient number of steps will result in large incremental steps, which will limit the system's ability to distinguish between two incrementally small analogue values.

The other factor is noise on the measurement signals. Unpredictable noise on the measurement signals might make it hard to distinguish between two incremental values. The signals might be covered by noise much larger than the actual change. For that reason, both the resolution of the ADC and the noise of the measurement signals are analysed in this section in order to identify the resolution of the initial test setup.

4.2.1 Test Method

Every measurement presented in Section 4.2 is static measurements using the same test setup as the one presented in Section 3.6. This means that the displacement system has been used to apply a constant deflection value to the pipe, while capturing the measurement signals. As previously mentioned, the four voltage signals from the four channels of the sensor is captured by a DAQ device. Further in this thesis the four voltage signals from the sensor will be referred to as measurement signals, while the calculated X and Y values will be referred to as position signals or position values. The measurement signals are imported and processed in real-time using a LabVIEW program. For this test configuration LabVIEW has three main objectives. Firstly, to use the four measurement signals to calculate the relative position values X and Y, using Equation (3.1) and (3.2). Secondly, both the four measurement signals, and the two position signals, are plotted in real-time for the user. Thirdly, all six signals are saved to a text file for further processing and analysis.

Various scripts in MATLAB have been used to analyse the noise measurements saved by LabVIEW. An important reason for saving both the position values and the measurement signals, is that it allows for a comparison between all the signals. This has been very useful for understanding how noise on the measurement signals will affect the position signals. It is worth noting that the position signals saved by LabVIEW is the measured relative position. The MATLAB scripts used are therefore dividing the relative position signals with the conversion ratio for the reflection setup, in order to find an estimate of the pipe deflection. This conversation ratio was previously found to be 0.3588, as seen in Figure 4.4. A reason for performing this conversion in MATLAB and not LabVIEW, is that it allows for easy adjustments of the conversion ratio, should the previous conversion ratio turn out to be incorrect.

Most of the noise measurements captured have been analysed both in the time domain and the frequency domain. For the time domain most measurements are captured and analysed over a period of 10 seconds. This is in most cases enough time to give a good representation of the noise on the measurement signals. If not otherwise is stated, the sampling frequency of the DAQ device is 1 kHz.

4.2.2 Method for Defining the Amount of Electrical Noise

A method for defining the amount of noise in measurement signals is required in order to compare the different noise signals. One way of defining the amount of noise in a measurement signal is to calculate the Standard Deviation (SD) of the signal. The Standard Deviation is a measure of the amount of variation or dispersion of a set of values [9]. This can thereby be used to measure how much the noise on the measurement signal disperse from the mean value of the signal. For this method to work properly, the DC-value of the measurement signal must stay relatively constant, meaning that the signal must have no significant drift. This way the measured variations on the measurement signal will only be caused by electrical noise.

In order to determine if the noise on measurement signal will limit the measurement resolution, the noise resolution must be identified. The noise resolution is defined, for this thesis, as the smallest change in a measurement signal one can with certainty detect. This means that the change measured was caused by a change on the sensor side and not just electrical noise.

One way of identifying the noise resolution, is to find the Peak-To-Peak (PTP) value for the measurement signal over a given period of time. Peak-To-Peak defines the difference between the highest and lowest value of a set of values. A problem with this method is that the PTP-value might not be a good representation of the overall noise, as a single noise spike on the measurement signal might decide the PTP-value. A better way to define the noise resolution is to use the SD-value to calculate an estimate of the PTP-value. From [10] it is suggested that a good estimate of the PTP for a noise signal will be six times the SD-value. This is predicated on the noise being perfectly normal distributed, which in reality is rarely the case.

4.2.3 Noise Measurements

Figure 4.6 presents one of the first noise measurements captured by the test setup. For this measurement the laser spot was centred to the middle of the sensor area, which is defined as $X = Y = 0$. The power supply used initially was a simple one from Biltema, which was adjusted to 5V. Figure 4.6 contains six graphs. The two first graphs display the calculated pipe deflection in the X and Y-axis. The deflection is displayed in micro meter (µm). Note that these signals are found from calculating the relative position values and dividing them by the sensitivity slope, as previously discussed. The four remaining graphs display the four measurement signals from the sensor, measured by the DAQ-unit. As previously discussed, these are used to calculate the relative position values and therefore also the pipe deflection values. The measurement signals are displayed in millivolts (mV).

All signals are captured and calculated simultaneously, meaning that there is no time delay between the 6 graphs. A given time value in one of the graphs corresponds to the same time value in all the other graphs. The measurement display 10 seconds of the measurement signals. Both the mean value, and the estimated PTP-value, are calculated for each signal. The mean value is displayed as a white line, while the PTP-value is the difference between the two red lines. The PTP-value is centered around the mean value as it indicates how much the signal disperse from the mean value.

As the DC-value of the four measurement signals in Figure 4.6 are approximately equal, the two deflection signals are close to zero. This is due to the way the deflection values are calculated. One very noticeable aspect of this noise measurement is the spikes on the four measurement signals. These spikes have been proven to be caused by the power supply used and will therefore not be the main focus of this analysis. However, the spikes allowed for other aspects of the system to be better displayed. One of them being how the noise on the measurement signals affects the displacement signals. Looking at two upper graphs, we can see that the noise spikes are not apparent on the displacement signals. This is due to the noise spikes acting as common noise on the four measurement channels. Due to the way the displacement signals are calculated, common noise on the four measurement channels will be eliminated.

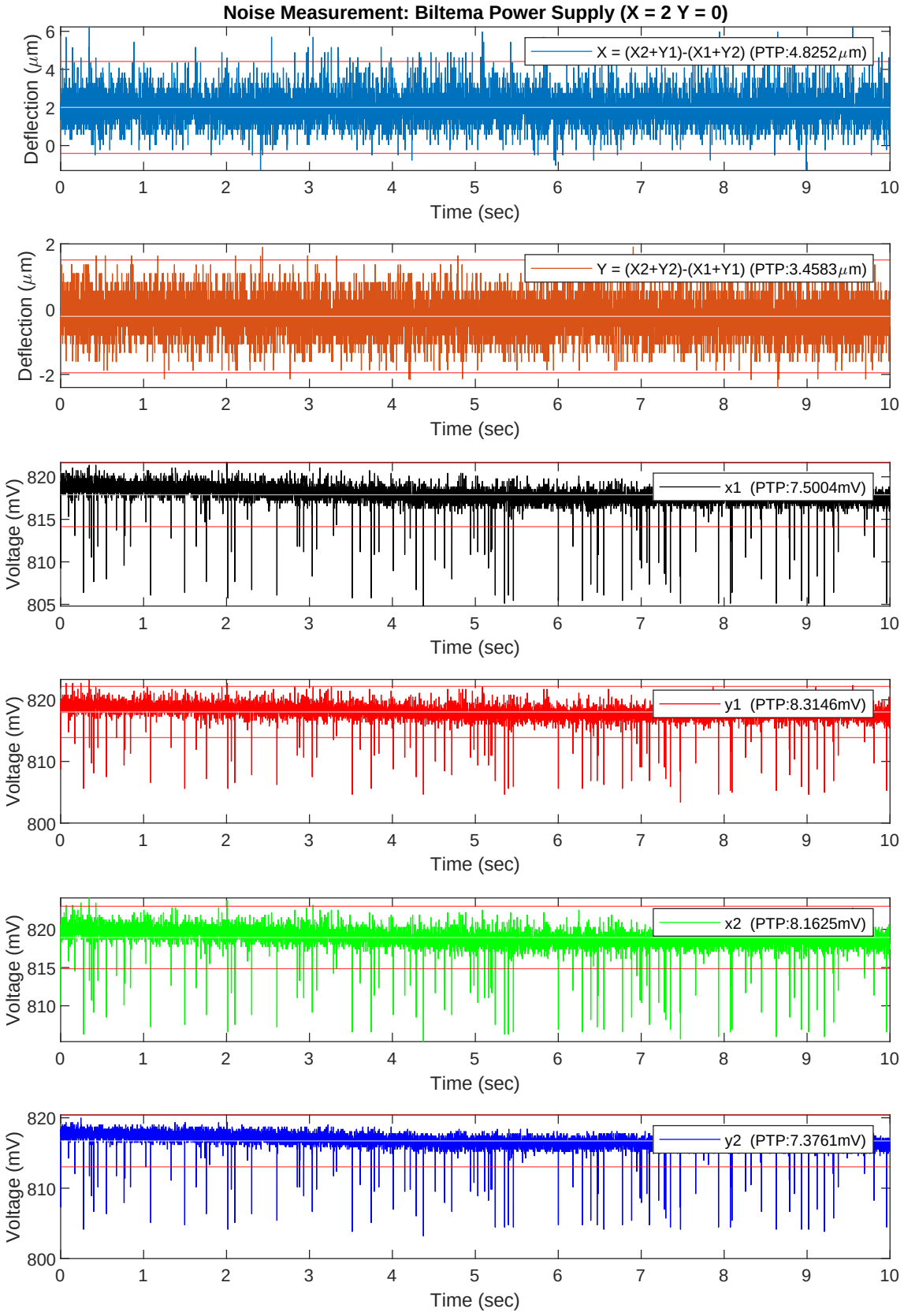

Figure 4.6: Noise measurement: Biltema Power Supply (X=0 Y=0). The figure displays six signals: The two calculated deflection values of the pipe and the four measurement signals used to calculate it. Due to the way the X and Y-deflection values are calculated, most of the common mode noise from the four measurement signals are eliminated on the deflection signals. The noticeable spikes on the measurement signals have been proven to be a result of the power supply used.

Impact of Laser Spot Position

Upon analysing different noise measurements, it became apparent that the cancellation of common mode noise did not work as well when the position of the laser spot was moved away from the centre of the sensor area. Figure 4.7 displays the two deflection signals from a noise measurement where the laser spot was placed somewhere between the centre of sensor, and the sensor edge corresponding to the negative X direction. From this measurement we can see that the noise spikes are now also apparent on one of the deflection signals. This being the X-direction which is the same axis as the laser spot was moved. Note that the four measurement signals are still very similar to the ones presented in Figure 4.6. The complete measurement including all six measurement signals, is presented in Appendix F.2.

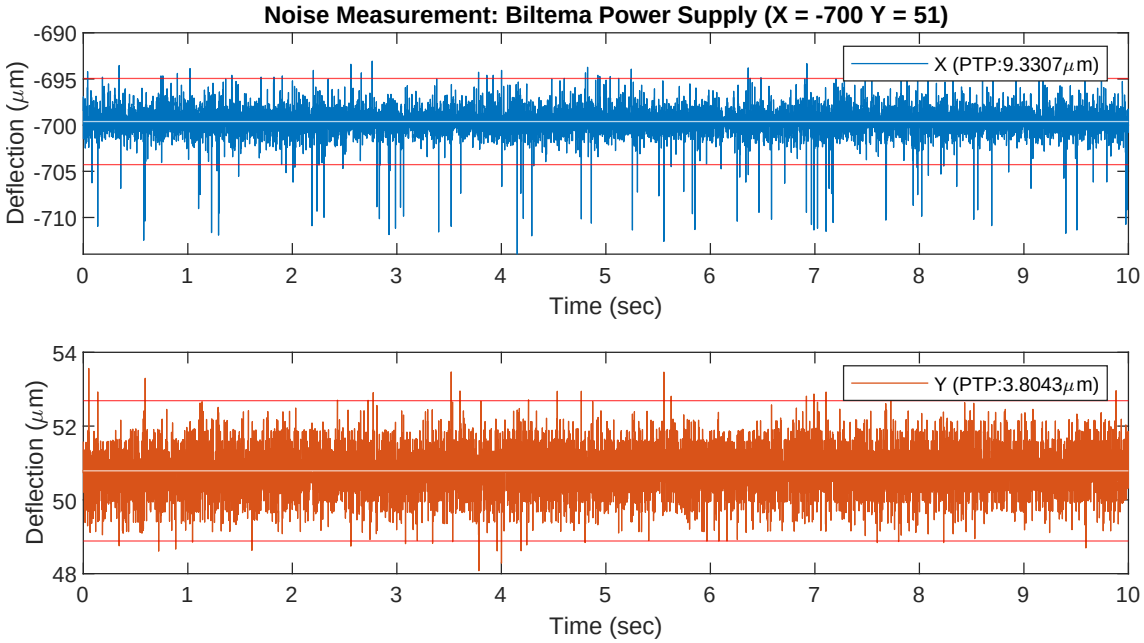

Figure 4.7: Noise measurement: Biltema Power Supply (X=-700 Y=51). As the deflection value in one axis gets farther away from zero, the noise spikes on this channel will get more noticeable. This is due to the noise on a measurement channel getting marginally larger when the laser spot gets closer to it. The differences in the amplitudes of the noise spikes get very noticeable on the calculated deflection values.

Other noise measurements with different laser spot positions have also been performed. From all the performed measurements, it was clear that the noise spikes on the displacement signals got larger the farther away the laser spot got from the centre of the sensor area. However, it affects the two measurement axes individually. This means that a laser spot with a high X-position and a close to zero Y-position, will only generate major noise spikes on the X-deflection signal, and vice versa. A laser spot position with high X and Y-position will generate noise spikes on both channels.

Upon closer inspection of each of the four measurement signals, the reason for this phenomenon was revealed. Figure 2.5 depicts the four channels of the sensor. As the laser spot gets closer to one of the channels, the noise spikes will get marginally larger on that same channel. As the X and Y-deflection values are calculated from the differences in the four measurement signals, these small differences will be very apparent on the deflection signals.

Impact of Power Supply

Several different measurements were performed expecting to identify the source of the major noise spikes seen on the previous measurements. After replacing the power supply used to power the PCB with the sensor interface, it was clear that this was the issue. Noise from the supply voltage got directly coupled to the measurement signals. This has to do with the way the transimpedance amplifier is configured and how the voltage reference for the amplifier is generated. From Figure 3.14b and Equation (2.4) we can see that the voltage reference, V_{ref}, will get directly coupled to the output voltage, V_{out}. This means that noise on the voltage reference will be directly added to the output signal. As displayed by the circuit diagram in Figure 3.15, the voltage reference is generated from a simple voltage divider. This allows noise from the supply voltage to be coupled directly to the voltage reference. This configuration will therefore make the measurement signals very susceptible to noise from the supply voltage.

Figure 4.8 displays a noise measurement performed with a lab power supply instead of the Biltema power supply previously used. For this measurement, the laser spot is placed roughly in the middle of the sensor area. The measurement clearly displays a different noise pattern on the four measurements signals, compared to the previous measurements. While the large noise spike is not present anymore, the common mode noise is still very noticeable. At first glance, it might seem like the four measurement signals have about the same amount of noise. However, by comparing the PTP-values, it is clear that noise amplitude of the four channels is different. The noise of channel y1 and x2 is more than twice as large as channel y2. Upon comparing the noise levels on the different channels, for all the measurements performed, a slight trend was observed. The comparison revealed that y1 and x2 in general would have slightly more noise than the two other channels. The exact reason for this is unclear. However, it is most likely a physical difference. It can be a difference in the connection quality of the wires used to connect the DAQ-unit to the measurement signals from the PCB. Another possibility is a difference in the way the four measurement signals are routed on the PCB.

Due to the difference in noise levels of the four channels, the same problem will occur as the one presented in Figure 4.7. The rejection of common mode noise is not working well because of the differences in noise levels. The common mode noise will therefore be coupled to the displacement signals.

4.2.4 ADC Resolution

The DAQ-unit used to sample the measurement signals contains four synchronous 16-bit ADCs. The ADCs are hardware configured to measure voltages from −10 V to 10 V. The ADC voltage resolution, Q, can be found by the following equation.

$$Q = \frac{E_{FSR}}{2^n} = \frac{+-10V}{2^{16}} = \frac{20V}{2^{16}} = 0.3052mV \tag{4.1}$$

Where E_{FSR} is the ADCs full scale voltage range and n is the ADCs resolution in number of bits. The ADCs voltage resolution is calculated to be 0.3052 mV. Upon analysing the measurement signals in MATLAB, the smallest change in the signals was observed to be 0.3190 mV, which is not far away from the calculated resolution.

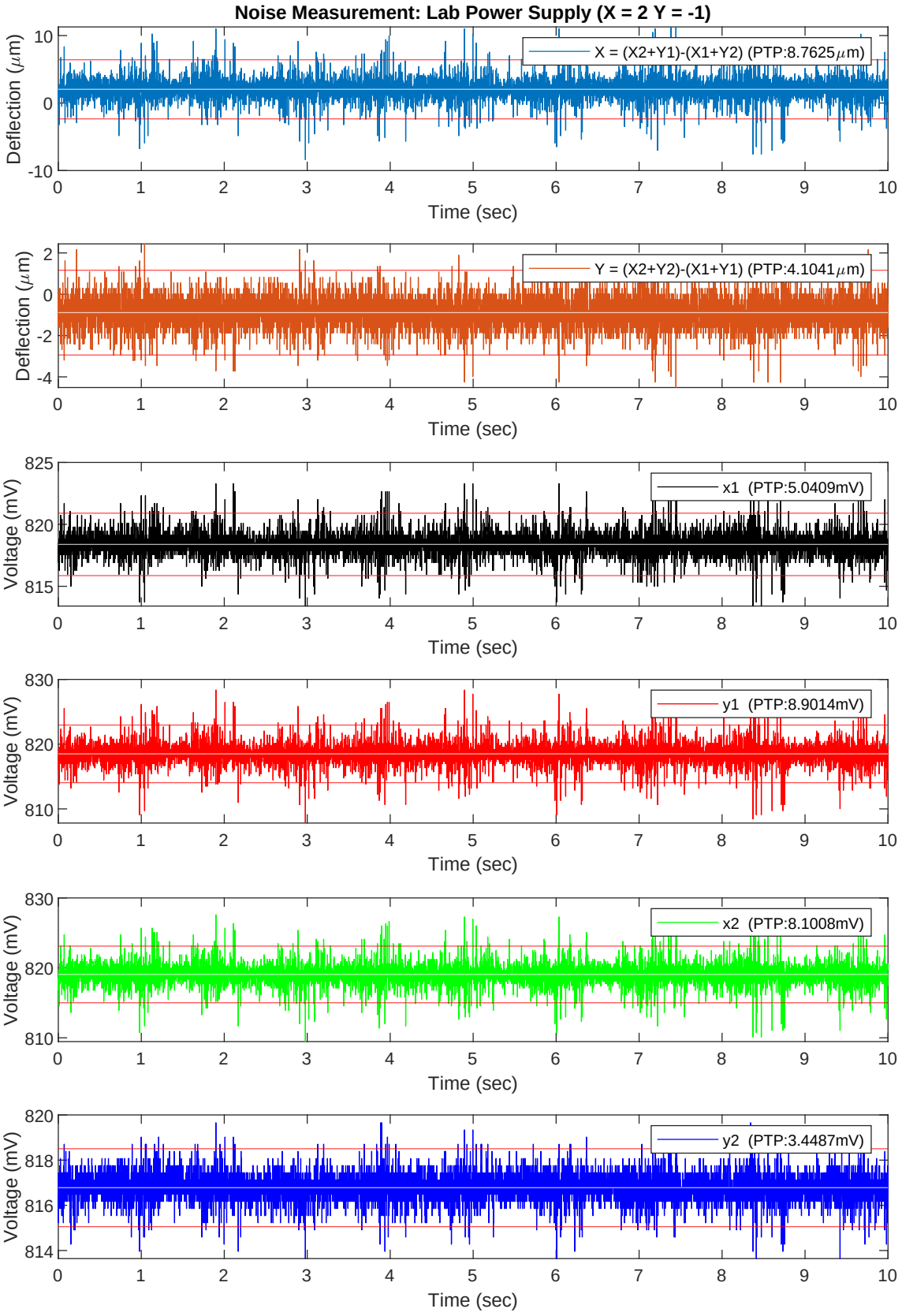

Figure 4.8: Noise measurement: Lab Power Supply (X=2 Y=-1). The measurement signal is significantly affected by noise from the supply voltage. This is due to the transimpedance amplifier configuration, and how the voltage reference for the amplifier is generated. Differences in noise levels for the four measurement channels weaken the system's ability to eliminate common mode noise. The common mode noise is therefore very noticeable on deflection signals too.

4.2.5 System Resolution

From the noise measurements presented, it is clear that the electrical noise is limiting the system resolution, and not the ADC resolution. This can be seen by the fairly detailed noise signals. From the noise measurements previously presented, we have seen that the amount of noise will vary depending on the position of the laser spot and the type of voltage supply used. An overview of the noise levels for the two power supplies has therefore been created and is presented in Table 4.1.

	Deflection (µm)			Voltage (mV)		
Power Supply	Min	Avg.	Max	Min	Avg.	Max
Biltema PSU	3.48	5.87	9.33	6.18	7.69	9.16
Lab PSU	4.12	7.15	8.76	3.35	6.19	8.90

Table 4.1: Comparison of PTP noise levels for the two different power supplies. The table displays the minimum, maximum and average noise levels of both the deflection signals and measurement signals. The data is gathered from multiple measurements with different laser spot positions.

For both power supplies, multiple noise measurements have been performed with different laser spot positions. The minimum, maximum and average noise levels have been identified using all the measurements. For example, this means that the average voltage value of the Biltema power supply have been calculated using the four measurement signals for all the different noise measurements. All noise levels in this comparison, is the estimated PTP value. As seen from the previous measurements, the accuracy of this estimation will heavily depend on the noise pattern. The estimation will be a better fit for compact noise signals, versus signals with large noise spikes, as seen in Figure 4.6.

The comparison reveals that the average noise levels on the measurement signals is 7.69 mV for the Biltema power supply and 6.19 mV for the lab power supply, which leads to the average noise levels on the deflection signals to be 5.87 µm for the Biltema power supply and 7.15 µm for the lab power supply. As the resolution is limited to the noise levels, the system resolution for the two configurations can be stated as 5.87 µm and 7.15 µm, respectively. This is on average six and a half times worse than the deflection resolution requirement set in Section 1.3.1 of 1 µm.

4.3 Vibration Detection

This section will present and discuss the test setup's ability to detect vibrations applied to the free end of the pipe. It will be important to see from the measurements if the correct vibration amplitude and frequency can be detected by the system.

4.3.1 Test Method

To apply vibrations to the free end of the pipe, an industrial vibration machine was used. This machine can apply known vibration to the system. The vibration frequency can be kept constant or set to sweep over a range of frequencies. In addition, the PTP amplitude of the vibrations can be adjusted. Figure 4.9 depicts the setup used for the vibration measurements of the initial test setup.

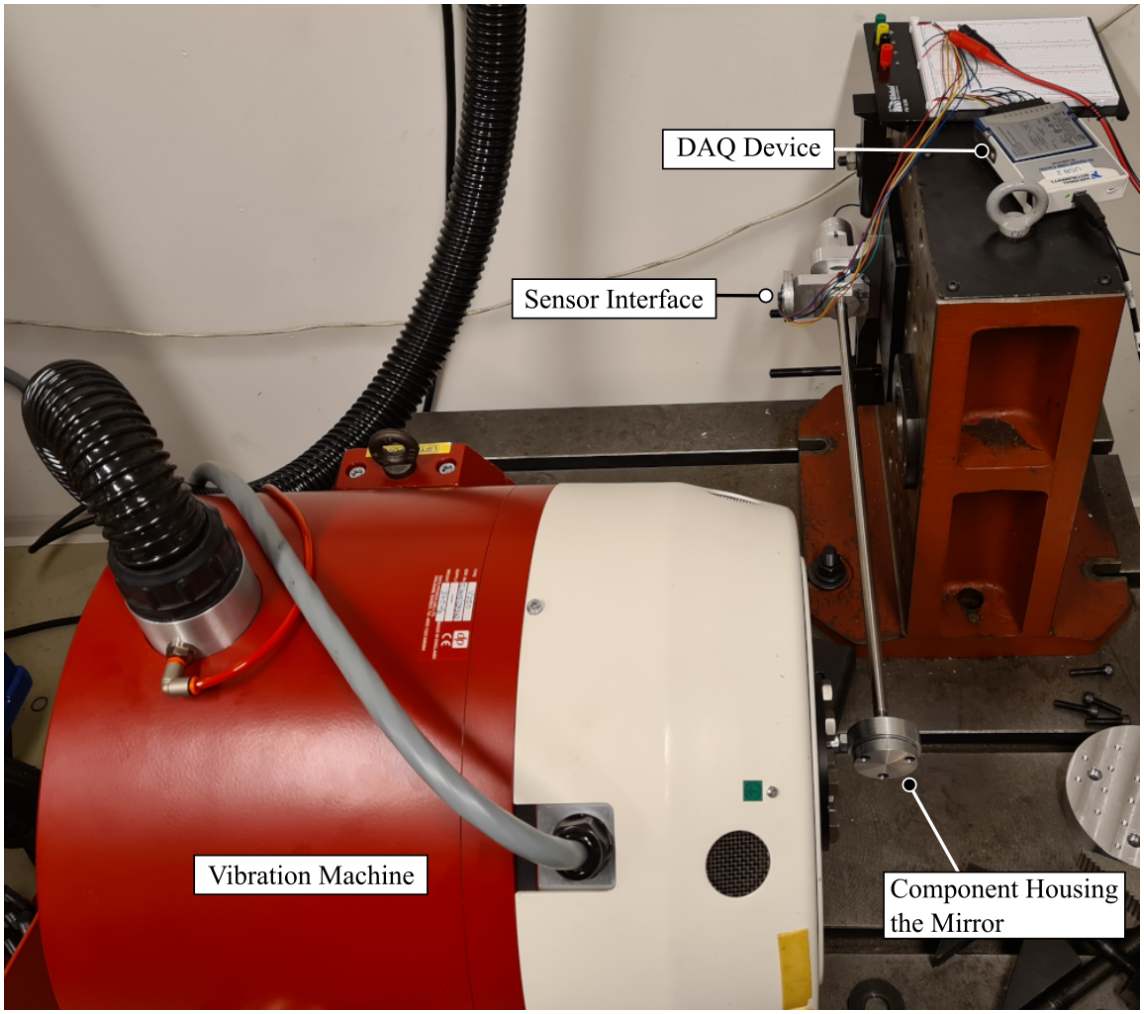

Figure 4.9: Setup used for the vibration measurements of the initial test setup. The fixed end of the test setup is mounted to a large metal block, while the free end is mounted firmly to the vibration machine. This will force the free end of the pipe to follow the movement of the vibration machine, while the fixed end should be still.

From Figure 4.9 we can see that the fixed end of the test setup is mounted to a large metal block. This was achieved by mounting the test setup to a mechanical breadboard plate which was mounted to the large metal block. This is better depicted in Figure 4.10a. The free end of the pipe is now mounted to the vibration machine. This was achieved by using a mechanical component which was clamped around the component housing the mirror. This is better depicted in Figure 4.10b. The clamping component is fixed firmly to the part of the vibration machine, which move when vibrations are applied. This means that the free end of the pipe is firmly mounted to the vibration machine and should therefore follow the exact movement of the vibration machine.

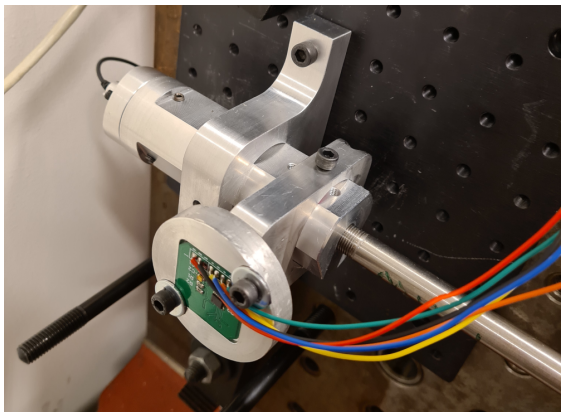

(a) The fixed end of the test setup is mounted to a mechanical breadboard which is mounted to the large metal block. All parts of this mounting solution are fixed very firmly, making this part of the test setup very resistant to external movement.

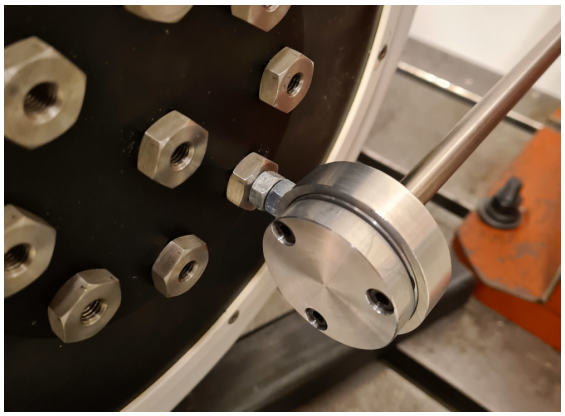

(b) The free end of the test setup is mounted to the vibration machine with the use of a mechanical component clamping over the component housing the mirror. This forces the free end to follow the exact movement of the vibration machine.

Figure 4.10: Mounting solutions for the vibration test setup.

For the vibration measurements, the sampling frequency of the DAQ-unit was set to 6.4 kHz. The sampling frequency was set to be about ten times higher than the highest applied vibration frequency, which was 500 Hz. This is to ensure that there is close to no reduction in the amplitude of the sampled signal, at the highest frequencies. The signals were captured and saved in LabVIEW, in the same way the noise measurements was.

4.3.2 Vibration Measurements

Various vibration measurements with different frequencies and amplitudes have been performed to the initial setup. Figure 4.11 displays a section of a measurement where vibrations at 30 Hz with a PTP amplitude of 100 µm were applied. The upper graph displays 1 second of the measured Y displacement signal, which was the direction the vibration was applied. The graph displays a visible sinusoidal pattern repeating 30 times per second, which equals 30 Hz. Noise on the deflection signals makes the measured sinusoidal pattern not as clean as the one applied. The PTP amplitude of the measured signal is about 18 µm. This is about five times lower than the applied amplitude of 100 µm. The full vibration measurement can be seen in Appendix G.1.

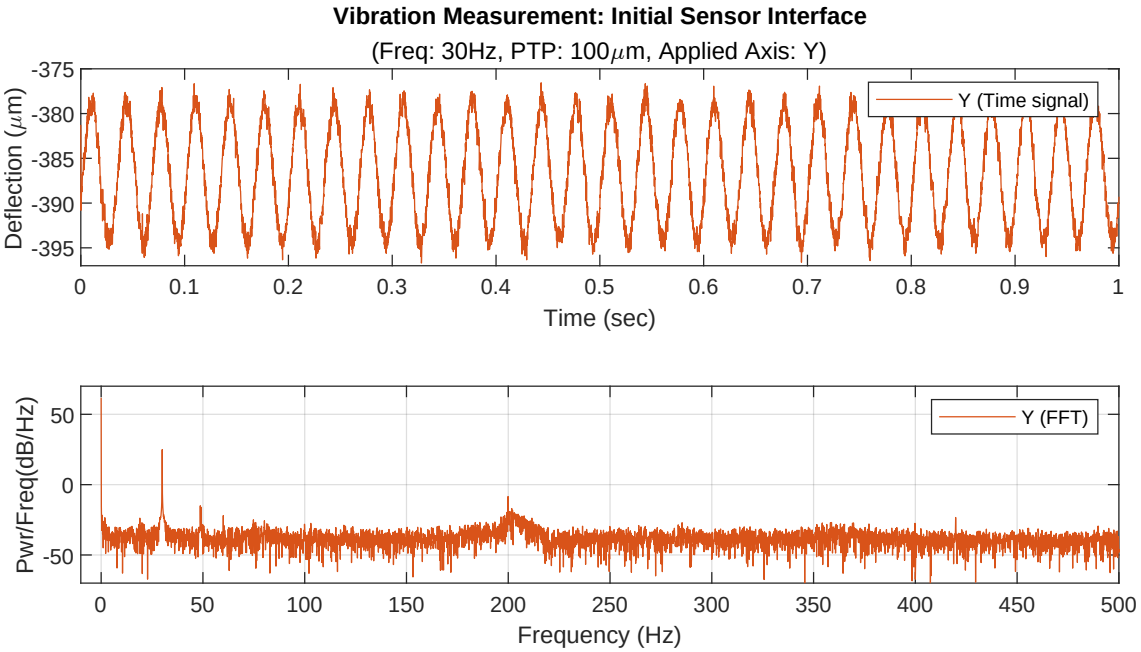

Figure 4.11: Vibration measurement on the initial test setup. The applied vibration frequency of 30 Hz can easily be recognised in both the time and frequency domain of the measured deflection signal. The measured PTP amplitude of 18 µm is about five times smaller than the applied amplitude of 100 µm.

For each vibration measurement a Fast Fourier Transform (FFT) analysis has been performed. A FFT analysis is useful for finding which frequency components the signal consists of. The lower graph of Figure 4.11 depicts the FFT of the time signal in the upper graph. The FFT displays two major spikes at 0 Hz and 30 Hz. The 0 Hz spike indicates that the time signal has a major DC-level, while the 30 Hz spike indicates that the majority of the signal consists of a 30 Hz sinusoidal pattern. The whole FFT analysis can be seen in Appendix G.2.

While applying vibrations at different frequencies and amplitudes, some aspects of the system got apparent. The system has no problem detecting the applied vibration frequency. However, the measured amplitude does not match the one applied. Measurements with different amplitudes, but same frequency, show that the amplitude changes fairly proportionally. This means that if an applied amplitude of 100 µm corresponds to a measured amplitude of 18 µm, will an applied amplitude of 200 µm correspond to a measured amplitude of 36 µm. However, this ratio is found to vary with the vibration frequency. To further investigate this phenomenon a linear vibration frequency sweep was applied to the system. Figure 4.12 presents the result of a linear frequency sweep from 20 Hz to 200 Hz over 60 seconds, with a constant amplitude of 20 µm.

The upper graph of Figure 4.12 displays the measured vibrations over the 60 seconds that the sweep was applied. The measured signal displays changes in amplitude as the frequency changes. This is despite the applied amplitude being constant. The measured amplitude varies from about 5 µm to 400 µm, despite the applied amplitude of 20 µm. The middle graph displays the same signal, but with a zoomed-in vertical axis. This reveals that the amplitude gets larger for certain frequencies. The lower graph displays the FFT of the signal and is aligned so the frequency axis corresponds fairly well with the frequency applied at the corresponding time stamps above.

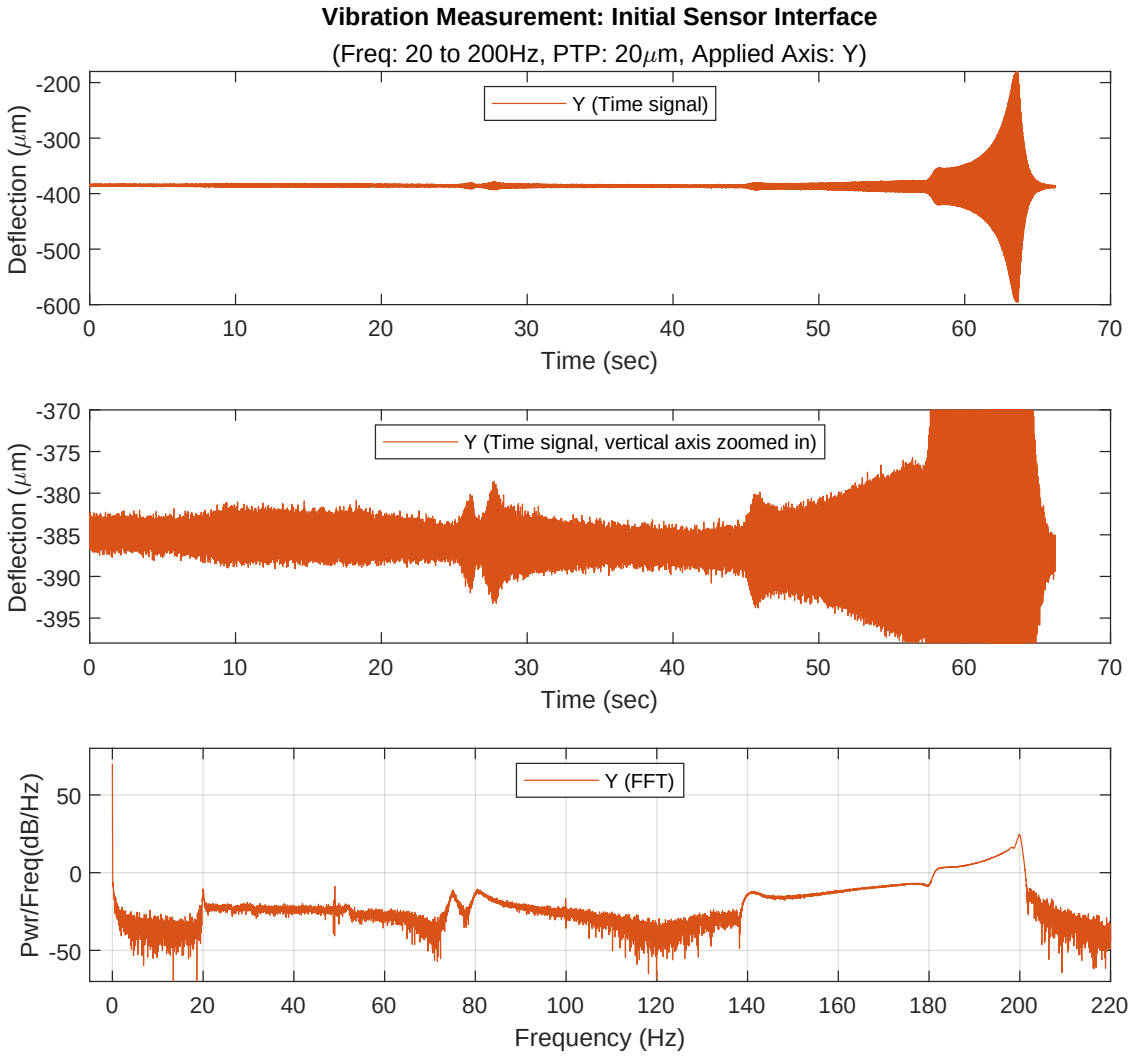

Figure 4.12: Vibration sweep of the initial test setup. A linear vibration sweep from 20 Hz to 200 Hz is applied to the system over 60 seconds. Despite the applied amplitude being constant at 20 µm, is not the measured amplitude constant. The measured amplitude varies between 5 µm to 400 µm. The graphs display the measured time signal and the corresponding FFT analysis. Due to the frequency sweep being linear, the frequency axis is aligned so it corresponds fairly well with the frequency applied at the corresponding time stamps above. From a linear frequency sweep is a flat frequency spectrum from 20 Hz to 200 Hz expected. However, this is not the case for this measurement. The largest spike in amplitude occurs when the applied frequency is around 200 Hz.

Due to this being a linear frequency sweep, the expected FFT result would be a flat frequency spectrum from 20 Hz to 200 Hz. However, this is not the case, as the power per frequency within the range 20 Hz to 200 Hz fluctuates about 75 dB. This frequency response is very undesirable as it makes it difficult to measure the correct amplitude. The reason for this phenomenon is unclear, but it is most likely a mechanical issue. From the graph we can see that the amplitude got 20 times higher than the expected amplitude around 200 Hz. When performing the measurement, these large vibration amplitudes could be felt by touching the vibrating pipe. This means that the system actually vibrates at such high amplitudes and not just the sensor interface amplifying the signals somehow. A possible explanation to this phenomenon is that the applied frequency of 200 Hz equals a resonant frequency of the pipe used in the mechanical setup. When applying a resonant frequency to a dynamic system, the system will start to oscillate at higher amplitudes, compared to when a non-resonant frequency is applied [11]. Another aspect to support this being a mechanical issue and not the sensor interface, is the varying amplitudes. A system being limited by the sensor interface bandwidth would have a close to constant amplitude for low frequencies, but the amplitude would gradually start to decrease for higher frequencies. However, this is not the case for this phenomenon.

Disregarding the variations in the vibration amplitude, the general amplitude measured is still lower than the amplitude applied. The exact reason for this is unclear, but it is also most likely a mechanical issue. Similarly to the test method used for the sensitivity measurements in Section 4.1, this is also not an optimal test method. Due to the way the pipe is mounted onto the vibration machine, the mirror will be forced to follow the linear movement of the applied vibration. Meanwhile, the pipe will try to force the mirror into its natural curvature. The result is most likely a middle ground between the two movements. This means that the angle of the mirror is not as big as it would be if a single point force was applied to the pipe, but bigger than if it just would have followed the linear movement of the vibration machine. Note that if the mirror would follow the movement of the vibration machine exactly, the mirror angle would stay constant and the laser beam would not move. A change of the laser beam would therefore not be detected by the sensor.

Chapter 5

Sensor Interface Improvements

This chapter will present the development of an improved sensor interface for the optical sensor system. A new sensor interface is developed to try to increase the system's deflection resolution, in addition to making a more complete sensor interface containing systems for sampling and transferring the measurement data.

5.1 Motivation for Improving the Sensor Interface

The initial performance tests of the test setup revealed some challenges with the system. The deflection resolution of the system was found to be six-and-a-half times worse than the stated goal, on average. The resolution of the system was found to be limited by the electrical noise on the displacement signals. This is mainly caused by two reasons. The overall noise on the four measurement signals, but also the differences in the noise levels for the four signals. For minimal noise on the deflection signals, the noise of the measurement signals should be as low as possible and as equal as possible. In Section 4.2 the transimpedance amplifier configuration and its voltage reference, was presented to be the two major reasons for the amount of noise appearing, hence important aspects to address in order to improve the deflection resolution of the system.

The differences in noise levels for the four channels is assumed to be a problem related to connection between the sensor interface PCB and the DAQ-unit. The measurement signals are transferred from the PCB to the DAQ-unit through breadboard wires. The wires are soldered onto the PCB and connected to a through hole terminal block on the DAQ-unit. The connection to the through hole terminal block has been proven to be very unreliable, where the movement of the wires has caused them to be easily disconnected or cause a bad connection. The difference in connection quality might be a reason for the differences in the noise levels seen on the four channels.

Based on these results, the main goal of the master's project was set to improve the resolution of the initial test setup, where the main objective was to reduce the noise of the measurement signals. A decision was therefore made to try to improve the sensor interface, focusing on the amplifier circuit, voltage reference generation, and the ADC. An additional goal of the

improved sensor interface, was to develop a more complete system. This meant including the ADC onto the same PCB as the sensor interface. This will possibly eliminate noise and problems related to the loose wires, as previously discussed. A more complete system will also make the implementation of the test setup onto a cutting tool easier, as the initial test setup is very bulky and vulnerable to being moved, due to the use of the DAQ-unit.

5.2 System Idea

Figure 5.1 depicts a block diagram displaying the general idea of the improved sensor interface. As presented, one of the goals was to include the sampling circuit onto the same PCB as the position sensor and the amplifier circuit. The inclusion of an ADC will also in most cases require a Microcontroller Unit (MCU) to control it and handle the measurement data. As with the previous sensor interface, all signal processing and visualisation will be performed on a PC. This means that a system for transferring the measurement data from the PCB to the PC is required. The main purpose of the MCU will therefore be to transfer the measurement data from the ADC to the data transfer unit.

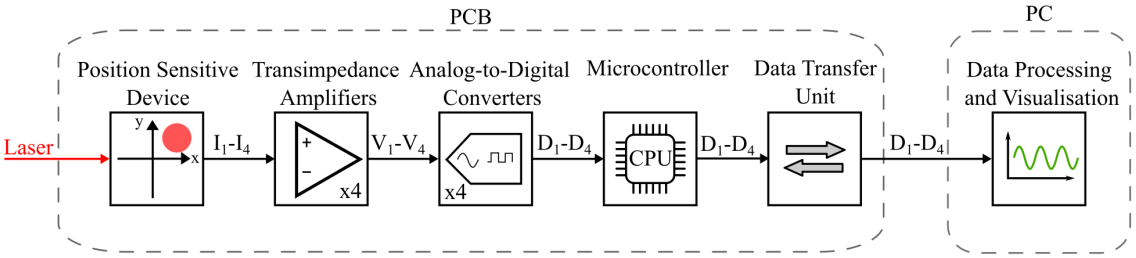

Figure 5.1: Block diagram displaying the general idea of the improved sensor interface. The system is similar to the initial sensor interface seen in Figure 3.21. The major differences being the implementation of an ADC on the same PCB. A microcontroller and a data transfer unit are also included for transferring the measurement data from the ADC to a PC, where the data will be processed and visualised to the user.

5.3 System Solutions

This subsection will present the specific solutions that was chosen to realise the improved sensor interface. Figure 5.2 depicts a block diagram which displays the overall solutions for the system that has been chosen. The different solutions chosen, and the functionality of the system will be presented through the following sections.

5.3.1 Position Sensitive Device

The purpose of this development was to improve the deflection resolution of the sensor system. The optical sensor was therefore not changed, as it is one of the most fundamental parts of the system. The PSD S5991-01 previously used was proven to be very suitable for the system with its high linearity and large sensor area.

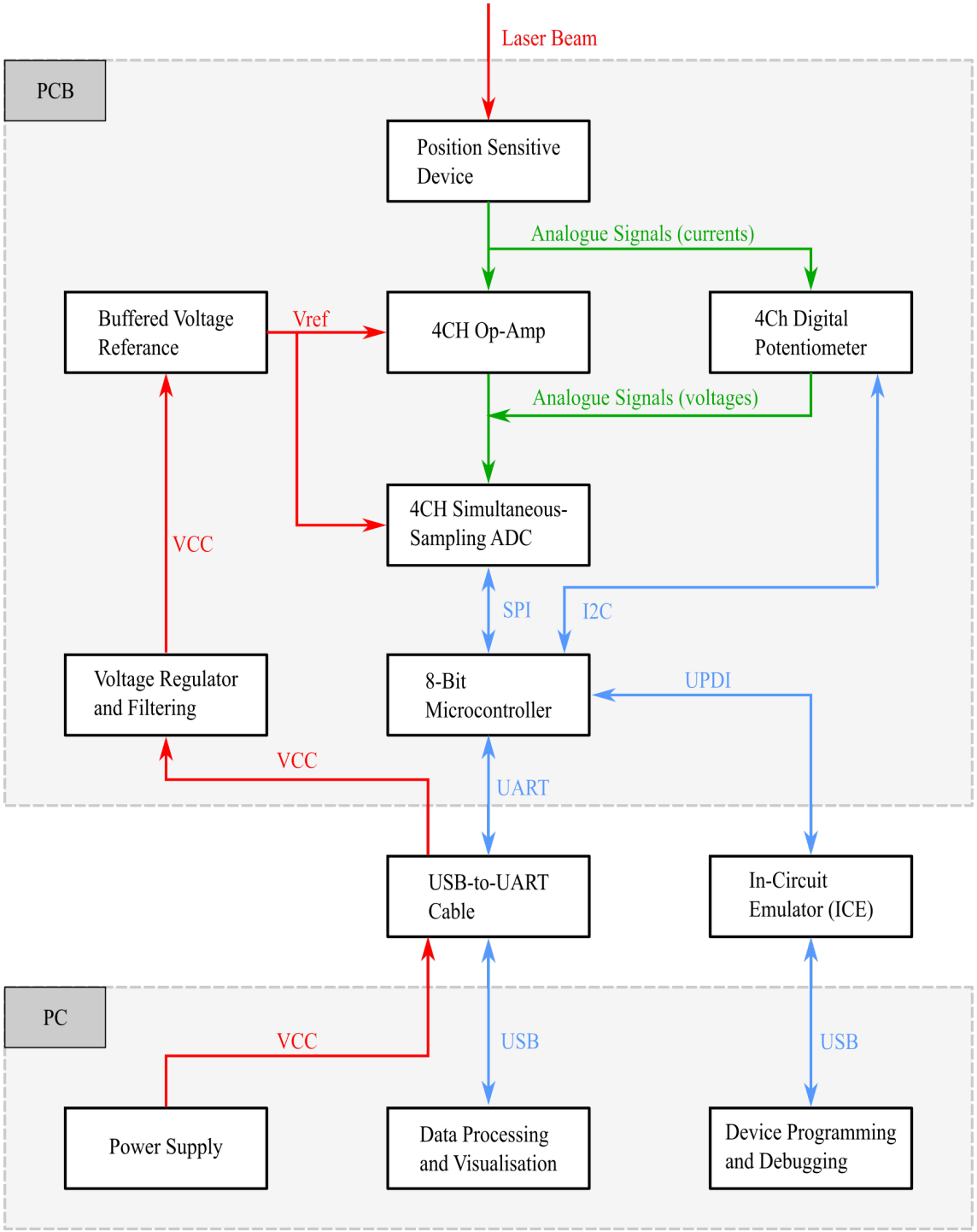

Figure 5.2: Block diagram displaying the solutions and overall functionality of the improved sensor interface. The individual components of the system are discussed in the following sub-sections.

5.3.2 Transimpedance Amplifier Circuit

The TIA used for the initial test setup was the AS89000, a four-channel programmable transimpedance amplifier. A problem with this component was the different programmable steps of gain. As discussed in Section 3.4.1, only the lowest gain resistor of 25 kΩ could be chosen due to photocurrents from the sensor being up to 120 µA. In order for the system to utilise the whole voltage span from 0 to 5 V the gain resistor needs to be 41.6 kΩ.

A big focus of the new sensor interface was to allow the weak photocurrents to be amplified as much as possible. This can be preferable due to the noisy voltage reference being added to the output signal. Amplifying the photocurrents will improve the Signal-to-Noise Ratio (SNR) by amplifying the signal and not the noise on the voltage reference. Note that any noise from the photocurrents will also be amplified, meaning that the noise contribution from this source will still be the same. This can for example be noise from the dark current of the PSD.

Another issue with the AS89000 was the programmable feedback capacitor, C_f. The feedback capacitor will work as a low pass filter, where the amplification of signal frequencies over the cutoff frequency, f_c, will be reduced, as presented in Section 2.3. However, due to an unclear datasheet, it is hard to understand what the two programmable capacitor values are.

Other transimpedance amplifier circuits were therefore researched, in order to find one that would solve these issues. The chosen solutions were to use a standalone op-amp circuit and external gain resistors and feedback capacitors. The op-amp chosen was the OPA4388 [12], a quad precision operational amplifier from Texas Instruments. In order to adjust the gain of the transimpedance amplifier, a digital potentiometer was chosen to function as the gain resistors. The digital potentiometer chosen was the MCP4462 [13] from Microchip. The component consists of 4 digital potentiometers which can be programmed to resistor values from 0 to 100 kΩ in 256 steps (2^8). The device can be programmed by a microcontroller using the communication protocol I2C.

The value of the feedback capacitors was calculated using a variation of Equation (2.5). By rearranging the equation the required feedback capacitor value can be calculated by specifying the gain resistor value and the wanted cutoff frequency. To ensure that all signal frequencies within the stated vibration bandwidth of 500 Hz gets amplified sufficiently, a cutoff frequency 10 times greater is chosen. This results in a preferred cutoff frequency, f_c, of 5 kHz. The required feedback capacitor value is then found to be 318.3 pF, as presented in Equation (5.1)

$$C_f = \frac{1}{2\pi \cdot R_f \cdot f_c} = \frac{1}{2\pi \cdot 100\,\text{k}\Omega \cdot 5\,\text{kHz}} = 318.3\,\text{pF} \tag{5.1}$$

Note that this will only apply when setting the digital potentiometer to 100 kΩ. Changing the gain resistor value to for example 50 kΩ or 25 kΩ, while using the same feedback capacitor, will result in cutoff frequencies of 10 kHz and 20 kHz respectively.

To ensure stability of the transimpedance amplifier system and that the gain bandwidth of the op-amp is adequate, the guidelines in [14] have been followed. After verifying that these aspects of the system were correct, 330 pF capacitors were chosen as the feedback capacitors, as these were the closest standard values.

5.3.3 Voltage Reference Generation

In Section 4.2, the importance of a good voltage reference for the transimpedance amplifiers was discussed. Due to the way the TIAs are configured, the voltage reference will be directly added to the output signal. By using a simple voltage divider to create the reference voltage, the noise from the voltage supply will be directly coupled to the voltage reference signal. A stable and relative noise free voltage reference is therefore preferred in order to reduce the noise on the output signals.

Through the development of the improved sensor interface, the whole system was built upon a breadboard first. This allowed for testing different voltage reference configurations. The resistor values of the voltage divider were reduced by a factor of 10, in order to reduce impedance of the voltage divider. This also reduced the amount of noise from the voltage supply. In addition, decoupling capacitors were added over the voltage divider, which also reduced some amount of noise.

In addition to improving the voltage divider, another solution was tested. This was using a buffered voltage reference, which is built to generate a stable reference voltage. One of the main advantages of using a buffered voltage reference, is that the output voltage from this device will not be impacted much by variations on the voltage supply. The device tested was the MCP1501-40 [15], a high precision buffered voltage reference from Microchip. This exact version can take input voltages from 4.3 V to 5.5 V and output a voltage reference of 4.096 V. Both solutions have been compared by using the same power supply and sampling both signals at once. The result is depicted in Figure 5.3.

The supply voltage used in this test is coming from the USB-port of the PC used, through a USB-to-UART cable. The generation of the supply voltage will be further discussed in Section 5.3.6. From the graphs in Figure 5.3, it is possible to see how the two different voltage references are affected by variations in the supply voltage. The blue graph is showing the 5 V supply voltage. The signal has slow oscillations with a PTP value of about 7 mV. The same variation can be seen in the orange graph, which is the voltage reference generated by the voltage divider. However, the PTP value is now about 2.5 mV. The yellow graph depicts the voltage reference generated by the MCP1501. The PTP value of this signal is about 3 mV and the mean value is very close to its expected value of 4096 mV. The variations seen on the voltage supply can not be seen in this signal.

Upon comparing the two solutions, the MCP1501 was chosen for the sensor interface. The noise levels of MCP1501 might be a bit worse than the voltage divider. However, the offered stability of this buffered voltage reference is preferable for the transimpedance amplifier system.

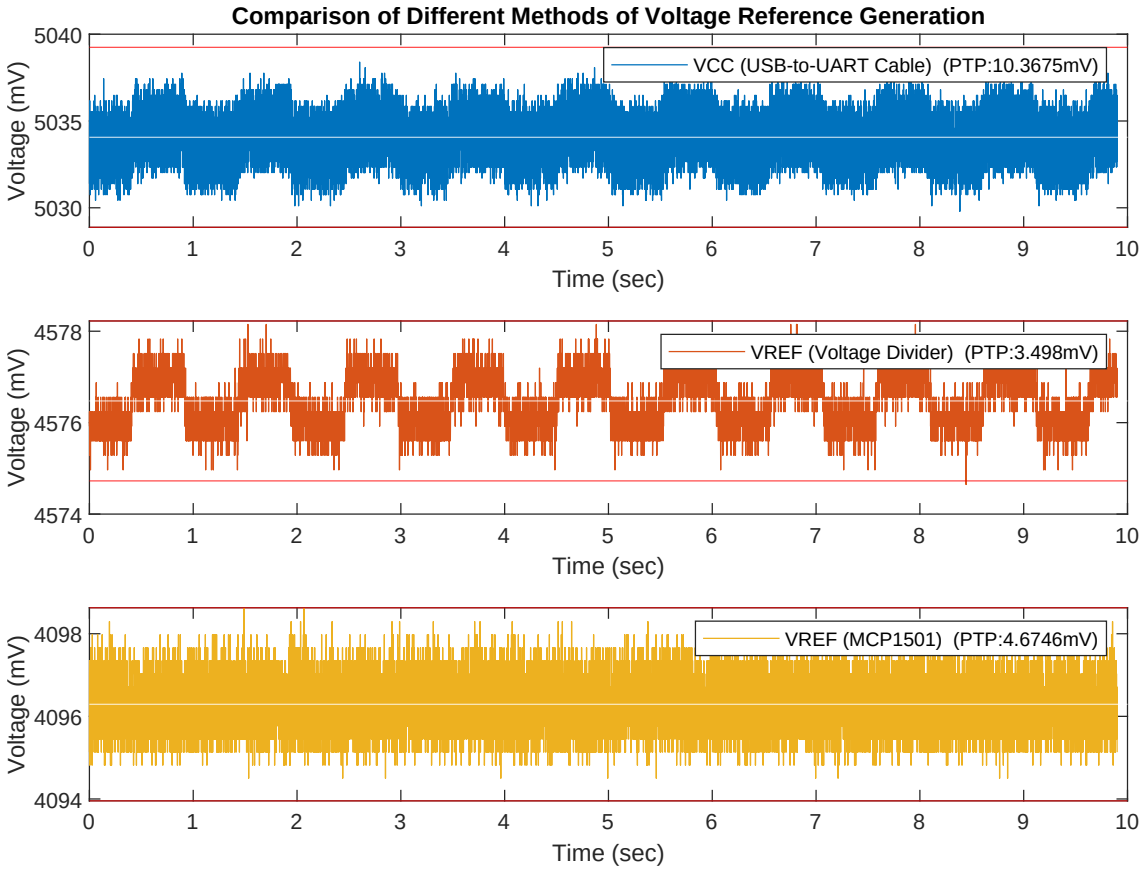

Figure 5.3: Comparison of different methods of voltage reference generation. The figure displays how variations in the supply voltage, VCC, impacts the two different voltage references. The middle graph displays the voltage reference generated by a voltage divider, which gets heavily affected by the variations in the voltage supply. The lower graph display the reference voltage generated by the MCP1501, which reveals that noise from the voltage supply has little impact on it.

5.3.4 Sampling Circuit

Differential ADC configuration

As presented, an ADC is required in order to digitalise the four measurement signals. The measurement signals coming from the outputs of the transimpedance amplifiers are equal to the voltage reference minus the sensor signal, as seen in Equation (2.4). Previously the output voltage, V_{out}, has been sampled by the DAQ-unit by connecting the positive terminal of the ADC to V_{out} and the negative terminal to ground. In LabVIEW where the signals were processed, the signals would be subtracted by a constant in order to remove the DC-contribution from the voltage reference. This is not optimal as it does not remove the noise contribution from the voltage reference. A way of solving this problem is to use the ADC configuration depicted in Figure 5.4.

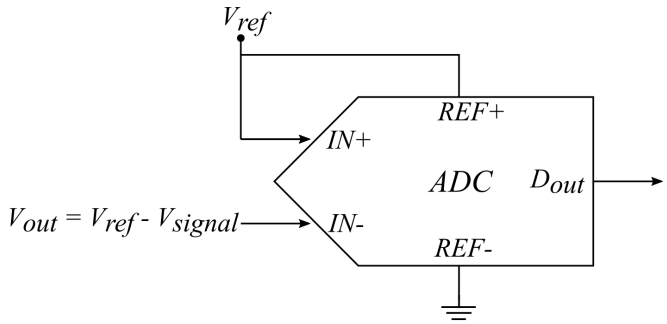

Figure 5.4: A differential ADC configuration where the voltage reference, V_{ref}, is connected to the positive input terminal and the transimpedance amplifier output, V_{out}, is connected to the negative terminal.

Figure 5.4 depicts a differential ADC configuration. Instead of connecting the signal to the positive terminal and ground to the negative terminal, like in a single-ended configuration, two signals are connected to the two terminals. By connecting the voltage reference, V_{ref}, to the positive terminal and the transimpedance amplifier output, V_{out}, to the negative terminal, the ADC will effectively only measure the sensor signal, V_{signal}. This can be explained by how a differential ADC determines its output data, D_{out}.

$$D_{out} = \frac{(IN^+ - IN^-)}{(REF^+ - REF^-)} \cdot \frac{2^n}{2} = \frac{(V_{ref} - (V_{ref} - V_{signal})}{(V_{ref} - 0)} \cdot \frac{2^n}{2} = \frac{V_{signal}}{V_{ref}} \cdot \frac{2^n}{2} \tag{5.2}$$

From Equation (5.2) we can see that the input of the negative terminal is subtracted from the input of the positive terminal. Using the configuration depicted in Figure 5.4, we can see that voltage reference, V_{ref}, is cancelled out. This results in the digitalised data effectively being just the V_{signal}. The potential input range of the V_{signal} will for this differential configuration be $-V_{ref}$ to $+V_{ref}$. However, the V_{signal} from the TIA will never go below zero. This makes the effective input range of the V_{signal}, 0 to $+V_{ref}$, which will correspond to a digital output of 0 to $2^n/2$, where n is the ADCs resolution in number of bits. This means that the system will only utilise half of the ADCs resolution. For example, the system would only utilise 32768 (2^{15}) steps of a 16-bit ADC with 65536 (2^{16}) steps.

Programmable Gain Amplifier

Many ADCs have a Programmable Gain Amplifier (PGA) stage included. This stage is used to amplify low-amplitude input signals so they can utilise the whole the measurement range of the ADC, effectively increasing the resolution of the captured signal. This kind of amplifier system was considered but abandoned due to an important detail. On the differential ADCs that was considered, the amplification occurs before the signal comparison. This means that the signals that would be amplified is the reference voltage, V_{ref}, and the output voltage, V_{out}. This would not work, as amplifying these signals would make them much larger than the input range of the ADC. A PGA stage was therefore not set as a requirement when searching for a suitable ADC.

Multiplexed vs. Simultaneous-Sampling

There are multiple ways one could sample the four sensor signals coming from the TIA. One way is to use a multiplexed ADC. A multiplexed ADC uses one sampling unit to sample all four signals. This is done by sampling one signal at a time and multiplexing the inputs of the sampling unit to sample all four signals. This is often used because it is a cost-effective method, requiring only one sampling unit. A potential problem with using a multiplexed ADC, is that there will be a time delay between the sampling moment of the four signals. This is not preferred as the four signals are used to calculate a position at an exact moment. Another disadvantage might be the rejection of common mode noise. As seen, the system heavily favours common mode noise. This is because the noise gets cancelled out when calculating the deflection signals. A time delay between the channels will result in a difference in the noise levels at the same sample point, which will weaken the system's ability to reject common mode noise.

Another solution is to use a simultaneous-sampling ADC. This type of ADC contains multiple sampling units in one ADC. The sampling units are configured to sample the different signals at the exact same time. Simultaneous-sampling can also be achieved by using multiple ADCs. However, it will often get more complex as additional hardware is required to synchronise the ADCs. From these three solutions, the simultaneous-sampling ADC was considered to be the best choice for this system.

ADC Resolution

The resolution of the ADC used for the initial system was presented in Section 4.2.4. With a voltage input range of +-10 volt the ADC resolution was calculated to be 0.3052 mV. From the same equation, the resolution for a 16-bit differential ADC using the configuration previously presented can be identified. By using the voltage reference of 4.096 V the ADC voltage resolution, Q, is calculated to be 0.125 mV using Equation (5.3).

$$Q = \frac{E_{FSR}}{2^n} = \frac{+-4.096\,\text{V}}{2^{16}} = \frac{8.192\,\text{V}}{2^{16}} = 0.125\,\text{mV} \tag{5.3}$$

From the noise measurements of the initial setup, it was clear that the ADC voltage resolution was not limiting the deflection resolution. This was because the PTP noise amplitude was identified to be about 23 times higher than the ADC voltage resolution. However, if the noise of the measurement channels is to be improved, the ADC resolution might start to be the limiting factor. A resolution requirement for the ADC was therefore set to be 16-bit or higher.

Choosing an ADC

The final requirement set for the ADC was the sampling frequency. The sampling frequency was set to be at least ten times higher than the highest signal frequency. This is to ensure that the signal is reconstructed as close as possible to the original signal [16]. A lower sample rate than this might cause the amplitude of the reconstructed signal to be lower than the original signal. As the system is set to measure vibrations up to 500 Hz, the minimum sample frequency requirement was set to 5 kHz.

After setting the main requirements, the search started for a four-channel differential simultaneous-sampling ADC, with at least 16-bit resolution and 5 kHz sampling frequency. This led to three different ADCs: The MCP3912 [17] from Microchip, the ADS1174 [18] and the ADS131A04 [19] both from Texas Instruments. After comparing the ADCs, the ADS131A04 was chosen. The MCP3912 was abandoned due to the limited ADC input voltage span compared to the two other options. The ADS1174 was less preferable due to its small footprint. This was only important because the PCB was going to be hand soldered.

The ADS131A04 is a four-channel simultaneous-sampling delta-sigma ADC with a sample rate up to 128 kHz and a 24-bit resolution. The ADS131A04 requires a digital supply voltage between 1.65 V to 3.6 V and an analogue supply voltage between 3.3 V to 5.5 V. Using an analogue supply voltage of 5 V will allow for analogue input signals from 0 to 5.3 V. The differential ADC configuration previously presented will therefore work on this ADC, as the input signals will be between 0 and 4.096 V. The communication interface of the ADS131A04 is Serial Peripheral Interface (SPI).

5.3.5 Microcontroller and Data Transfer Unit

As the main purpose of the sensor interface improvements was to reduce the noise of the measurement signals, most of the focus was on the analogue parts of the system and not the digital parts. This means that the microcontroller and the data transfer unit was chosen to be an easily implementable solution, but maybe not the most optimal solution.

The process started with researching different methods for transferring the digital measurement data from a microcontroller to a PC. The solution which was considered the easiest to implement was to use a USB-to-UART bridge. Most USB-to-UART bridges work by converting UART data from the microcontroller to USB data which can be read by a PC, and vice versa. The communication device will appear as a virtual communication port on the PC side. This means that any program that can interact with a serial communication port can be used to read and write data to the microcontroller. Instead of using an IC with a USB-to-UART bridge, a USB-to-UART cable was chosen. This was to reduce the amount of components required,

allowing for a smaller PCB. The USB-to-UART cable chosen was the TTL-234X-3V3 [20] from FTDI Chip. The TTL-234X-3V3 communicates over UART at 3.3 V levels. However, the cable can also be used to supply the PCB with the 5 V USB supply voltage from the PC.

The microcontroller chosen for the system was the ATtiny1626 [21] from Microchip. This is an 8-bit microcontroller with one SPI, one I2C and two UART communication interfaces. This is a good fit as the required communication interfaces' is SPI for the ADC, I2C for the digital potentiometer and UART for the USB-to-UART cable. The microcontroller requires a supply voltage between 1.8 V to 5.5 V and can utilise an internal oscillator running up to 20 MHz. The microcontroller can be programmed over Unified Program and Debug Interface (UPDI) using an In-Circuit Emulation (ICE) device. UPDI is a programming and on-chip debugging interface developed by Microchip, which only requires one data pin of the microcontroller in order to communicate with the it. An ICE device is a hardware device used to program and debug the microcontroller from the PC.

5.3.6 Power Supply

In Section 5.3.4 it was presented that the chosen ADC required a digital supply voltage between 1.65 V to 3.6 V and an analogue supply voltage between 3.3 V to 5.5 V. As a focus of this development was to be able to amplify the measurement signals as much as possible, as discussed in Section 5.3.2, the voltage reference was set to 4.096 V. This means that the ADC must be able to sample signals in the range of 0 to 4.096 V. As the analogue supply voltage of the ADC must be greater than the input signals, it was sensible to set the analogue supply voltage to 5 V. This could then be supplied from the USB-port of the PC, using the USB-to-UART cable. Other components related to the analogue part of the system were also set to use the same 5 V supply voltage. This included the buffered reference voltage, the four-channel op-amp, and the digital potentiometer.

To fulfil the digital supply voltage requirement the MIC5319-33YD5-TR [22] was chosen. This is a linear ultra-low dropout regulator which can take 2.5 V to 5.5 V and output 3.3 V. The regulator has therefore been used to make a 3.3 V supply voltage from the initial 5 V supply voltage. In addition to powering the digital part of the ADC, the 3.3 V was also used to power the microcontroller.

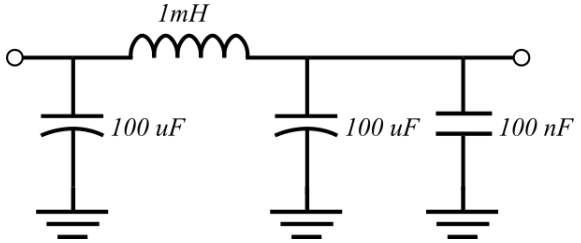

Figure 5.5: Implemented π-filter. The filter acts as a low pass filter, suppressing noise at high frequencies. The filter consists of two tantalum capacitors at 100 µF, one ceramic capacitor at 100 nF and an inductor at 1 mH.

When using the supply voltage from the USB-port of a PC, the quality of the supply voltage will be mainly depend on the power supply of the PC. This supply voltage can be quite noisy and will depend heavily on the PC being used. In order to reduce some of the noise on the

supply voltage, a π-filter is implemented close to the supply voltage input, prior to both the buffered reference voltage component and the 3.3 V voltage regulator. The implemented π-filter is depicted in Figure 5.5.

The filter acts as a low pass filter, suppressing noise at high frequencies. The cut-off frequency for this filter is calculated to be 503 Hz. The supply voltage from the USB-to-UART cable connected to a PC, has been measured with and without the π-filter. The results can be seen in Figure 5.6.

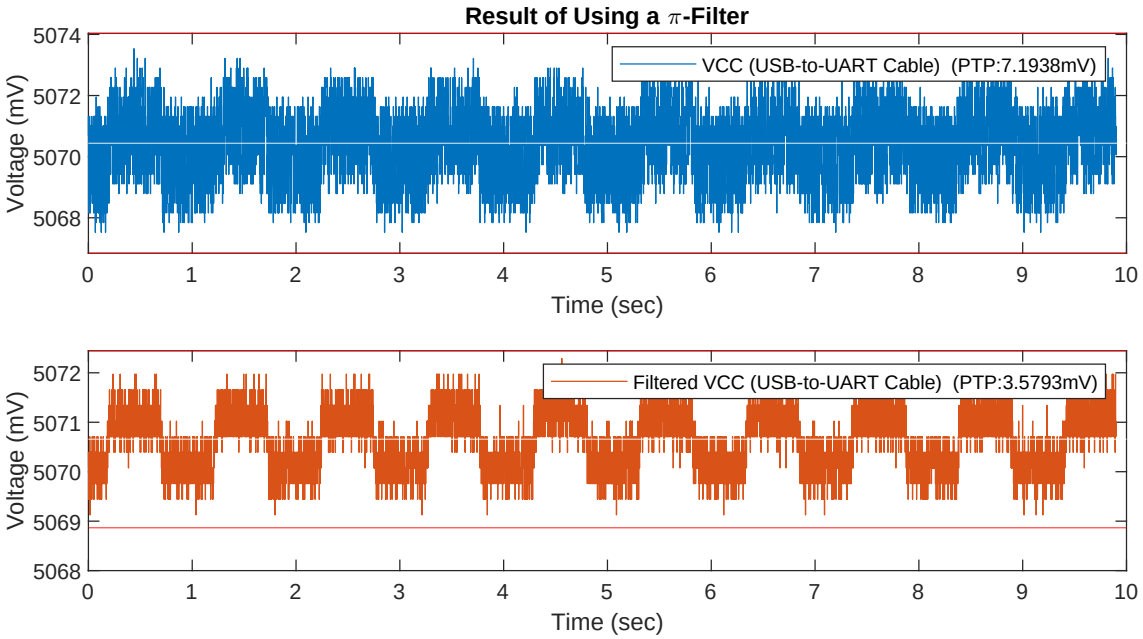

Figure 5.6: Result of using a π-filter. The two graphs display the supply voltage from the USB-to-UART with and without the use of the π-filter.

From Figure 5.6 we can see that some noise is suppressed using the π-filter. In this measurement the noise amplitude is approximately halved using the π-filter.

5.3.7 Data Processing and Visualisation

The applications for data processing and visualisation were the same as in the initial test setup. This meant using LabVIEW to import, process, visualise and store the measurement data. MATLAB was used to analyse the saved measurement data. One major difference is how the measurement data is imported into LabVIEW. Previously control blocks called DAQmx were used. These control blocks are used to easily import and handle measurement data coming from compatible DAQ-devices. This was no longer possible as the new system acts as a serial device. The solution to this was using control blocks called Serial VISA. These blocks allowed for easy implementation of serial communication in LabVIEW.

5.3.8 Component Summary

The main components chosen for the improved sensor interface are listed in Table 5.1.

System Component	Part Number	Link
Position Sensitive Device	S5991-01	[5]
4CH Op-Amp	OPA4388	[12]
4CH Digital Potentiometer	MCP4462	[13]
4CH Simultaneous-Sampling ADC	ADS131A04	[19]
8-bit Microcontroller	ATTINY1626	[21]
USB-to-UART cable	TTL-234X-3V3	[20]
Buffered Voltage Reference	MCP1501-40	[15]
Voltage Regulator (3.3V)	MIC5319-33YD5-TR	[22]

Table 5.1: Summary of the main components chosen for the improved sensor interface.

5.4 System Development

In parallel with the process of choosing components, the sensor interface was gradually built upon a breadboard. This allowed for testing and code developing on parts of the system, even though not all components had been chosen yet. This made the development process more effective. All chosen components were ordered in the same SMD package as the ones that would be used for the PCB design. This required various breadboard adapters which the SMD components could be soldered to in order to be connected to the breadboard. The main advantage of using this solution is that a working breadboard setup can easily be converted to a PCB design, as the same component types can be reused.

Figure 5.7 depicts the complete improved sensor interface that was built upon a breadboard. The complete sensor interface is built on the big breadboard, except the sensor which is mounted on another breadboard in order to more easily measure the laser spot coming from the optomechanical system. Both the USB-to-UART cable and the Atmel-ICE debugger are connected to the same PC using two USB-ports. This made it possible to program and debug the microcontroller using the debugger and the Integrated Development Environment (IDE), Microchip Studio. At the same time LabVIEW, in combination with the USB-to-UART cable, could be used to read the measurement data of the system. In addition, LabVIEW can be used to send commands to the system, as for example "Start ADC Measurement".

Basic tests were performed to ensure that the system was working as intended. The performance tests were saved for the PCB version of the system, as the breadboard setup was expected to have more signal noise than the PCB version. Especially due to the relatively long breadboard wires between the sensor and the op-amp circuit. These wires are preferred to be kept as short as possible to reduce the interference on the weak photocurrents running through them.

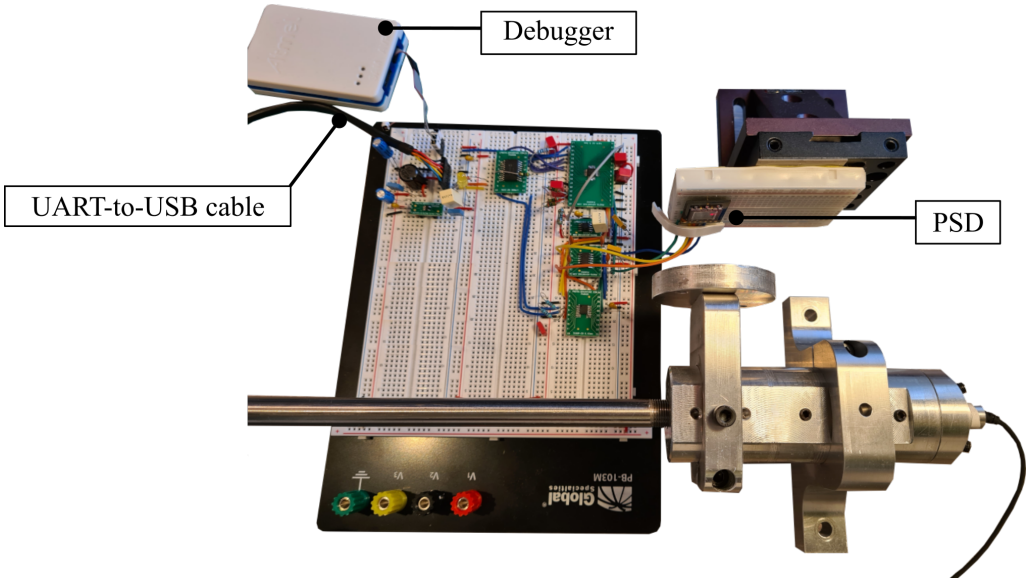

Figure 5.7: The whole improved sensor interface built upon a breadboard. The Position Sensitive Device (PSD) was kept to a separate breadboard, making it easier to measure the laser spot of the optomechanical system. The debugger is used to program and debug the microcontroller. While the USB-to-UART cable is used to transfer measurement data to LabVIEW and system commands to the microcontroller.

5.5 PCB Design

After ensuring that the basic functionality of the breadboard setup was working, a PCB of the same system was designed in Altium Designer. The schematic of the PCB can be seen in Appendix A. In addition to the main system components presented in Section 5.3, various decoupling capacitors and pull-up resistors have been included. Most of these components was selected based on the design recommendations in the datasheets of the different components. Two different connectors have been added, which will allow for easy connection of the debugger and the USB-to-UART cable to the PCB.

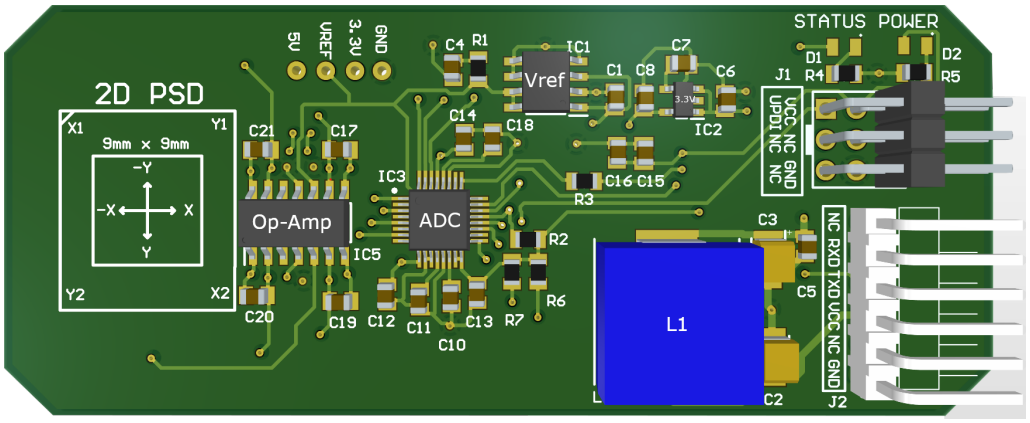

Figure 5.8: 3D model of the PCB for the improved sensor interface, front side. The analogue and the digital part of the system are sectioned into two sides of the PCB. Where the analogue section is seen on the left side and the digital section on the right side.

Figure 5.8 and 5.9 depicts the 3D model of the designed PCB. The block diagram presented in Figure 5.1 is a good representation of the actual PCB layout. The analogue components are placed towards one edge and the digital components towards the opposite edge. The ADC is placed in the middle of the two sections. In addition, the power supply components are located on the same section as the digital components. The reason for this layout is to shield the sensitive analogue signals from noise interference of the digital components. An important layout aspect is the placement of the sensor, op-amp and digital potentiometer. These components are kept as close as possible in order to reduce the signal path of the photocurrents. To minimise the distance between the op-amp component and digital potentiometer, these components are placed directly above each other on the two sides of the PCB.

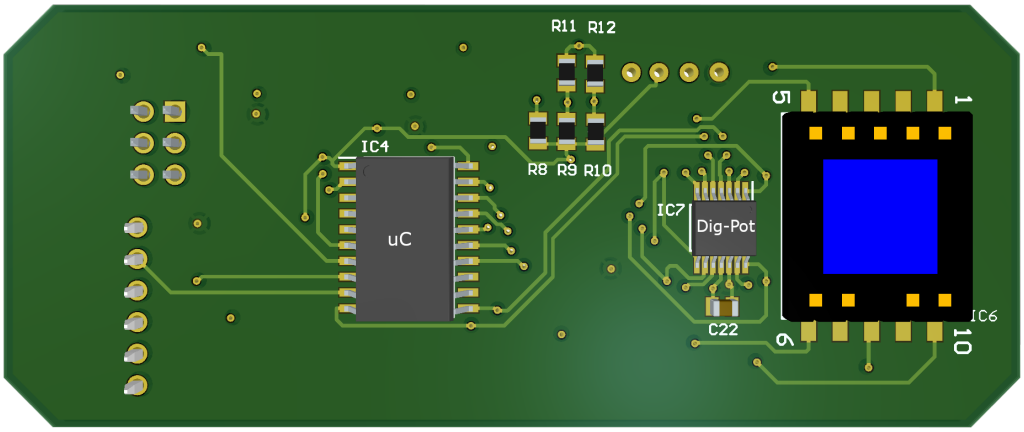

Figure 5.9: 3D model of the PCB for the improved sensor interface, back side. The analogue and the digital part of the system are sectioned into two sides of the PCB. Where the analogue section is seen on the right side and the digital section on the left side.

Another important aspect of the PCB is that it consists of 4 layers. The two outer layers are used for components and signal traces, and the two inner layers consists of a power plane and a ground plane. These planes appear as low-impedance paths for the signals and are used to reduce noise in the circuit [23]. The layout of the signal paths is better depicted in the figures found in Appendix B.

5.6 Finalised Sensor Interface

5 PCBs were ordered from, and produced by JLCPCB. One of the PCBs was assembled by soldering all the required components. Basic tests verified that no major error had been made in the PCB design process.

In order to use the new sensor interface with the optomechanical system, the mechanical component housing the initial sensor interface was modified. No other changes to the optomechanical system were required in order to use the new sensor interface. The test setup with the improved sensor interface is depicted in Figure 5.10

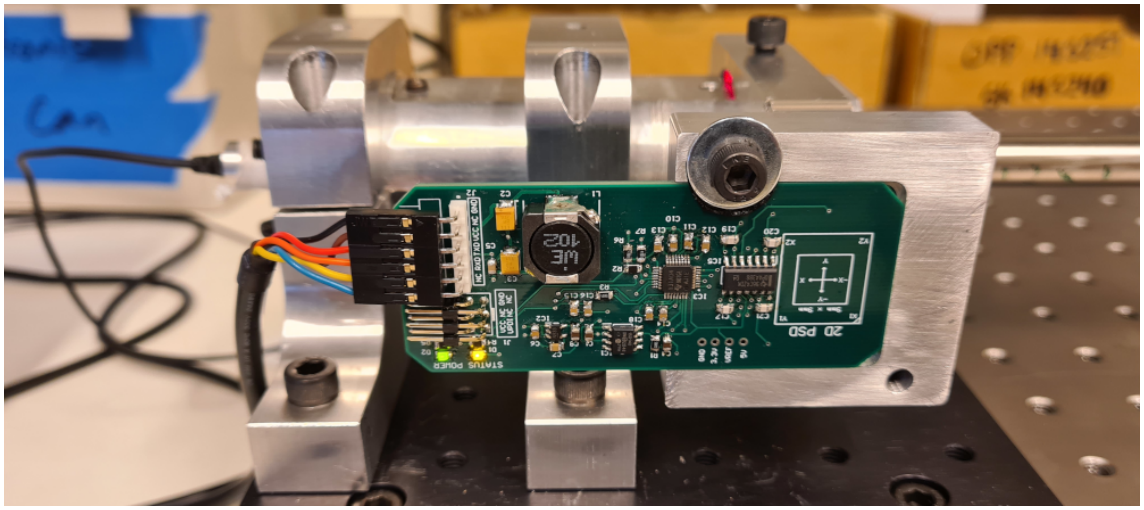

Figure 5.10: Test setup with the improved sensor interface. The optomechanical system is identical to the one presented in Chapter 3, except for the component used to mount the PCB.

5.6.1 Known Problems with the Improved Sensor Interface

I2C Communication Between Microcontroller and Digital Potentiometer

There are two major problems with the improved sensor interface, which is known at the time of writing. One being a problem related to communication between the microcontroller and the digital potentiometer. Initially, the digital potentiometer IC was planned to be powered by the digital supply voltage of 3.3 V. Upon developing the breadboard setup, it was discovered that this would not work, as the input signal voltage on the potentiometer channels must be lower than the supply voltage. This requirement was not met as the input signal voltage can be up to 4.096 V. The analogue supply voltage of 5 V was therefore used to power the digital potentiometer. This was not optimal as the microcontroller was powered by the digital supply voltage of 3.3 V. This meant that the microcontroller was communicating over I2C with signal levels of 3.3 V, while the digital potentiometer was expecting signal levels of 5 V. However, this did not cause any problems while testing the system on the breadboard, and was therefore not addressed further.

While testing the PCB it was no longer possible to communicate with the digital potentiometer. However, the problem was not related to the PCB, but the supply voltage from the USB-port used. Upon testing, it was discovered that using a USB-port with 5.03 V would work, while using a USB-port with 5.09 V would not. This was tested with other USB-ports on other computers with the same results. This problem is most likely related to the difference in supply voltage for the two components and can be fixed by implementing a logic level converter on the communication lines.

Limited Data Transfer Speeds

The second problem is related to the transfer speed between the microcontroller and PC, meaning that some parts of the system can not keep up with the rate which the ADC outputs data. The highest data rate of the ADC that has been transferred and displayed correctly is at 2.4 kHz. This was when the ADC was configured to send measurement data with 24-bit resolution, but only 16 of these were sent from the MCU to the PC. This means that the ADC is outputting sampled measurement data 2400 times per second. Note that each sample consists of 18 bytes of data, where 12 of these bytes are the measurement data. The 12 bytes are made up of the measurement data of the 4 sampling units with a 24-bit (3 bytes) resolution. 18 bytes, 2400 times a second, results in a data rate of 345.6 kilobits per second (kbps). Only 16-bits of these were sent from the MCU to the PC. This results in a data rate of 240 kbps. Through testing, it is observed that the microcontroller can transfer data over UART up to 440 kbps when not interacting with the ADC. The most likely reason for the limited transfer speeds is therefore that the microcontroller can not both receive data from the ADC and send the data to the PC at such speeds. This is most likely because of poorly optimised code for the MCU. Due to time priorities this problem was not analysed further. This means that the measurement data imported into LabVIEW only has a 16-bit resolution instead of 24-bit. In addition to the sampling speed being maximum 2.4 kHz.

Chapter 6

Test Setup Performance with Improved Sensor Interface

This chapter will present the different tests performed on the test setup using the improved sensor interface. The exact same tests that were performed on the initial test setup, as presented in Chapter 4, were also performed on this setup. This was done to compare the performance of the two sensor interfaces.

6.1 System Sensitivity and Measurement Range

For this system test, only the reflection configuration was tested, as this is the one being used for the later measurements. Using the same test method presented in Section 4.1, the sensitivity curve for this setup was measured. The sensitivity slope of the system was found to be nearly identical to the initial system. This is to be expected as the sensor still remains the same. A difference in the two measurements was the measured mechanical range. This is most likely just a result of the laser beam being aligned slightly differently for the two measurements.

Due to the way the laser spot position is calculated, the optical effect of the laser beam is irrelevant. This is because it is the relative position that is determined. This means that the calculated position just indicates the relative difference between the four measurement signals. Increasing the laser beam effect by a factor of x, would also increase each measurement signal by a factor of x. However, the relative difference would still remain the same. The exact same concept applies when amplifying the signals using the transimpedance amplifier in combination with the digital potentiometer. This means that the gain of the TIA will not impact the calculated position of the laser spot. This is very advantageous as the same displacement-to-deflection ratio can be used independently of the selected gain of the TIA. For that reason, the same displacement-to-deflection ratio of 0.3588 is also used for this system.

6.2 Deflection Resolution and System Noise

All the different noise measurements performed on the initial test setup have also been performed on this setup. The only difference is that the sample frequency of the initial system was 1000 Hz, while this setup uses a sampling frequency of 1220 Hz. The value of 1220 Hz was chosen as it is the closest possible option. Other possible options in this range would be 610 Hz or 2440 Hz.

Figure 6.1 displays a noise measurement where the laser was placed in the center of the sensor and the gain resistors, R_f, of the digital potentiometer was set to 50 kΩ. These graphs show signals which are very different from the measurements of the previous system. The main reason for this is that the noise on the measurement channels have decreased and is now just a bit larger than the ADC voltage resolution. The ADC voltage resolution has been calculated to be 0.125 mV when using only the 16 most significant bits of the ADC. The ADC voltage resolution can easily be seen in the measurement signals as the smallest change in the signals. Due to the noise amplitude being only about 3 times the ADC voltage resolution, it is very hard to see any noise patterns in the measurement signals.

Another aspect that is apparent in most of the noise measurements performed on the improved sensor interface, is a slight drift in the measurement signals. The four measurement signals in Figure 6.1 have fairly equal noise amplitudes, but different degrees of signal drift. Signal drift is not preferable as it generates an error between the measured and actual signal. This means that the deflection resolution will not be limited by the electrical noise or the ADC resolution, but the drift on the measurement signals. The reason for the drift is unclear. A possible reason can be a slight drift in the voltage reference. However, this would theoretically make the drift of the four measurement channels equal, which is not the case. Another possible explanation is that the resistance over the digital potentiometers varies with the temperature. This will cause the amplitude of measurement signals to vary correspondingly. Thermal expansion causing the laser beam to be displaced, could also be a possibility. However, a displacement of the laser spot would cause some of the measurement signals to increase and others to decrease, which is not the case for this measurement.

Disregarding the different amounts of drift on the measurement channels, the noise levels are fairly similar. This is positive as it makes the noise levels of the deflection signals lower, as discussed in Section 4.2.3.

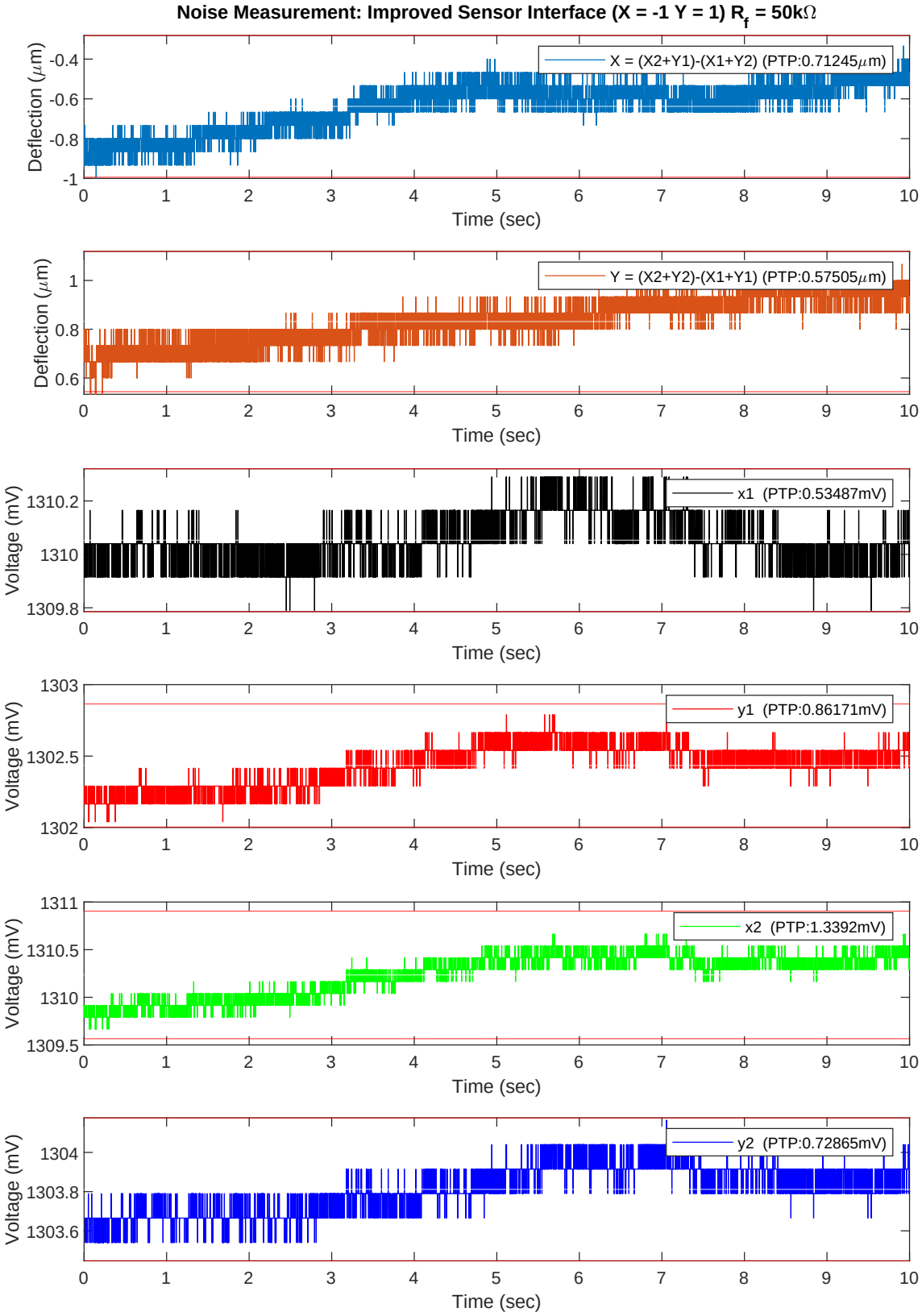

Figure 6.1: Noise measurement with the improved sensor interface. The laser is placed in the middle of the sensor and the gain of the digital potentiometer is set to 50 kΩ. The noise levels of the measurement signals are only a few times bigger than the ADC voltage resolution, making it hard to detect any noise patterns. A slight drift can be seen on the signals.

Impact of Gain

As presented in Section 5.3.2, the improved sensor interface utilises a programmable potentiometer to adjust the gain of the measurement signals. The gain resistor can be adjusted from 0 to 100 kΩ in steps of about 390 Ω. Noise measurements have been performed with different gain resistor values to analyse the effect of adjustable gain. Figure 6.2 displays parts of two different noise measurements. One using a gain resistor value of 25 kΩ and the other 100 kΩ. The upper graph displays the deflection signal in X direction for both measurements, while the lower graph displays the measurement signal x1 for both measurements. In these graphs the DC-level of the signals are removed to make a clear comparison. In reality, the DC level of the 100 kΩ measurements is about 4 times bigger than the DC level of the 25 kΩ measurements.

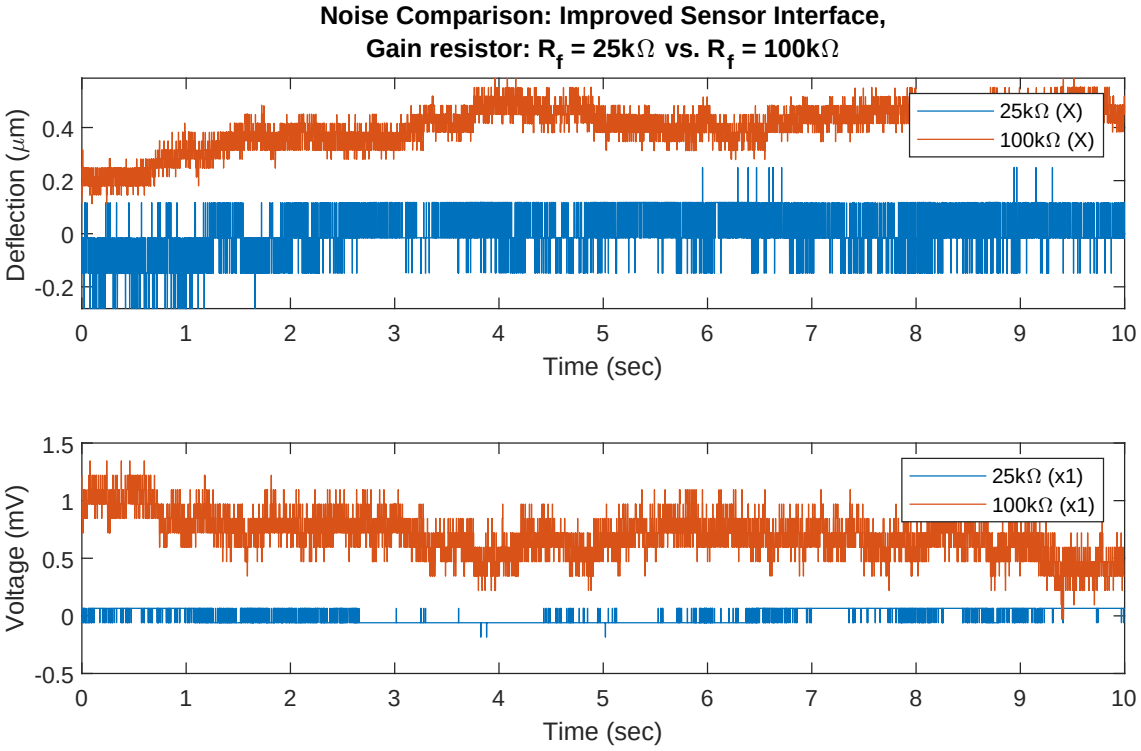

Figure 6.2: Noise comparison of different signal gain values. The orange signals represent a gain value of 100 kΩ, while the blue signals represent a gain value of 25 kΩ. Despite the orange measurement signal having higher noise amplitudes, due to a higher gain, the two deflection signals are considered to have fairly equal noise amplitudes. The full measurements can be seen in Appendix F.4 and F.6.

It is hard to tell the exact noise levels of the 25 kΩ signals due to them being limited by the ADC voltage resolution. However, from the lower graph we can see that the 100 kΩ signal has about 4 times bigger amplitudes, while in the upper graph the noise amplitudes of the two signals are almost equal. From this it is not possible to state that the noise amplitudes on the deflection signals are changed by the applied gain. However, it is very clear that a higher gain setting is preferred in order to display a more detailed deflection signal. Note that the preferred gain value for the system is about 50 kΩ. A higher gain than this will saturate the measurement channels at certain positions of the laser spot. This will result in false readings.

Improvements in Noise Levels

Figure 6.3 compares two noise measurements. One from the initial sensor interface and one from the improved sensor interface. Both measurements have been previously presented in Figure 4.8 and 6.1. From Figure 6.3 it is clear that the improved sensor system has managed to reduce the noise of both the measurement signals and the deflection signals.

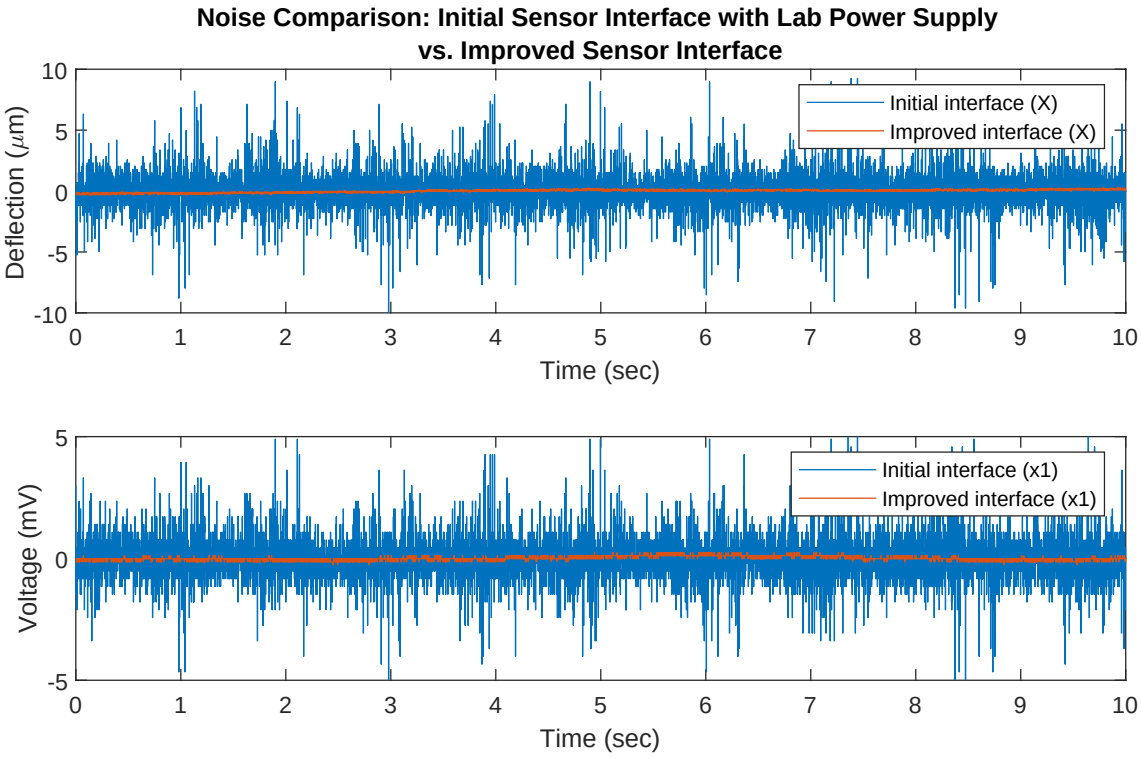

Figure 6.3: Noise comparison of the initial sensor interface using the lab power supply, and the improved sensor interface. The figure displays a comparison of both deflection signals and measurement signals.

To further compare the noise levels of the two system's, the noise comparison table seen in Section 4.2.5 has been updated with the data of the new sensor interface. Note that the PTP values for the improved system, seen in Table 6.1, includes the drift seen on the signals. The table reveals that the average noise levels on the deflection signals has a 9 times improvement. While the average noise on the measurement signals has a 7 times improvement. The deflection resolution of the test setup with the improved sensor interface is stated to be 0.7 µm.

	Deflection (µm)			Voltage (mV)		
Sensor Interface	Min	Avg.	Max	Min	Avg.	Max
Initial with Biltema PSU	3.48	5.87	9.33	6.18	7.69	9.16
Initial with Lab PSU	4.12	7.15	8.76	3.35	6.19	8.90
Improved	0.42	0.70	1.62	0.48	0.97	1.99

Table 6.1: Comparison of PTP noise levels for the three different system configurations. The data is gathered from multiple measurements with different laser spot positions.

6.3 Vibration Detection

The exact same test method as the one presented in Section 4.3.1 was used to perform vibration measurements with the improved sensor interface. The only difference was that the improved sensor interface was used with a sampling frequency of 2.4 kHz instead of 6.4 kHz. This was due to the limited transfer speeds, which was discussed in Section 5.6.1. The same measurements were performed to identify any differences between the two sensor interfaces. The two major challenges presented with the initial vibration measurements were also present with the improved sensor interface. One being that the measured vibration amplitude was lower than the applied one. The other was that the measured vibration amplitude would change at different frequencies. However, this was expected as these challenges were discussed to be related to the mechanical setup and not the sensor interface.

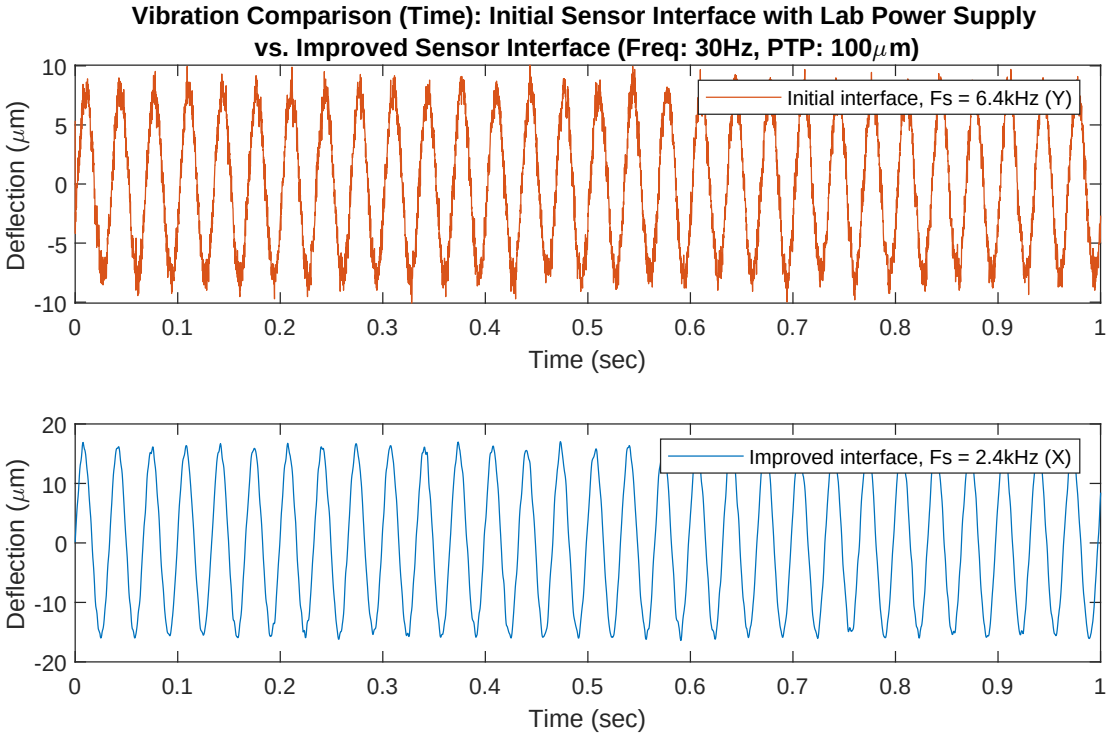

Figure 6.4: Comparing the ability of the two sensor interfaces to detect an applied vibration. The applied vibration is at 30 Hz with an PTP amplitude of 100 µm. The improved sensor interface displays a vibration signal with less noise than the initial sensor interface. The full vibration measurements can be seen in Appendix G.1 and G.5.

Figure 6.4 depicts a comparison of the two different sensor interfaces detecting the same vibration at 30 Hz and 100 µm amplitude. Note that this is not a perfect comparison due to the sample frequency of the two measurements being different. The upper graph displays the measurement that was previously presented in Figure 4.11, while the lower graph displays the measurement with the improved sensor interface. From the comparison we can see that the decreased noise levels of the improved sensor interface is also clearly visible on the measured vibration signals. This results in the measured signal being a more accurate representation of the applied signal. Another thing to notice is the difference in amplitudes. The amplitude of the upper graph is about 18 µm, whilst the amplitude of the lower graph is 30 µm. The reason for the difference in amplitudes is unclear.

Chapter 7

Discussion

7.1 Results of an Improved Sensor Interface

One of the main goals of the master's project was to improve the deflection resolution by reducing the noise of the measurement signals. This has been achieved by developing an improved sensor interface. Section 6.2 presents that the average PTP noise amplitudes with the improved sensor interface is 0.7 µm. This is about 9 times better than the initial sensor interface. The main reasons for this improvement are considered to be the better voltage reference generation, the differential ADC configuration, and the integration of the sampling circuit on the PCB. However, it might not have been necessary to improve the voltage reference that is added to the measurement signals, because the voltage reference is subtracted from the signals anyway with the use of the ADC configuration. Nevertheless, it is still important to generate a good and stable reference for the ADC. The integration of the ADC on the PCB is considered to be important as it makes the amount of noise on the four channels fairly equal, which has been seen to be very advantageous for the noise on the deflection signals.

There were mainly two reasons for implementing adjustable gain of the measurement signals. One reason was to improve the Signal-to-Noise Ratio by amplifying the signal contribution of the sensor, compared to the signal contribution of the voltage reference. This might be an unnecessary function, as the voltage reference is subtracted from the signal anyway. The other reason was to amplify the measurement signals so they could utilise the whole ADC resolution. As seen in Figure 6.2, this is very beneficial as it allows for a more detailed measurement and deflection signals.

From Section 6.1 and 6.3 it is discussed that the system sensitivity and the system's ability to detect vibration was unchanged. This is considered a positive thing, as it indicates that the improvements of the system noise were not at the expense of other system parameters. For example, the noise levels could be improved by applying heavy low-pass filtering. This would limit the system's ability to detect correct vibration amplitudes at higher frequencies. However, this limitation is not observed for the frequency range of 0 to 500 Hz. This is expected, as the cut-off frequency designed for the TIA is at 10 kHz when using a gain resistor value of 50 kΩ. This is 20 times higher than the highest expected signal frequency. Note that the ADC's sampling frequency is only about 5 times higher than the highest vibration frequency, at

2.4 kHz. However, this should neither decrease the vibration amplitudes as much as observed in the vibration measurements.

7.2 Performance of the Sensor System

From the system requirements in Section 1.3.1, it was presented that the sensor system was required to be designed for a cutting tool of 500 mm. The pipe of the test setup was therefore selected to be 500 mm, to mimic a potential cutting tool. Further, it was presented that the sensor system should be able to detect deflections within a range of 2 mm × 2 mm, with a deflection resolution of 1 mm. The system should also be able to measure and reconstruct vibrations up to 500 Hz.

In Section 4.1.2 it was presented that the potential deflection measurement range of the test setup is 2575 µm × 2575 µm. However, due to mechanical limitations the actual measurement range is only a circle with a diameter of 2169.4 µm. This results in the actual measurement area being 92% of the required area of 2000 µm × 2000 µm. This is probably suitable for most cases. However, if a larger measurement area is required, the mechanical components can be modified to allow for a measurement range of 2575 µm × 2575 µm. This can be achieved by making sure that every passage the laser beam travels through from the mirror to the sensor, is at least 9 mm × 9 mm square, or circular with a diameter of 12.73 mm, as presented in Section 3.2.3.

As discussed in Section 7.1, the deflection resolution was identified to be on average 0.7 µm, using the improved sensor interface. This is within the set requirement of 1 µm. In Section 4.3 and 6.3 the sensor system's ability to measure vibrations was discussed. From the measurements it was clear that the system could perfectly measure the applied vibration frequency. However, the amplitudes of the measured vibration were identified to generally be about 5 times lower than the applied amplitudes. In addition, the amplitude was observed to vary with the applied frequency. Both issues are suggested to be challenges related to the mechanical test setup and not the sensor interface. However, this should be further tested in order for this theory to be confirmed. Section 7.3 will present one method for testing this aspect.

It is important to note that the system performance presented in this thesis is specific to the test setup. This is because all displacement values measured are based on the system sensitivity found in Section 4.1.2. The system sensitivity is heavily dependent on how the mirror gets angled when the pipe is deflected. As discussed, the mirror angle will change depending on the pipe being forced or pushed in a direction. These system parameters should therefore only be considered as an indication of how such a sensor system can perform.

7.3 Evaluation of Test Methods

Several of the test results presented have an uncertainty bound to them because of the mechanical system and the test methods used. In retrospect, some of these test methods could have been done differently.

As presented in Section 4.1.1, the system sensitivity is measured by forcing the pipe in a given direction using the displacement system. This will cause the pipe to curve differently compared to when a single point force is applied. The reason for holding the pipe in place with the displacement system, is due to the weight of the pipe and the component housing the mirror. Without the displacement system, the free end of the pipe will start to deflect downwards due to its own weight, making the pipe deflected outside the system's measurement range. This could potentially have been solved by using a more rigid pipe. Another solution could have been to mount the system vertically, pointing the free end of the pipe towards the floor. This would allow the pipe to be undeflected when no force is applied. The displacement system could then be used to deflect the pipe with a single point force.

These solutions could also have been applied for the test method for the vibration measurements. The vibration machine could then be used to push the pipe with a single point force, instead of forcing the pipe to follow its movement. An addition to this setup could have been to use a wire between the vibration machine and the pipe to transfer the vibrations. This will apply the vibration in a more natural movement, compared to the vibration machine directly hitting the pipe.

As presented in Section 4.3.2, the amplitude of the measured vibrations was dependent on the frequency of the vibrations. This was discussed to be a challenge related to the mechanical setup, where some applied vibration frequencies were equal to the resonant frequencies of the pipe. In order to verify that this problem is not related to the sensor interface, the sensor system should have been tested in a transmission configuration without the pipe. By mounting the sensor on the vibration machine, and aligning the laser beam directly onto the sensor, the vibrations could be measured directly. A vibration sweep similar to the one applied in the measurement seen in Figure 4.12 could then have been performed. If the measured amplitude was constant, this would confirm that the problem is related to the mechanical setup.

7.4 Cutting Tool Implementation

The next logical step of the project would have been to apply the sensor system to an internal turning tool. Section 3.1.1 discussed different mounting configurations of the sensor system. The system can potentially be mounted on both the inside, and outside of the turning tool. In addition, the system can be used with a pipe and without a pipe. All these configurations can potentially be used as long as the mirror follows the curvature of the cutting tool. An important aspect with these configurations is that the mirror can not be mounted at the very end of the cutting tool. However, this is not necessarily a problem. As presented in Section 3.2.1, the mirror can potentially be placed anywhere within the pipe. Placing the mirror closer to the beam splitter will increase the deflection measurement range, but decrease the deflection resolution. The same applies when using the optical sensor system in a cutting tool, where the

distance between the beam splitter, the mirror, and the cutting tip will decide the deflection measurement range.

Similar to the test setup, a system sensitivity must be identified when using the optical sensor system in a cutting tool. The sensitivity can technically be identified by performing a theoretical analysis similar to the one presented in Section 3.2.1. However, due to the mechanical complexity of a cutting tool, a better solution might be to perform a calibration to find the system sensitivity. This can be performed similarly to the test method presented in Section 4.1.1, where the cutting tool can be deflected at known values and the laser spot positions can be measured.

In Section 1.1 it was presented that the motivation for using an optical sensor system was that it potentially would require less space inside a cutting tool, compared to the existing solution. The overall space of the sensor system has not been addressed in this project, as the focus has been on the performance and functionality of the sensor system. Another reason for the size of the sensor system not being addressed, is because the overall size is heavily dependent on the mechanical components and not the optical or electrical components. The mechanical components of the test setup are quite bulky and must be miniaturised in order for the sensor system to be implemented into a cutting tool.

Chapter 8

Conclusion

An implementation of an optical sensor system for measuring deflections and vibrations in a cutting tool for internal turning has been developed. By using a mechanical test setup, the performance of the sensor system has been tested. The test setup was dimensioned for cutting tools with a length of 500 mm. At this tool length the sensor system was capable of measuring tool deflections up to 1084.7 µm in every direction, with a deflection resolution of 7.15 µm. By developing an improved sensor interface with less signal noise, the deflection resolution was improved to 0.7 µm.

Vibration measurements revealed that the sensor system perfectly detected the applied vibration frequencies, in the range from 0 to 500 Hz. However, due to mechanical resonance in the test setup, the vibration amplitude is observed to vary with the applied frequency. The optical sensor system is concluded to be a viable option for the defined application, given the fulfilled requirements. However, some mechanical challenges need to be solved in order for the system to be used in a cutting tool.

8.1 Further Work

The sensor interface should be tested independently of the mechanical components, due to uncertainties around the sensor system's ability to detect correct vibration amplitudes. This will reveal if the issues discovered in the vibration measurements are caused by the mechanical setup or the sensor interface. The optical sensor system will need to be miniaturised before being used in a cutting tool. In addition, a system for mounting the sensor system inside a cutting tool must be developed.

Bibliography

[1] R. H. Todd, D. K. Allen and L. Alting, *Manufacturing Processes Reference Guide*. Industrial Press Inc., 1994, 514 pp., ISBN: 978-0-8311-3049-7. Google Books: 6x1smAf_PAcC.

[2] A. Saha, S. Das, M. Suresh, V. Raj Kiran and N. Dey, 'FPGA based self-vibration compensated two dimensional non-contact vibration measurement using 2D position sensitive detector with remote monitoring,' *Measurement*, vol. 111, pp. 271–278, 1st Dec. 2017, ISSN: 0263-2241. DOI: 10.1016/j.measurement.2017.07.038. [Online]. Available: https://www.sciencedirect.com/science/article/pii/S0263224117304748 (visited on 04/06/2021).

[3] D. Shetty, A. Ali and J. Hill, 'Optical instrumentation for vibration measurement and monitoring,' *International Journal of Precision Engineering and Manufacturing*, vol. 12, no. 3, pp. 405–411, 2011, ISSN: 2234-7593. DOI: 10.1007/s12541-011-0052-5.

[4] *PHOTODIODE BASICS – Wavelength Electronics*. [Online]. Available: https://www.teamwavelength.com/photodiode-basics/ (visited on 20/05/2021).

[5] *Two-dimensional PSD S5991-01*. [Online]. Available: https://www.hamamatsu.com/eu/en/product/type/S5991-01/index.html (visited on 20/05/2021).

[6] *CPS635R, compact laser modules with phono jack*. [Online]. Available: https://www.thorlabs.com/newgrouppage9.cfm?objectgroup_id=1487&pn=CPS635R#1620 (visited on 20/05/2021).

[7] *AS89000 Transimpedance-Amplifier, Ams*. [Online]. Available: https://ams.com/as89000 (visited on 20/05/2021).

[8] *Sensor Terminology, NI*. [Online]. Available: https://www.ni.com/en-no/innovations/white-papers/13/sensor-terminology.html (visited on 20/05/2021).

[9] J. M. Bland and D. G. Altman, 'Statistics notes: Measurement error,' *BMJ*, vol. 312, no. 7047, p. 1654, 29th Jun. 1996, ISSN: 0959-8138, 1468-5833. DOI: 10.1136/bmj.312.7047.1654. pmid: 8664723. [Online]. Available: https://www.bmj.com/content/312/7047/1654 (visited on 20/05/2021).

[10] *Resolution Specifications and Effects on Performance*, Lion Precision. [Online]. Available: https://www.lionprecision.com/understanding-sensor-resolution-specifications-and-effects-on-performance/ (visited on 19/05/2021).

[11] D. Halliday, R. Resnick and J. Walker, *Fundamentals of Physics*. John Wiley & Sons, 13th Aug. 2013, 1235 pp., ISBN: 978-1-118-23071-8. Google Books: HybkAwAAQBAJ.

[12] *OPA4388 data sheet, product information and support | TI.com*. [Online]. Available: https://www.ti.com/product/OPA4388 (visited on 24/05/2021).

[13] *MCP4462 - Digital Potentiometers*. [Online]. Available: https://www.microchip.com/wwwproducts/en/MCP4462 (visited on 24/05/2021).

[14] J. Caldwell, '1 MHz, Single-Supply, Photodiode Amplifier Reference Design,' p. 21, 2014. [Online]. Available: https://www.ti.com/lit/ug/tidu535/tidu535.pdf?ts=1601907026151&ref_url=https%253A%252F%252Fwww.google.com%252F (visited on 25/05/2021).

[15] *MCP1501 - Voltage References*. [Online]. Available: https://www.microchip.com/wwwproducts/en/MCP1501 (visited on 25/05/2021).

[16] *Digital Signal Processing: Sampling Rates, Bandwidth, Spectral Lines, and more...* [Online]. Available: https://community.sw.siemens.com/s/article/digital-signal-processing-sampling-rates-bandwidth-spectral-lines-and-more (visited on 07/06/2021).

[17] *MCP3912 - Energy Measurement*. [Online]. Available: https://www.microchip.com/wwwproducts/en/MCP3912 (visited on 26/05/2021).

[18] *ADS1174 data sheet, product information and support | TI.com*. [Online]. Available: https://www.ti.com/product/ADS1174 (visited on 26/05/2021).

[19] *ADS131A04 data sheet, product information and support | TI.com*. [Online]. Available: https://www.ti.com/product/ADS131A04#product-details#features (visited on 26/05/2021).

[20] *TTL-234X-3V3*, FTDI. [Online]. Available: https://ftdichip.com/products/ttl-234x-3v3/ (visited on 27/05/2021).

[21] *ATTINY1626 - 8-bit Microcontrollers*. [Online]. Available: https://www.microchip.com/wwwproducts/en/ATtiny1626 (visited on 27/05/2021).

[22] *MIC5319 - Linear Regulators*. [Online]. Available: https://www.microchip.com/wwwproducts/en/MIC5319 (visited on 27/05/2021).

[23] *Digital Systems Design with FPGAs and CPLDs*. Elsevier, 2008, ISBN: 978-0-7506-8397-5. DOI: 10.1016/B978-0-7506-8397-5.X0001-3. [Online]. Available: https://linkinghub.elsevier.com/retrieve/pii/B9780750683975X00013 (visited on 28/05/2021).

Appendix A

Circuit Diagram of Improved Sensor Interface

The following page depicts the circuit diagram for the improved sensor interface. The circuit diagram has been designed in Altium Designer and is used to make the PCB layout presented in Appendix B.

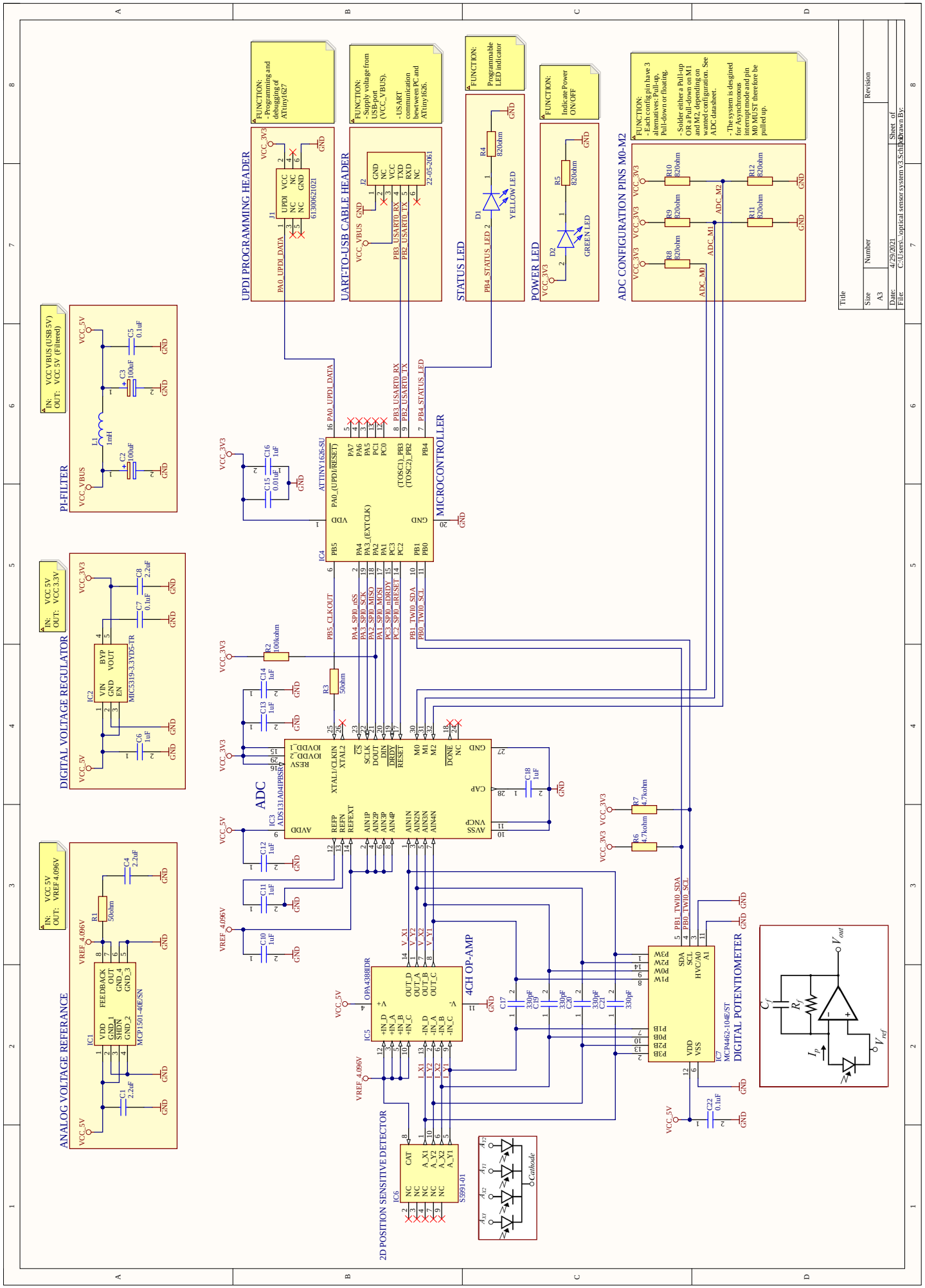
ANALOG VOLTAGE REFERANCE
DIGITAL VOLTAGE REGULATOR
PI-FILTER
ADC
MICROCONTROLLER
4CH OP-AMP
DIGITAL POTENTIOMETER
2D POSITION SENSITIVE DETECTOR
UPDI PROGRAMMING HEADER
UART-TO-USB CABLE HEADER
STATUS LED
POWER LED
ADC CONFIGURATION PINS M0-M2

Appendix B

PCB Layout of Improved Sensor Interface

The following page depicts the layout of the improved sensor interface in both a 2D and 3D view. The PCB layout is designed from the circuit diagram presented in Appendix A, using Altium Designer.

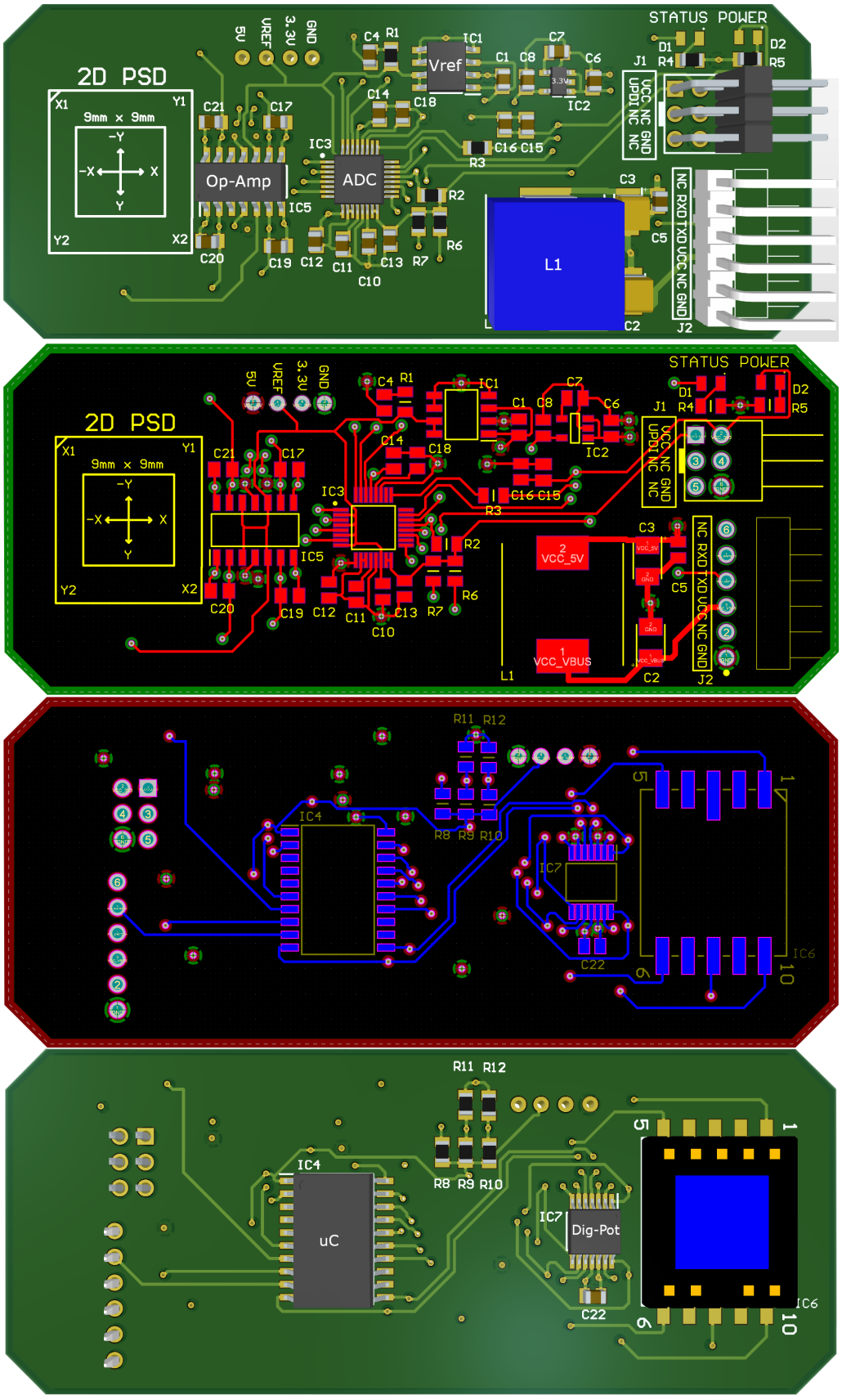
2D PSD
9mm x 9mm
Op-Amp
ADC
Vref
uC
Dig-Pot
STATUS POWER
L1
J1
J2

Appendix C

Bill of Materials for the Improved Sensor Interface

The following page present the bill of materials for the PCB of the improved sensor interface. This is an overview of all the components mounted on the PCB.

Comment	Description	Designator	Part Number	Quantity
2.2uF	Ceramic Capacitor	C1, C4, C8	C0805C225K4PACTU	3
100uF	Tantalum Capacitor	C2, C3	T495B107K006ATE400	2
0.1uF	Ceramic Capacitor	C5, C7, C22	C0805C104K4RACTU	3
1uF	Ceramic Capacitor	C6, C10, C11, C12, C13, C14, C16, C18	C0805C105J4RECTU	8
0.01uF	Ceramic Capacitor	C15	C0805X103K5RAC3316	1
330pF	Ceramic Capacitor	C17, C19, C20, C21	C0805C331J5GAC	4
YELLOW LED	LED Yellow 591nm 25mA 2.5V	D1	LYR976-PS-36	1
GREEN LED	LED Green 572nm 20mA 2.2V	D2	LGR971-KN-1	1
MCP1501-40E/SN	V-Ref Precision 4.096V 20mA	IC1	MCP1501-40E/SN	1
MIC5319-3.3YD5-TR	Linear Regulator 3.3V 500MA	IC2	MIC5319-3.3YD5-TR	1
ADS131A04IPBSR	ADC, 24 bit, 128 kSPS	IC3	ADS131A04IPBSR	1
ATTINY1626-SU	Microcontroller	IC4	ATTINY1626-SU	1
OPA4388IDR	Quad Op Amp	IC5	OPA4388IDR	1
S5991-01	2D Position Sensitive Device	IC6	S5991-01	1
MCP4462-104E/ST	Quad Digital Potentiometer , 8-bit 100KOhm	IC7	MCP4462-104E/ST	1
61300621021	Connector, Through Hole, 6x1 Header, 2.54 mm	J1	61300621021	1
22-05-2061	Connector, Through Hole, 3x2 Header, 2.54 mm	J2	22-05-2061	1
1mH	Inductor 600mA 12x12mm	L1	7447706102	1
50ohm	Thick Film Resistor 0.125W	R1, R3	CRCW080550R0FKTA	2
100kohm	Thick Film Resistor 0.125W	R2	CRCW0805100KFKEA	1
820ohm	Thick Film Resistor 0.125W	R4, R5, R8, R9, R10, R11, R12	CRCW0805820RFKEA	7
4.7kohm	Thick Film Resistor 0.125W	R6, R7	CRCW08054K70FKTA	2

Appendix D

Trigonometrical Analysis

This chapter presents the figure and equations identified from the trigonometrical analysis.

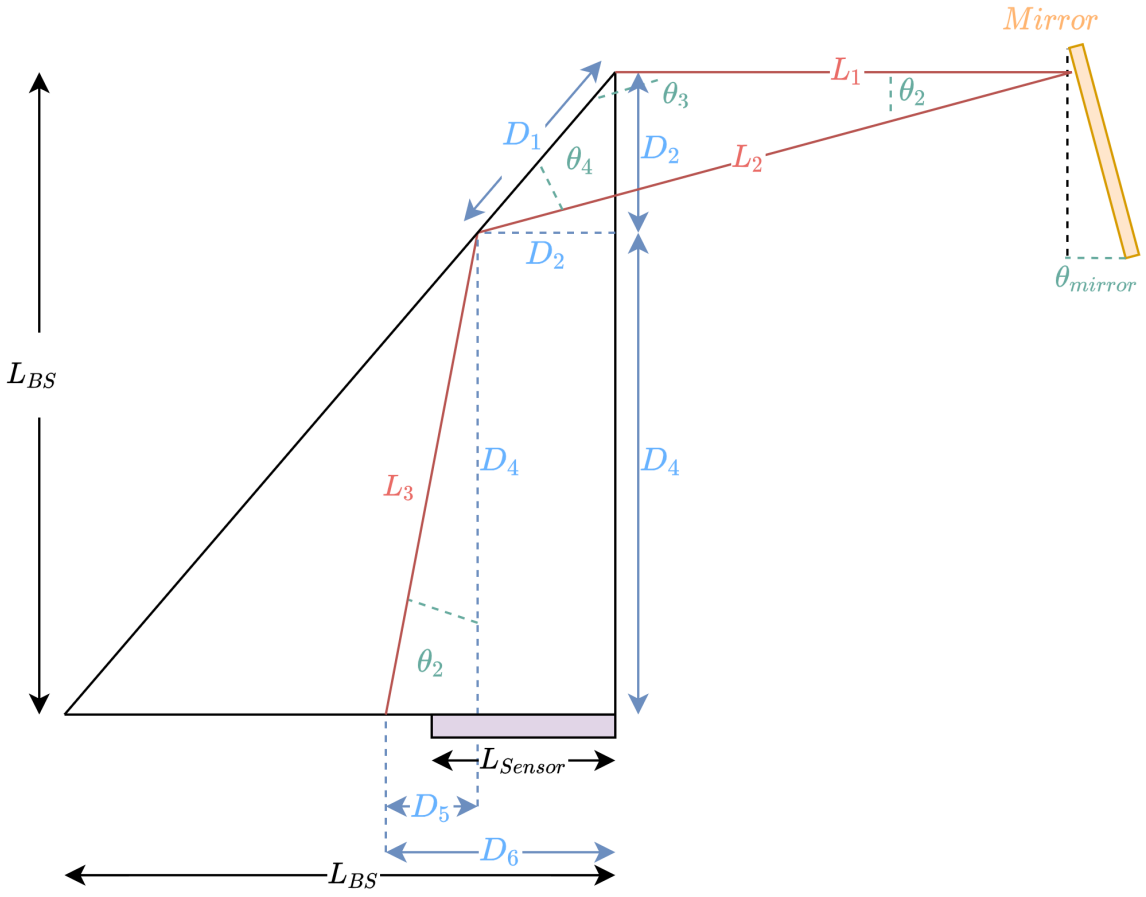

Figure D.1: Trigonometrical figure of the test setup. A change in the mirror angle, θ_{mirror}, will result in a change of the laser spot displacement, D_6.

L_1: Distance between beam splitter and mirror.

L_{BS}: Size of the beam splitter.

L_{Sensor}: Sensor area length.

D_6: Displacement of the laser beam.

θ_{mirror}: Angle of the mirror.

$$\theta_2 = 2\theta_{mirror} \tag{D.1}$$

$$\theta_3 = 135^\circ \tag{D.2}$$

$$\theta_4 = 180^\circ - (\theta_2 + \theta_3) \tag{D.3}$$

$$D_1 = \frac{sin\,\theta_2}{sin\,\theta_4} L_1 \tag{D.4}$$

$$D_2 = \sqrt{\frac{D_1^2}{2}} \tag{D.5}$$

$$L_2 = \frac{sin\,\theta_3}{sin\,\theta_4} L_1 \tag{D.6}$$

$$D_4 = L_{BS} - D_2 \tag{D.7}$$

$$D_5 = D_4\,tan\,\theta_2 \tag{D.8}$$

$$L_3 = \frac{D_4}{tan\,\theta_2} \tag{D.9}$$

$$D_6 = D_5 + D_2 \tag{D.10}$$

$$D_6 = tan\,(2\theta_{mirror})(L_{BS} - \sqrt{\frac{\left(\frac{sin\,(2\theta_{mirror})\,L_1}{sin\,(45^\circ - 2\theta_{mirror})}\right)^2}{2}}) + \sqrt{\frac{\left(\frac{sin\,(2\theta_{mirror})\,L_1}{sin\,(45^\circ - 2\theta_{mirror})}\right)^2}{2}} \tag{D.11}$$

Appendix E

Cantilever Beam Deflection

This chapter presents the figure and equations used to identify the deflection and end-slope of a cantilever beam.

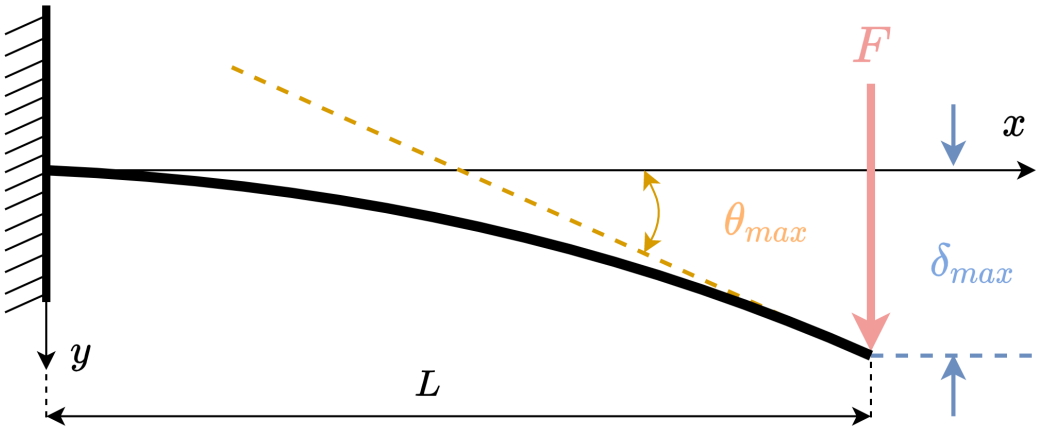

A force F is being applied to the end of a cantilever with length L. This results in a deflection of the cantilever, where δ_{max} is the deflection at the end point of the beam and θ_{max} is the slope of the beam at this point. These two parameters can be calculated by using Equation (E.1) and (E.2).

$$\delta = -\frac{Fx^2}{6EI}(3L - x) \tag{E.1}$$

$$\theta = -\frac{Fx}{2EI}(2L - x) \tag{E.2}$$

In these equations E is Young's modulus, a mechanical property that measures the stiffness of a solid material. I is the moment of inertia for the cross section of the cantilever. Note that these equations can be used to calculate the deflection and the slope of the cantilever at any point along the x-axis. By setting $x = L$ one can calculate the slope and the deflection at the end of the beam. This can be expressed as Equation (E.3) and (E.4).

$$\delta_{max} = \frac{FL^3}{3EI} \quad , \quad x = L \tag{E.3}$$

$$\theta_{max} = \frac{FL^2}{2EI} \quad , \quad x = L \tag{E.4}$$

Equation (E.5) can be used to calculate the end slope of the cantilever when the deflection is given, or vice versa.

$$\theta_{max} = \frac{3\,\delta_{max}}{2L} \quad , \quad x = L \tag{E.5}$$

Appendix F

Noise Measurement Results

This chapter presents six of the noise measurements conducted during this project. This includes noise measurements on both the initial and improved sensor interface. The test method used for these noise measurements are described in Section 4.2.1. Following is a overview of the noise measurements depicted in this chapter:

F.1 Initial Sensor Interface: Biltema Power Supply (X=2 Y=0): A noise measurement of the initial sensor interface, where the laser spot was aligned in the center of the sensor's measurement area and a Biltema power supply was used.

F.2 Initial Sensor Interface: Biltema Power Supply (X=-700 Y=51): A noise measurement of the initial sensor interface, where the laser spot was aligned approximately in the middle between the center and one edge of the sensor's measurement area. A Biltema power supply was used.

F.3 Initial Sensor Interface: Lab Power Supply (X=2 Y=-1): A noise measurement of the initial sensor interface, where the laser spot was aligned in the center of the sensor's measurement area and a Lab power supply was used.

F.4 Improved Sensor Interface: (X=10 Y=0), Rf = 25kohm: A noise measurement of the improved sensor interface, where the laser spot was aligned in the center of the sensor's measurement area and a gain resistor value of 25 kΩ was selected.

F.5 Improved Sensor Interface: (X=-1 Y=-1), Rf = 50kohm: A noise measurement of the improved sensor interface, where the laser spot was aligned in the center of the sensor's measurement area and a gain resistor value of 50 kΩ was selected.

F.6 Improved Sensor Interface: (X=23 Y=8), Rf = 100kohm: A noise measurement of the improved sensor interface, where the laser spot was aligned in the center of the sensor's measurement area and a gain resistor value of 100 kΩ was selected.

F.1 Initial Sensor Interface: Biltema Power Supply (X=2 Y=0)

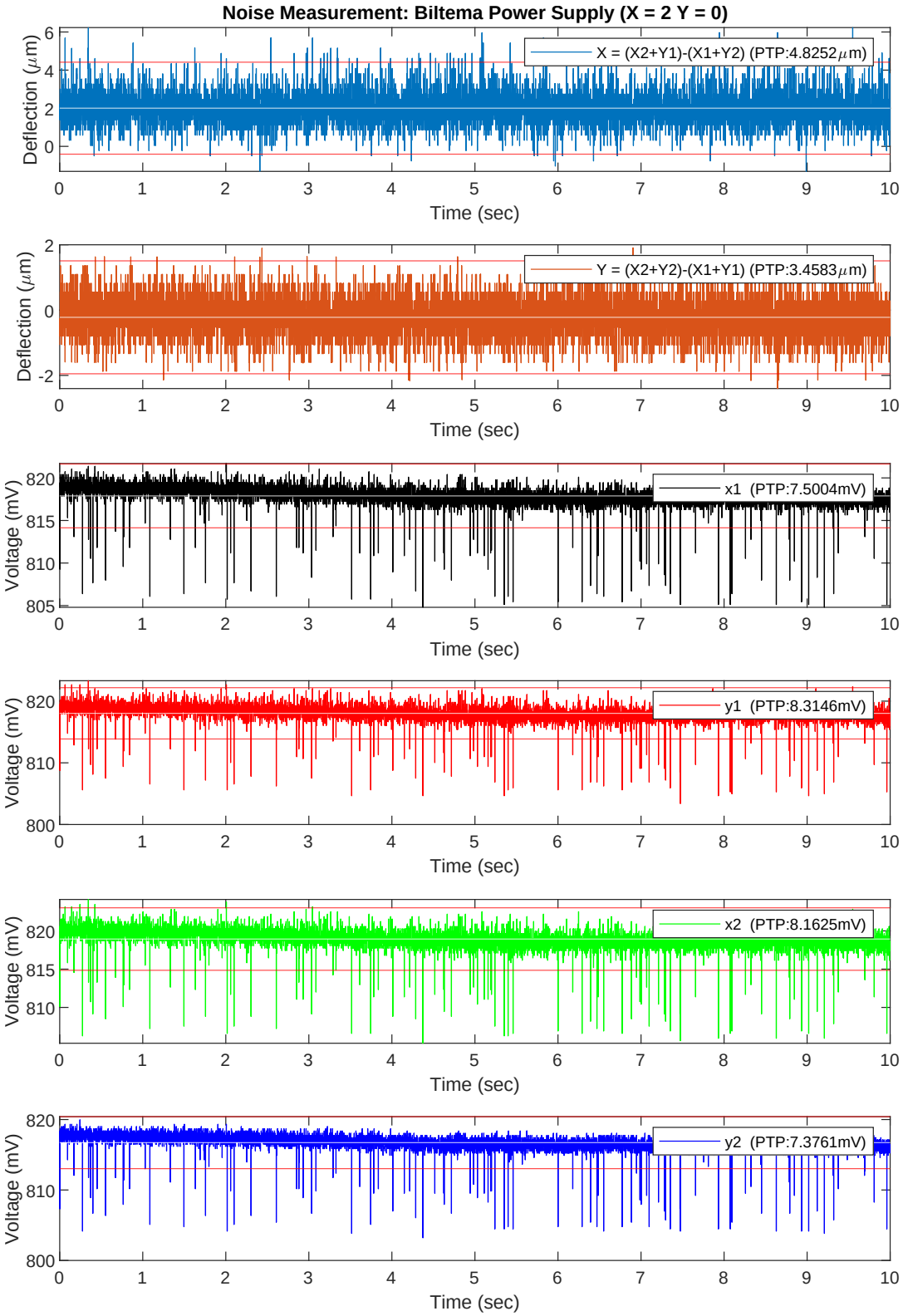

F.2 Initial Sensor Interface: Biltema Power Supply (X=-700 Y=51)

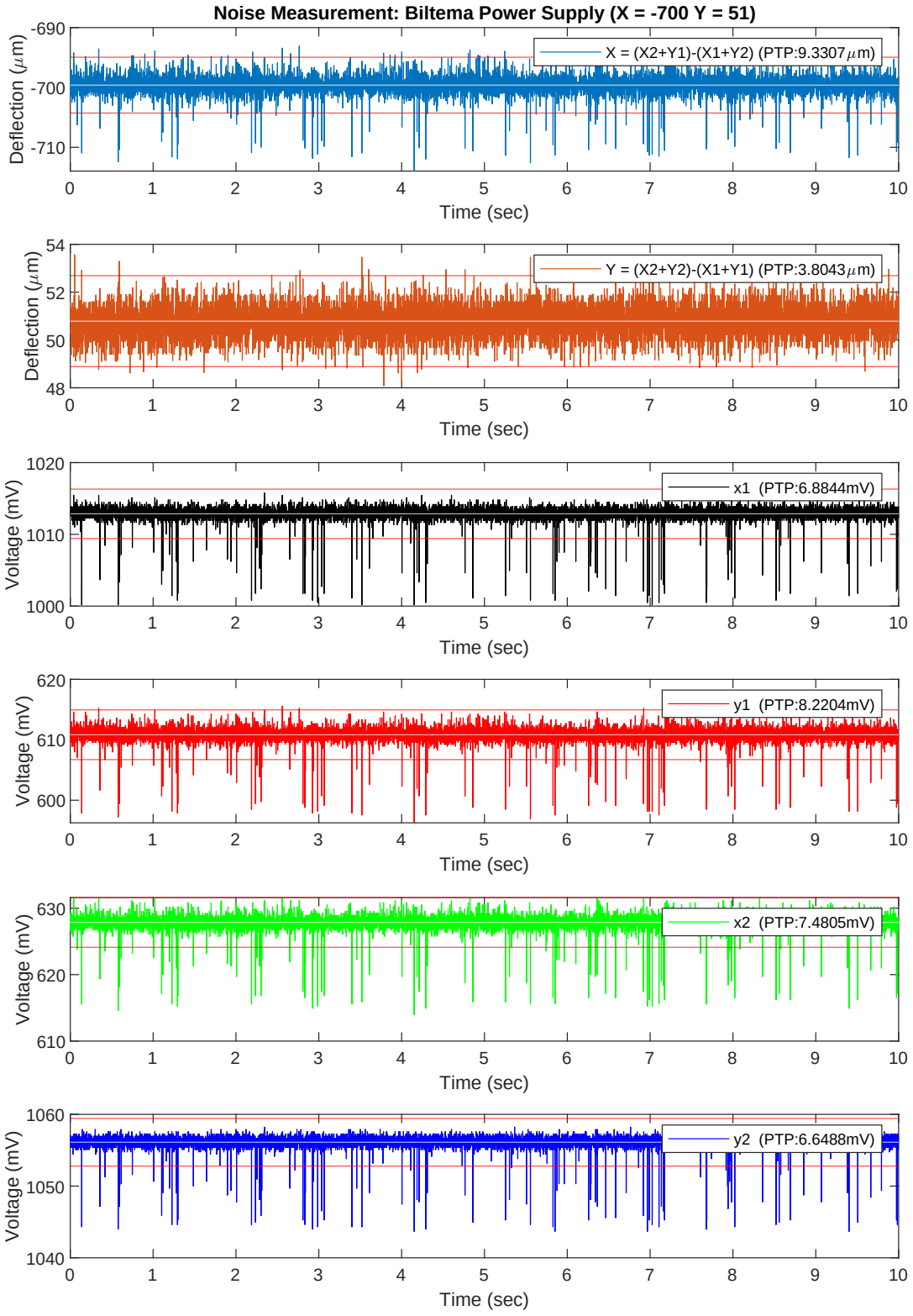

F.3 Initial Sensor Interface: Lab Power Supply (X=2 Y=-1)

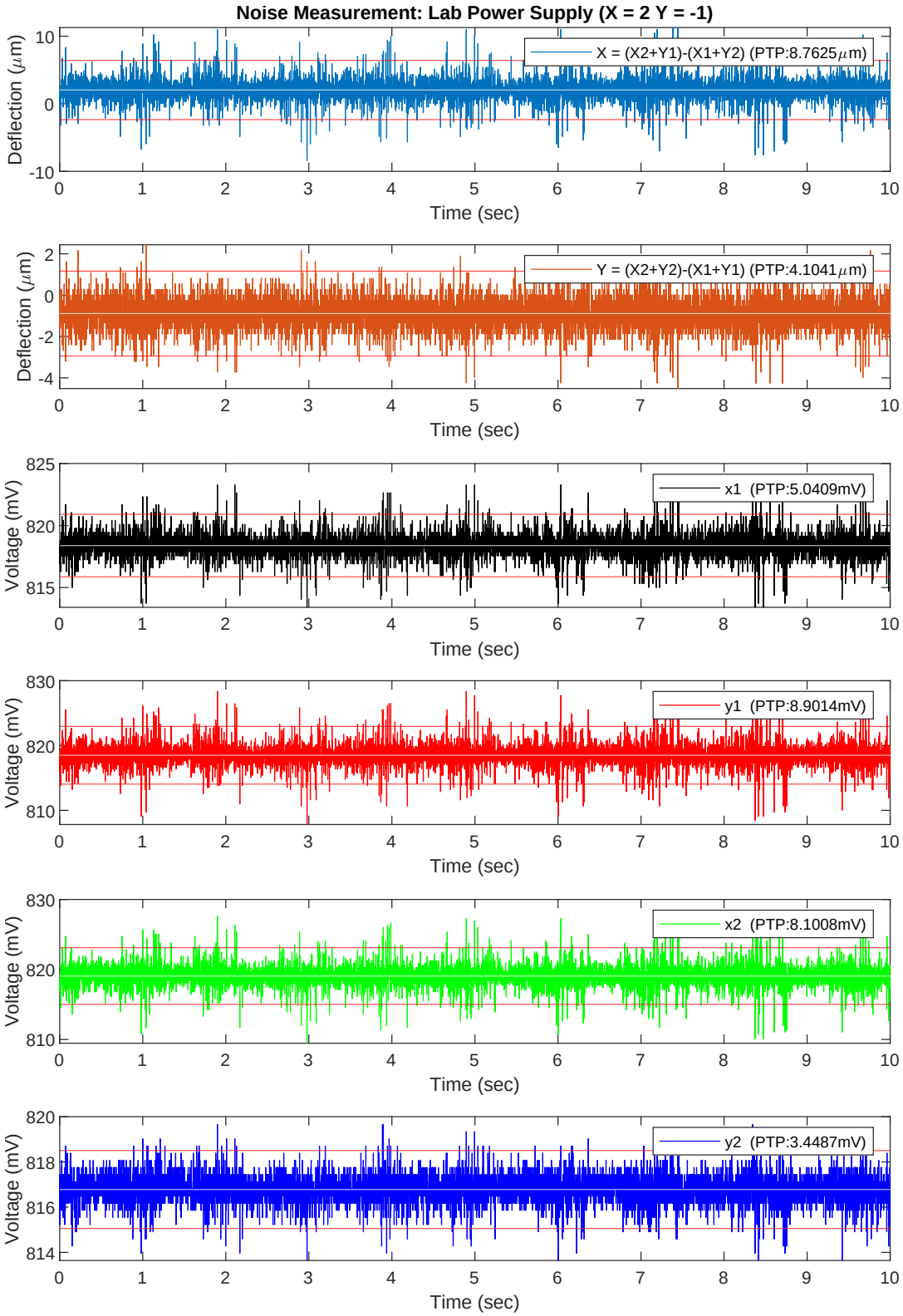

F.4 Improved Sensor Interface: (X=10 Y=0), Rf = 25kohm

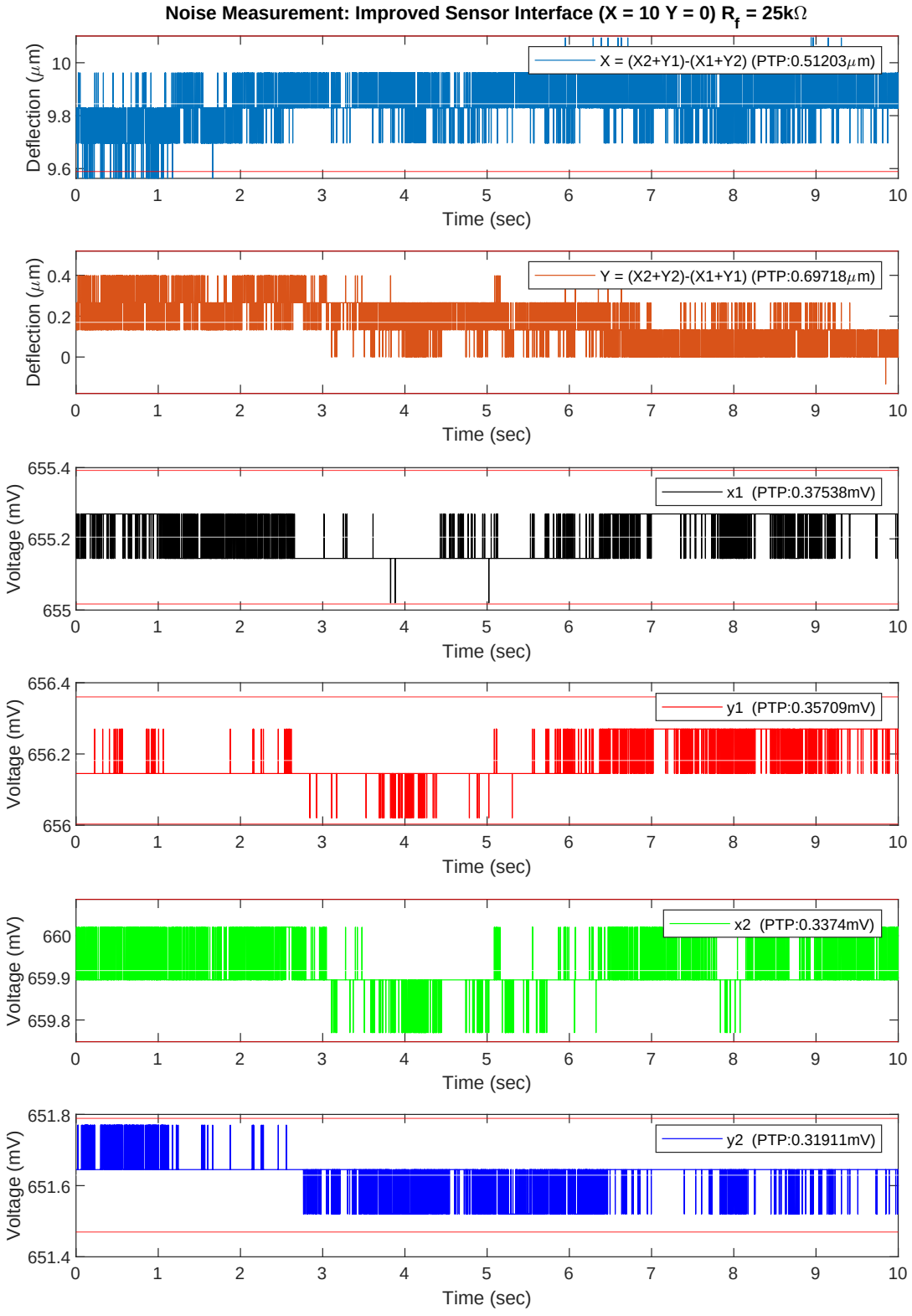

F.5 Improved Sensor Interface: (X=-1 Y=-1), Rf = 50kohm

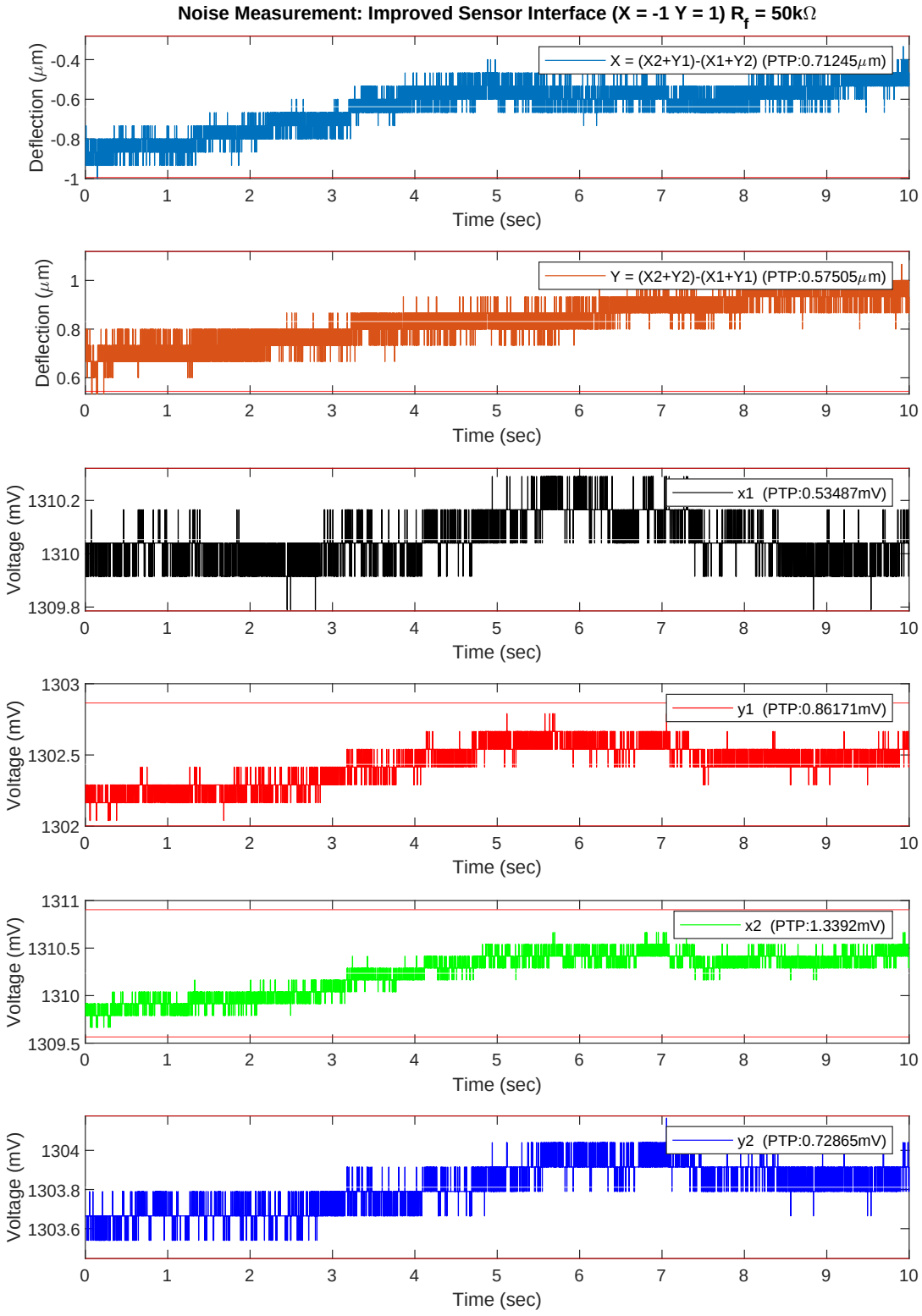

F.6 Improved Sensor Interface: (X=23 Y=8), Rf = 100kohm

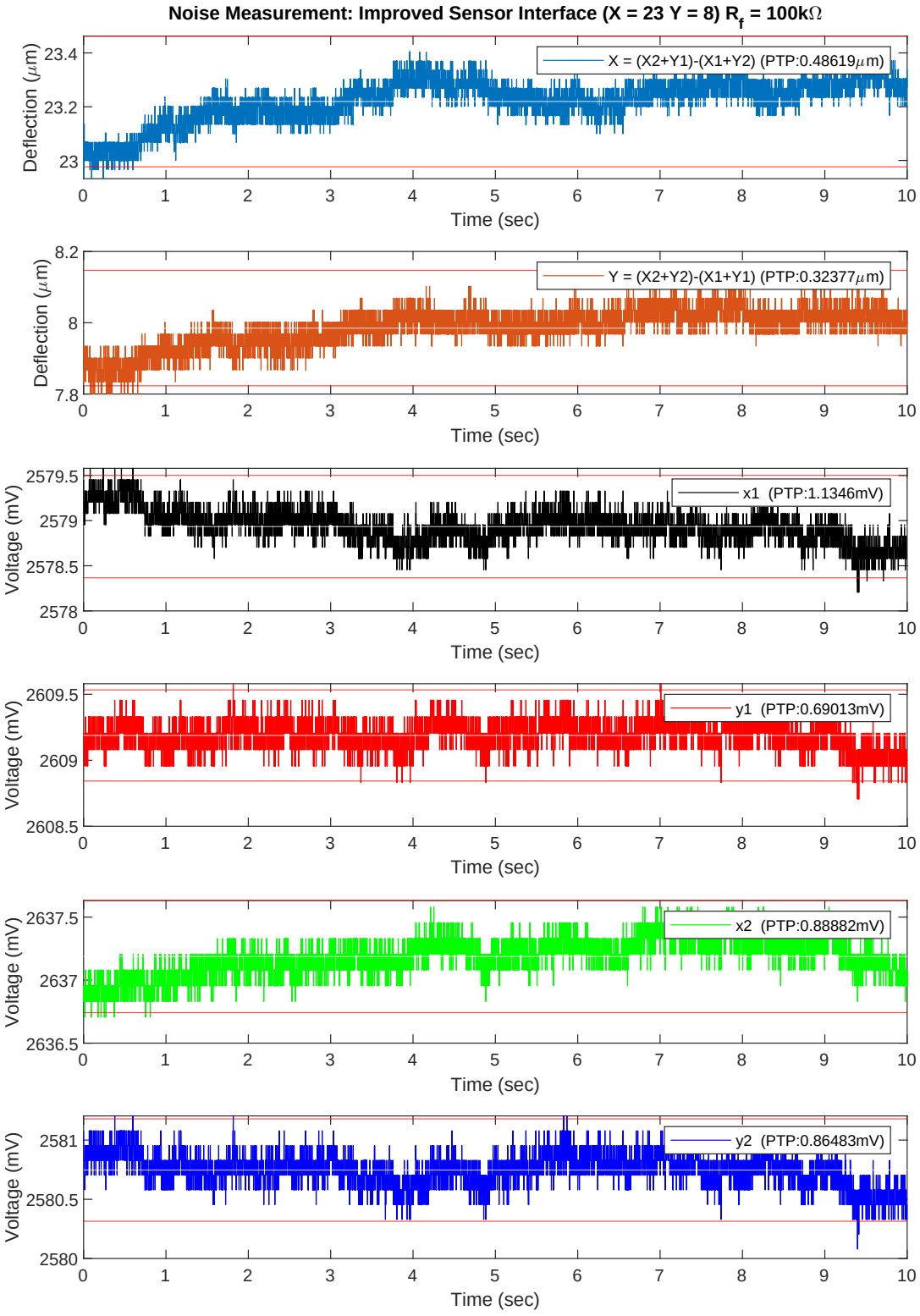

Appendix G

Vibration Measurement Results

This chapter presents six of the vibration measurements conducted during this project. This includes vibration measurements on both the initial and improved sensor interface. The test method used for these vibration measurements are described in Section 4.3.1. Following is a overview of the vibration measurements depicted in this chapter:

G.1 Initial Sensor Interface: Time signal (30Hz, 100um): A vibration measurement with the initial sensor interface, where a constant vibration of 30 Hz with a PTP amplitude of 100 µm was applied in the Y-axis. The ADC's sampling frequency was 6400 Hz.

G.2 Initial Sensor Interface: FFT (30Hz, 100um): A FFT analysis of the vibration measurement depicted in G.1.

G.3 Initial Sensor Interface: Time Signal (20 to 200Hz, 20um): A vibration measurement with the initial sensor interface, where a linear vibration frequency sweep, from 20 Hz to 200 Hz with a PTP amplitude of 20 µm, was applied in the Y-axis. The ADC's sampling frequency was 6400 Hz.

G.4 Initial Sensor Interface: FFT (20 to 200Hz, 20um): A FFT analysis of the vibration measurement depicted in G.3.

G.5 Improved Sensor Interface: Time Signal (30Hz, 100um): A vibration measurement with the improved sensor interface, where a constant vibration of 30 Hz with a PTP amplitude of 100 µm was applied in the X-axis. The ADC's sampling frequency was 2440 Hz.

G.6 Improved Sensor Interface: FFT (30Hz, 100um): A FFT analysis of the vibration measurement depicted in G.5.

G.1 Initial Sensor Interface: Time signal (30Hz, 100um)

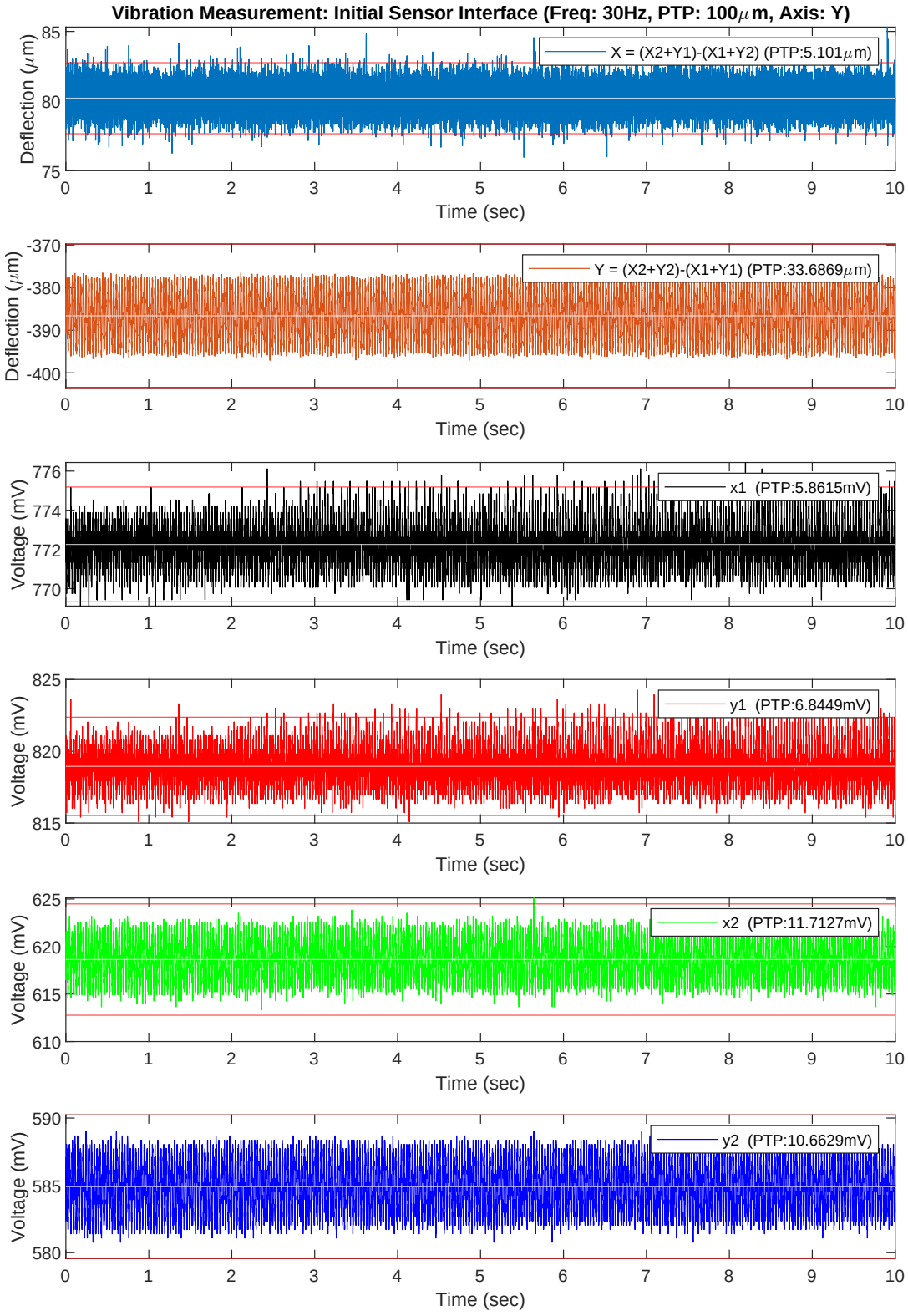

G.2 Initial Sensor Interface: FFT (30Hz, 100um)

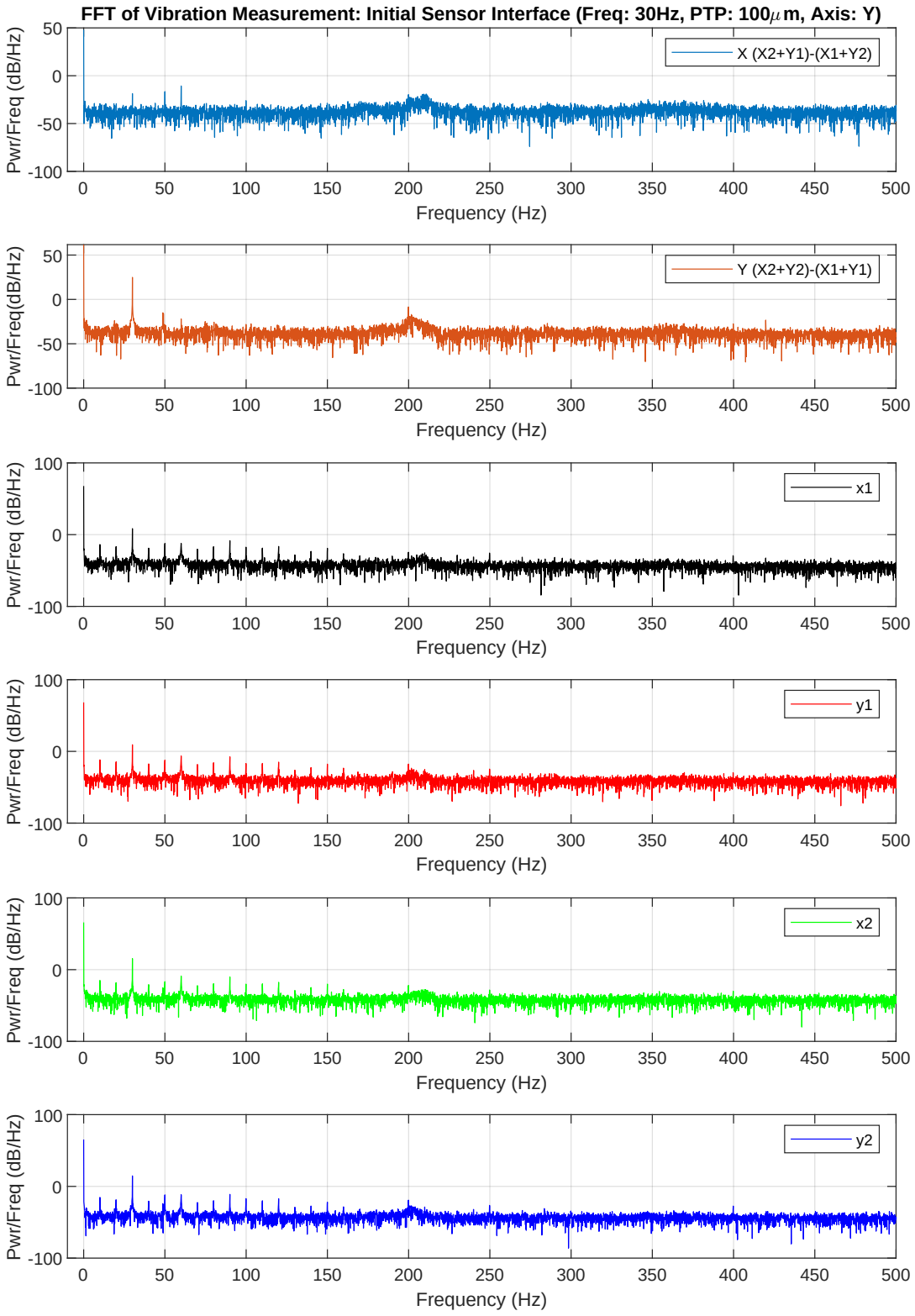

G.3 Initial Sensor Interface: Time Signal (20 to 200Hz, 20um)

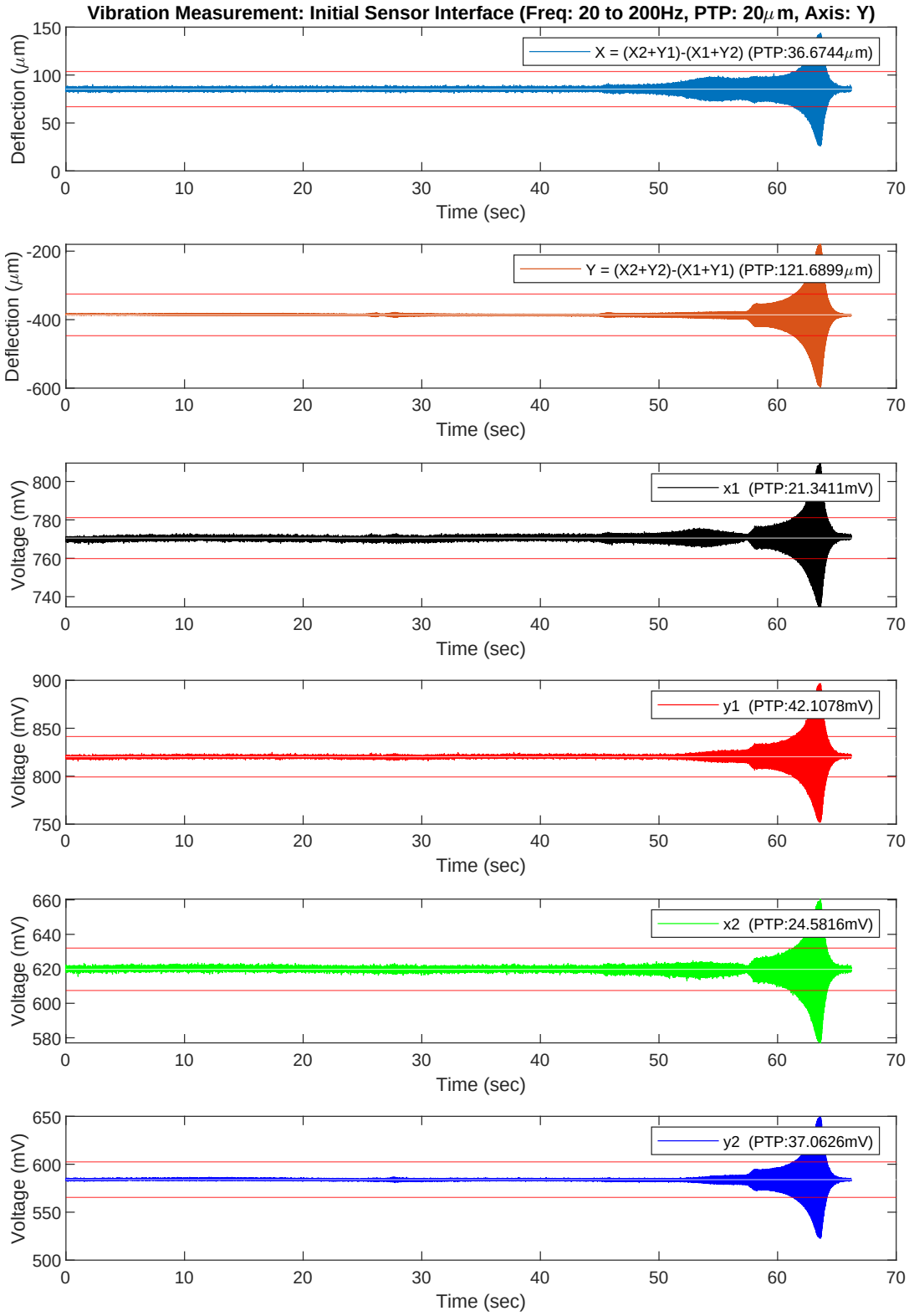

G.4 Initial Sensor Interface: FFT (20 to 200Hz, 20um)

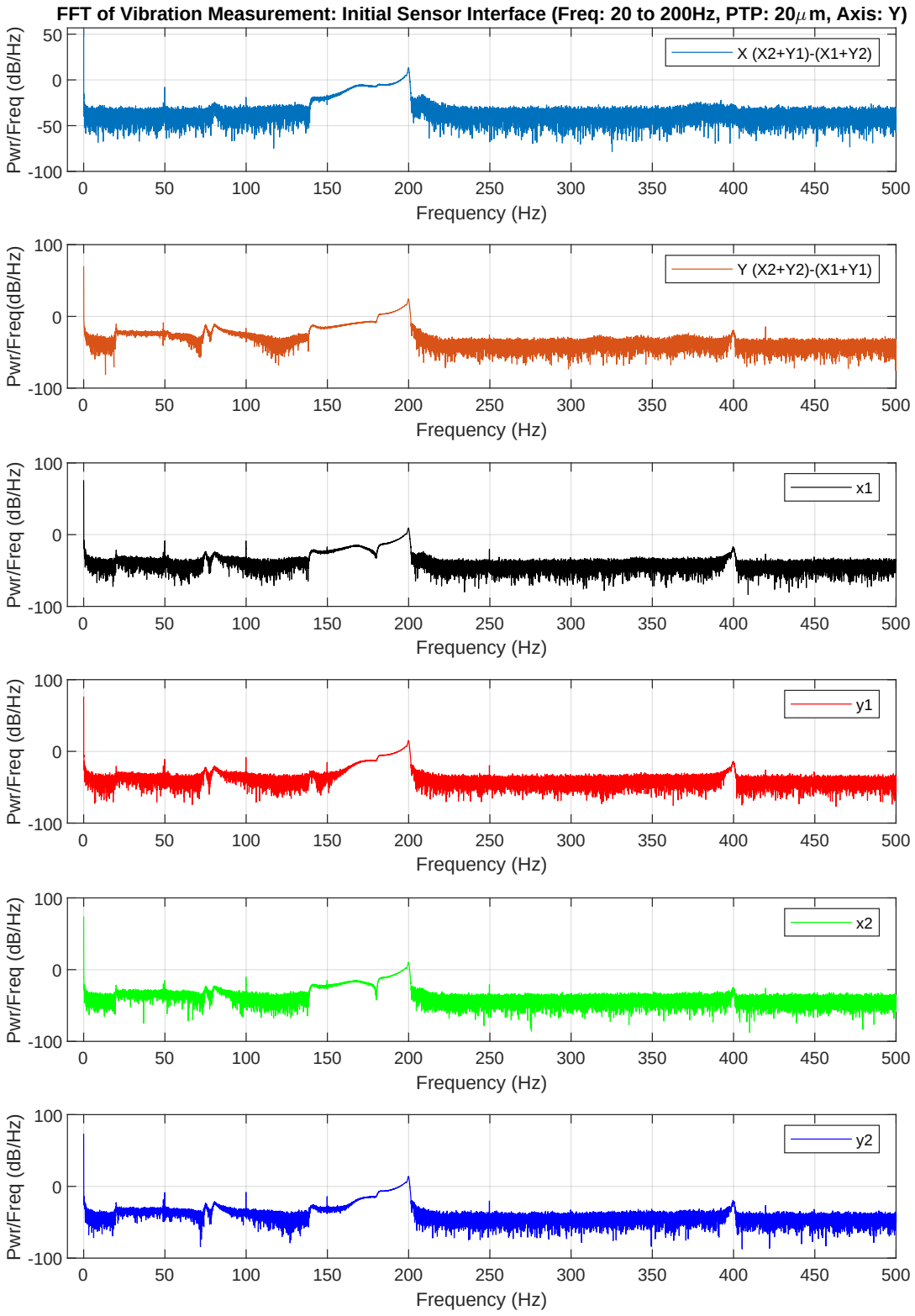

G.5 Improved Sensor Interface: Time Signal (30Hz, 100um)

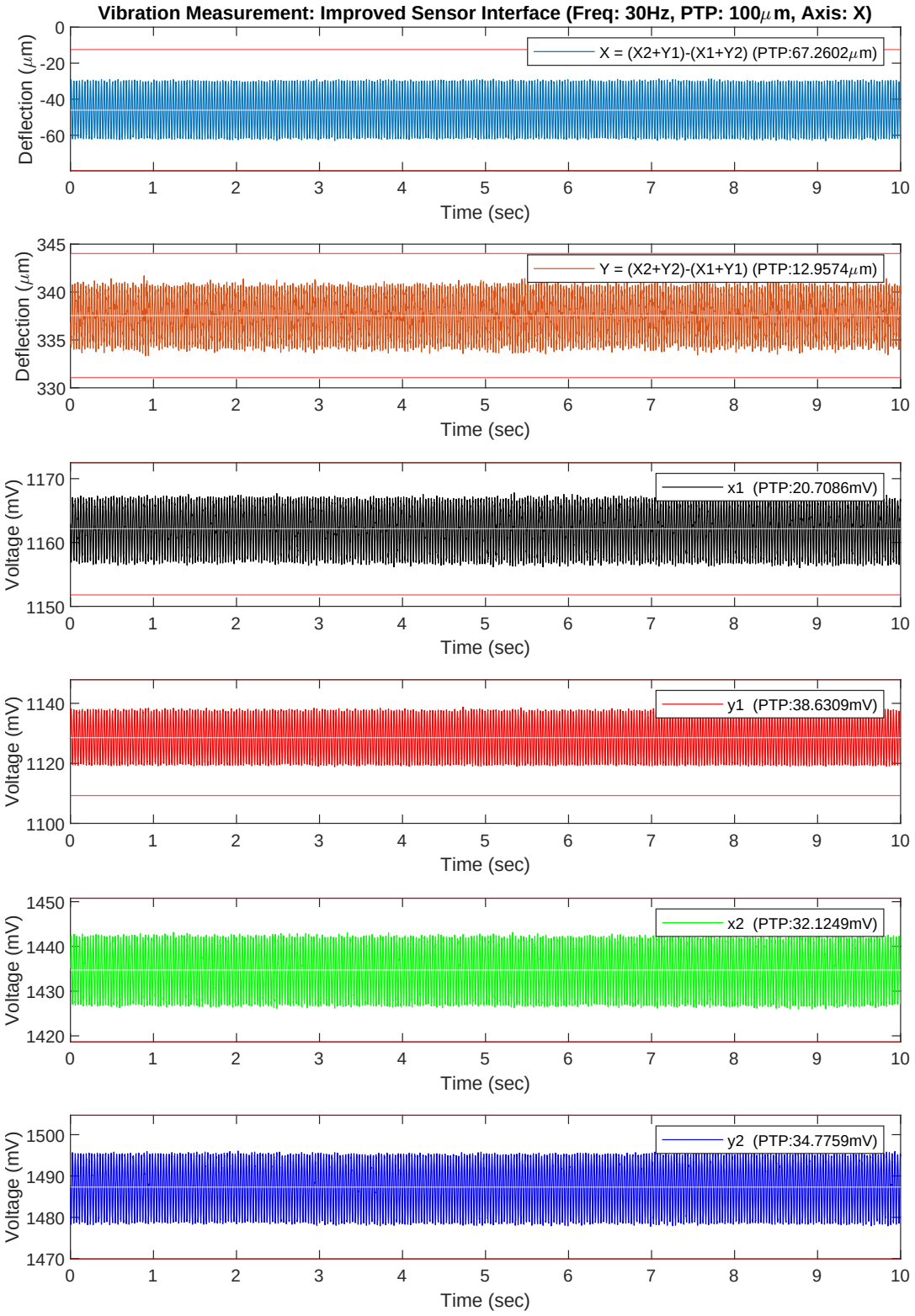

G.6 Improved Sensor Interface: FFT (30Hz, 100um)

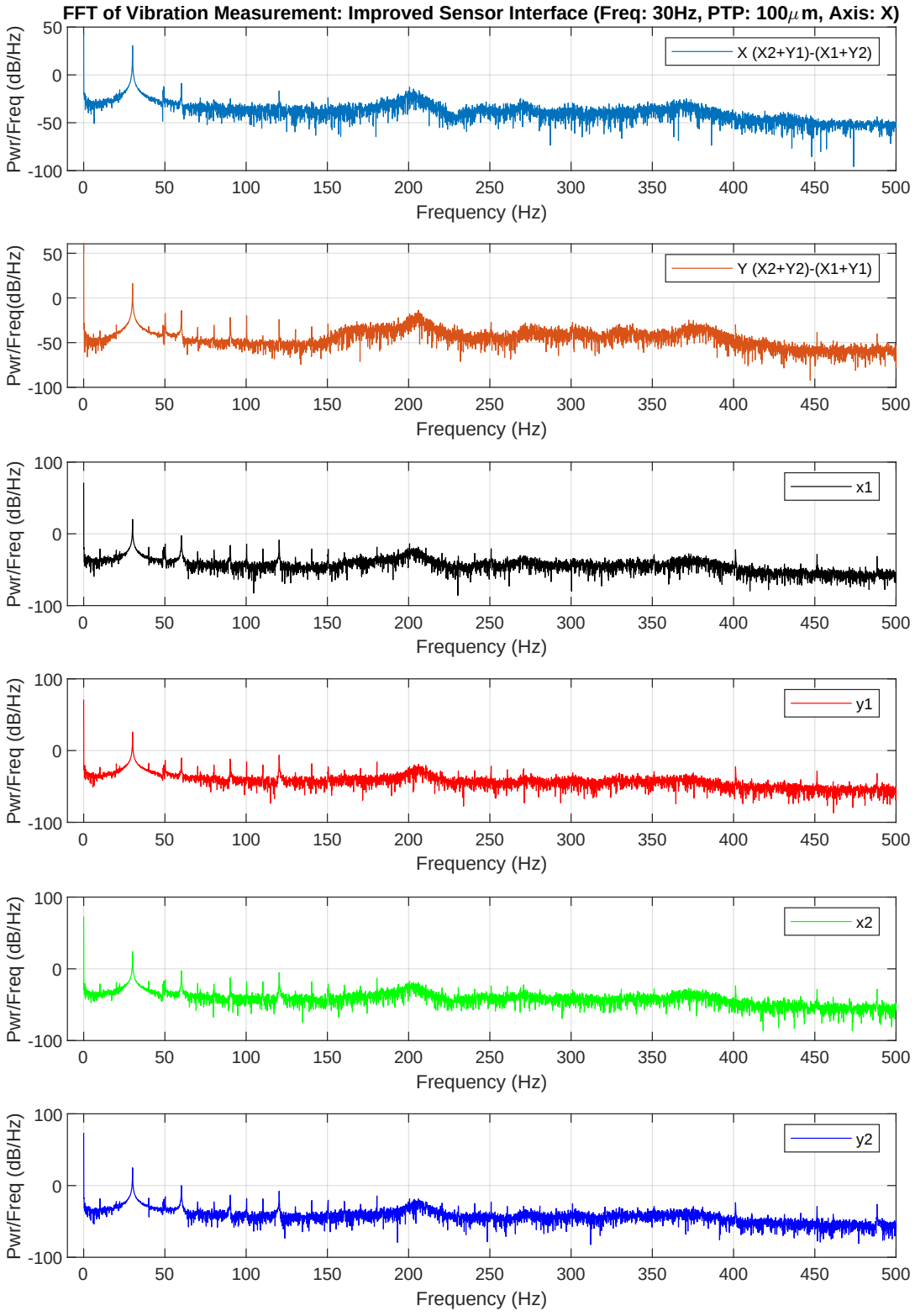

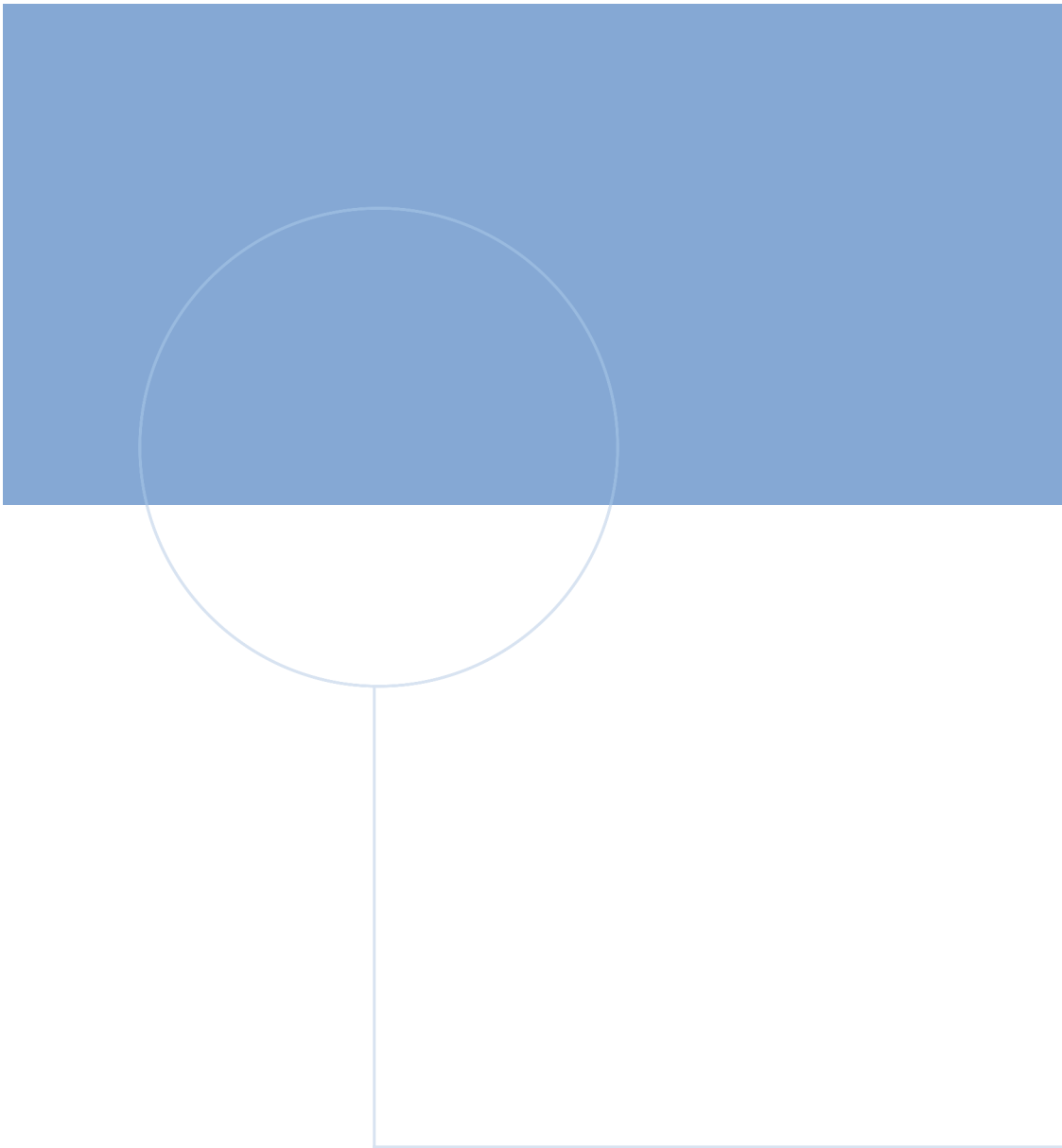

NTNU

Norwegian University of
Science and Technology